COMENIUS UNIVERSITY IN BRATISLAVA FACULTY OF MATHEMATICS, PHYSICS AND INFORMATICS

DECAY SPECTROSCOPY OF NEUTRON-DEFICIENT ISOTOPES ^{179}HG AND ^{177}AU

ACADEMIC DISSERTATION

Mgr. Andrej Špaček

2023

COMENIUS UNIVERSITY IN BRATISLAVA FACULTY OF MATHEMATICS, PHYSICS AND INFORMATICS

DECAY SPECTROSCOPY OF NEUTRON-DEFICIENT ISOTOPES ^{179}HG AND ^{177}AU

THE PROJECT OF ACADEMIC DISSERTATION

Academic Dissertation

for the degree of

Doctor of Philosophy

Subject:	Nuclear and subnuclear physics
Branch of study:	4.1.5. Nuclear and subnuclear physics
Institute:	Institute of Physics, Slovak Academy of Sciences
Department:	Department of Nuclear Physics
Supervisor:	Mgr. Andrej Herzáň, PhD.

Mgr. Andrej Špaček

2023

86149838

Comenius University Bratislava
Faculty of Mathematics, Physics and Informatics

THESIS ASSIGNMENT

Name and Surname:	Mgr. Andrej Špaček
Study programme:	Nuclear and Subnuclear Physics (Single degree study, Ph.D. III. deg., full time form)
Field of Study:	Physics
Type of Thesis:	Dissertation thesis
Language of Thesis:	English
Secondary language:	Slovak

Title: Decay spectroscopy of neutron-deficient isotopes 179Hg and 177Au

Annotation: Nuclear energy levels with a low and medium spin carry an important information about nuclear structure, e.g. evolution of deformation and a phenomenon known as shape coexistence. These states are often non-yrast. As such, they are difficult to populate with a reasonable statistics in the in-beam gamma spectroscopic studies. In the case of exotic heavy nuclei, decay spectroscopy is often the only way how to get the desired information. An example is the study of alpha-decay fine structure combined with the gamma and conversion electrons spectroscopy.

Aim: Main goal of this work is to study alpha decay fine structure of the 179Hg (experiment S17 at JYFL, Finland). The second part will be dedicated to study of alpha-decay fine structure of the 177Au (experiment JR115, Finland). In both experiments, data from the focal plane
of the RITU separator will be analysed.

Literature:

[1] Rowe, D. J. (2010). Nuclear Collective Motion: Models and Theory. Singapore: World Scientific Publishing Company. ISBN: 978-981-279-065-1.
[2] Rowe, D. J., Wood, J. L. (2010). Fundamentals of Nuclear Models: Foundational Models. World Scientific Publishing Company. ISBN: 978-9812569561.
[3] Veselský, M. (2014). Nuclear reactions with heavy ion beams. LAP LAMBERT Academic Publishing. ISBN: 978-3659211058.
[4] F.G. Kondev et al., First observation of excited structures in neutron-deficient 179Hg: evidence for multiple shape coexistence. Physics Letters B 528, 221-227 (2002).
[5] P. Peura et al., Quasiparticle alignments and α-decay fine structure of 175Pt. Physical Review C 89, 024316 (2014).
[6] M. Venhart et al., New systematic features in the neutron-deficient Au isotopes. Journal of Physics G: Nuclear and Particle Physics 44, 074003 (2017).
[7] V. Matoušek et al., TATRA: a versatile high-vacuum tape transportation system for decay studies at radioactive-ion beam facilities. Nuclear Instruments and Methods in Physics Research Section A 812, 118-121 (2016)

Tutor:	Mgr. Andrej Herzáň, PhD.
Department:	FMFI.KJFB - Department of Nuclear Physics and Biophysics
Head of department:	prof. RNDr. Jozef Masarik, DrSc.

Comenius University Bratislava
Faculty of Mathematics, Physics and Informatics

Assigned: 08.08.2019

Approved: 08.08.2019 prof. RNDr. Jozef Masarik, DrSc.
Guarantor of Study Programme

.....
Student

.....
Tutor

Univerzita Komenského v Bratislave
Fakulta matematiky, fyziky a informatiky

ZADANIE ZÁVEREČNEJ PRÁCE

Meno a priezvisko študenta: Mgr. Andrej Špaček
Študijný program: jadrová a subjadrová fyzika (Jednoodborové štúdium, doktorandské III. st., denná forma)
Študijný odbor: fyzika
Typ záverečnej práce: dizertačná
Jazyk záverečnej práce: anglický
Sekundárny jazyk: slovenský

Názov: Decay spectroscopy of neutron-deficient isotopes 179Hg and 177Au
Rozpadová spektroskopia neutrónovo-deficitných izotopov 179Hg a 177Au

Anotácia: Stavy s nízkym a stredným spinom sú nositeľmi dôležitej informácie o jadrovej štruktúre, napr. vývoj deformácie a fenomén známy ako tvarová koexistencia. Tieto stavy sú ale často tzv. non-yrast, čo znamená, že pravdepodobnosť ich populovania metódou in-beam gama spektroskopie je nízka. V prípade exotických ťažkých jadier sú metódy rozpadovej spektroskopie častokrát jediným spôsobom, ako získať potrebnú informáciu s dostatočnou presnosťou. Jedným z príkladov je štúdium jemnej štruktúry alfa premeny kombinovanej so spektroskopiou gama kvánt a konverzných elektrónov.

Cieľ: Práca bude rozčlenená na dve časti. V prvej časti je cieľom štúdium jemnej štruktúry alfa premeny izotopu 179Hg (experiment S17 v JYFL, Fínsko). Druhá časť bude venovaná štúdiu jemnej štruktúry alfa premeny izotopu 177Au (experiment JR115 v JYFL, Fínsko). V obidvoch experimentoch budú analyzované dáta z fokálnej rovivny separátora RITU.

Literatúra:

Školiteľ: Mgr. Andrej Herzáň, PhD.
Katedra: FMFI.KJFB - Katedra jadrovej fyziky a biofyziky
Vedúci katedry: prof. RNDr. Jozef Masarik, DrSc.

Dátum zadania: 08.08.2019

Dátum schválenia: 08.08.2019 prof. RNDr. Jozef Masarik, DrSc.
garant študijného programu

.....
študent

.....
školiteľ

Declaration of Authorship

I, Mgr. Andrej Špaček, declare that this thesis titled, "Decay spectroscopy of neutron-deficient isotopes ^{179}Hg and ^{177}Au", and the work presented in it are my own. I confirm that:

- This work was done wholly or mainly while in candidature for a research degree at this University.
- Where I have consulted the published work of others, this is always clearly attributed.
- Where I have quoted from the work of others, the source is always given. With the exception of such quotations, this thesis is entirely my own work.
- I have acknowledged all main sources of help.

Signed:

_____

Date:

_____

Univerzita Komenského v Bratislave
Fakulta Matematiky, Fyziky a Informatiky

Abstrakt

Philosophiae Doctor

Rozpadová spektroskopia neutrónovo deficitných izotopov ^{179}Hg a ^{177}Au

Mgr. Andrej Špaček

Alfa rozpad je vynikajúci nástroj na štúdium exotických jadier, a to aj ďaleko od línie beta stability. Okrem toho jemná štruktúra alfa premeny umožňuje štúdium nízkoenergetických vzbudených stavov v takýchto jadrách, ktorých produkcia je komplikovaná kvôli nízkym účinným prierezom. Táto práca prezentuje výsledky štúdia jemnej štruktúry alfa rozpadu dvoch neutrónovo deficitných jadier ^{179}Hg and ^{177}Au. Dáta boli namerané počas dvoch experimentov s kódovým označením S17 a JR115 v urýchľovačovom laboratóriu Univerzity v Jyväskylä, Fínsko. Aparatúta oboch experimentov bola zložená z poľa detektorov Jurogam 2, Ritu separátora a GREAT spektrometra. Po prvý krát bola pozorovaná jemná štruktúra alfa rozpadu v ^{179}Hg. Na základe experimentálne určeného konverzného koeficientu 131,3 keV prechodu mu bola priradená $M1$ multipolarita. Tak isto bola identifikovaná jemná štruktúra v alfa rozpade ^{177}Au. Tri nové prechody s energiou 156,1 keV, 215,1 keV a 134,5 keV, boli priradené ^{173}Ir. Taktiež bola vykonaná analýza zvyšných promptných aj oneskorených alfa - gama koincidencií.

Comenius University in Bratislava
Faculty of Mathematics, Physics and Informatics

Abstract

Philosophiae Doctor

Decay spectroscopy of neutron-deficient isotopes ^{179}Hg and ^{177}Au

Mgr. Andrej Špaček

The α decay is a powerful tool to study exotic nuclei, including far from the β stability line. Moreover, the α-decay fine structure allows the study of low-lying excited states in these nuclei that are dificult to populate due to low reaction cross-section. This thesis presents the results of α-decay study of two neutron-deficient nuclei ^{179}Hg and ^{177}Au. Data were acquired during two experiments performed at the Accelerator Laboratory of the University of Jyväskylä, Finland. Both experiments comprised of Jurogam 2 array, the RITU separator and GREAT spectrometer. The fine-structure in the α decay of ^{179}Hg was observed for the first time. The $M1$ multipolarity was assigned to the 131.3 keV transition based on the experimentally deduced conversion coeficient. Additionally, the fine structure of the ^{177}Au was identified. Three new transitions with energies of 156.1 keV, 215.1 keV and 134.5 keV were assigned to the ^{173}Ir. Finally, the analysis of the other prompt and delayed α-γ coincidences was performed.

Acknowledgement

I would like to express my deepest appreciation to my supervisor Andrej Herzáň for his tremendous patience, optimistic approach, support and friendship. Your guidance helped me throughout all of my PhD. studies. Your advices along with prompt feedback ensured the completion of my thesis. You made me realize that if I ever want to be a proper scientist I need to improve not only my knowledge but also the formulation of my ideas.

I also could not have undertaken this journey without my former supervisor Martin Venhart. Your enthusiasm for nuclear physics drew me to this beautiful field. Especially since you gave me an opportunity to participate in the alluring experiment IS521 in CERN even though I was only a bachelor student.

I would like to extend my sincere thanks to my colleagues Matúš Balogh, Matúš Sedlák, Vlado Matoušek for your help with ROOT, GRAIN, HDTV and for help with simulations. I am also grateful to the rest of my colleagues Monika Bírová, Gulnur Kantay, Anton Repko and Sebastian Vielhauer for the discussions, editing help and advices throughout my studies.

I would be remiss in not mentioning my familly. Their belief in me has kept my spirits and motivation high during all of my studies. I'd also like to recognize my friends who always found a way to keep my spirit high and helped me unwind when I was overwhelmed. Special thanks goes to my roommates who were able to listen to everything related to my work.

Contents

List of Figures

List of Tables

List of Abbreviations

ADC	**A**nalog-to-**D**igital **C**onverter
BGO	**B**ismuth **G**ermanium **O**xide
CFD	**C**onstant **F**raction **D**iscriminators
DAQ	**D**ata **A**c**Q**uisition system
DSSD	**D**ouble-sided **S**ilicon **S**trip **D**etector
FPGA	**F**ield-**P**rogrammable **G**ate-**A**rray
FWHM	**F**ull **W**idth at **H**alf **M**aximum
GREAT	The **G**amma **R**ecoil **E**lectron **A**lpha **T**agging Spectrometer
HF	**H**indrance **F**actor
HPGe	**H**igh **P**urity **Ge**rmanium
JYFL	**J**yväskylän **Y**liopisto **F**ysiikan **L**aitos (Univeristy of Jyväskylä, Department of Physics)
MWD	**M**oving **W**indow **D**econvolution
MWPC	**M**ulti**W**ire **P**roportional **C**ounter
RDT	**R**ecoil **D**ecay **T**agging
RITU	**R**ecoil **I**on **T**ransport **U**nit
SAGE	**S**ilicon **A**nd **GE**rmanium spectrometer
TAC	**T**ime to **A**mplitude **C**onverter
TDR	**T**otal **D**ata **R**eadout
W.u.	**W**eisskopf **u**nits

Introduction

The general goal of nuclear physicists is to understand the atomic nucleus. For this purpose it is necessary to develop a model that will explain different processes in nuclei and will be able to predict their behaviour. Nowadays, experimental physicists study many different phenomena ($e.g.$ shell evolution, nuclear deformations and shape coexistence). Various macroscopic and microscopic models of the atomic nucleus are currently available. However, each of those models is applicable to only a certain mass region of the chart of nuclei or to a specific feature of the atomic nucleus. Developing a universal model that will be able to explain all observed phenomena requires a systematic study of isotopes.

The study of α decays provides helpful insights to the underlying nuclear structure [1–3] and nuclear deformations [4–6]. Coupled with hindrace factors (*HF*), they form powerful tool for the identification of low-lying states in very neutron-deficient nuclei. Moreover, direct information on the excitation energy and configuration of the observed states can be obtained. In order to study heavy neutron-deficient nuclei, efficient and selective techniques must be deployed due to the extremely small production cross section and short half-lifes. In-flight separator combined with efficient decay spectrometer is one of the commonly used techniques.

The work presented here is focused mainly on the study of α-decay fine structure in ^{179}Hg and ^{177}Au. Both isotopes are extremely-neutron deficient since they are 17 and 20 neutrons away from the closest stable isotope. The study of the α-decay fine structure is a powerful tool to study properties of low-lying excited states, which are difficult to populate this far from the β stability line. The studied isotopes were produced during two experiments with code names S17 and JR115. Both experiments took place at the Accelerator Laboratory of the University of Jyväskylä (JYFL), Finland. The products of fusion evaporation reaction were separated with the RITU separator [7]. The focal plane data were measured with the GREAT spectrometer [8]. the Total Data Readout system (TDR) was used to collect data.

Events of interest were separated with standard tagging techniques [9, 10].

The focus of the data analysis from the S15 experiment is the study of ^{179}Hg α decay based on recent results in the α decay of ^{175}Pt [11]. A new α-decay branch was observed in ^{179}Hg. Alpha-decay characteristics of the newly observed branch were extracted from the experimental data. Owing to the presence of K_β x rays in the focal plane detectors, it was possible to extract the multipolarity of 131.3 keV γ-ray transition depopulating the newly observed α decay branch in ^{179}Hg. To confirm our findings a Geant4 simulation was performed. The goal of data analysis from the second experiment, JR115, was the focal-plane decay spectroscopy. There, the α decay fine structure of ^{177}Au is presented. A new α-decay branch along with new γ transitions from excited states populated by different α decays are discussed. Analyses of other prompt and delayed α-γ coincidences observed in focal plane of the RITU separator are presented.

Chapter 1

Theoretical background

1.1 Nuclear models

The nucleus is an example of the finite many-body quantum system. It is composed of *N* neutrons and *Z* protons, bound together to form the mass number *A*. The nucleons in atomic nucleus are subjected to the strong nuclear interaction and Coulomb interaction. Multiple models of atomic nucleus have been developed. They all share the same goal, which is to be able to describe and explain nuclear forces and features of nuclei. In this chapter, the most commonly used models will be introduced. In these models, nucleons will be considered to be point particles. This means that their internal structure will be neglected along with the phenomena associated with it.

1.1.1 Liquid drop model

One of the first models considered was the liquid drop model, invented by George Gamow in years 1928-1931 and later refined by Carl Friedrich von Weizsäcker in 1935 [12]. This model takes the nucleus as a drop of uniform liquid and regards the nucleons on the surface as if subjected to different forces than those in the interior, similarly to the surface tension of the liquid drop. The volume of this drop is proportional to the mass of the nucleus A. The greatest contribution of this model is the Bethe-Weizsäcker semi-empirical formula for calculating the binding energy of the nucleus:

$$B(A,Z) = a_V A - a_S A^{\frac{2}{3}} - a_C \frac{Z^2}{A^{\frac{1}{3}}} - a_A \frac{A-2Z}{A} + a_P \frac{((-1)^Z + (-1)^N)}{2A^{\frac{1}{2}}} \tag{1.1}$$

where the first term is called the volume term and it is calculating the short-distance strong nuclear force, in a sense that one nucleon can be only bounded by the nucleons around it. The second (surface) term plays a role of a correction to the volume term, meaning nucleons at the surface have fewer neighbours, and it also creates a mechanism similar to surface tension. The third (coulomb) term takes into account the repulsions of the protons. The fourth (asymmetry) term comes from Pauli exclusion principle as it allows only two protons or neutrons with different spins on the same level. When the number of neutrons and protons is not equal, higher energy levels are filled by one particle, while the lower energy levels are vacant for the other type of particles. The last (pairing) term considers spin coupling, and it creates greater binding energy (more stable nucleus) when the nucleus has even number of nucleons with even number of neutrons, and lower binding energy when the nucleus has even number of nucleons with odd number of neutrons. The advantages of the liquid drop model are: it explains the spherical shape of most nuclei, it gives a good approximation for atomic masses and it gives basis for understanding fission. However, it fails to predict greater binding energy at certain numbers of protons/neutrons (magic numbers), the effect of nucleon pairing or the properties of deformed nuclei [13].

1.1.2 Nuclear mean-field theory

Since most nuclei are composed of larger number of nucleons and the A-nucleon Schrödinger equation cannot be solved exactly in such cases, it is necessary to use another method, such as mean-field approximation. In this method, the strongly interacting system is replaced with weakly interacting quasiparticles (a physical concept, which treats collection of quantum characteristics among particles, like a hole after the emission of an electron in atomic physics, as particles). For this transformation, mean-field quasiparticles are introduced. The Hamiltonian H is composed of kinetic energy T and potential energy V. In many-body system it is written as:

$$H = T + V = \sum_{i=1}^{A} t(r_i) + \sum_{\substack{i=1,j=1 \\ i<j}}^{A} v(r_i, r_j) = \sum_{i=1}^{A} -\frac{\hbar^2}{2m_N}\nabla_i^2 + \sum_{\substack{i=1,j=1 \\ i<j}}^{A} v(r_i, r_j), \qquad (1.2)$$

where m_N represents the mass of a nucleon, whereby protons and neutrons have the same mass and r_i represents the coordinates of the i'th nucleon. If the single particle potential

energy is summed, it will change into:

$$H = \left[T + \sum_{i=1}^{A} v(r_i)\right] + \left[V - \sum_{i=1}^{A} v(r_i)\right] \equiv H_{MF} + V_{RES}; \tag{1.3}$$

where H_{MF} is the nuclear mean-field Hamiltonian and V_{RES} is the mean-residual interaction, which is weaker compared to the original interaction V. They are expressed as:

$$\begin{aligned} H_{MF} &= T + \sum_{i=1}^{A} v(r_i) \equiv T + V_{MF} = \sum_{i=1}^{A} [t(r_i) + v(r_i)] \equiv \sum_{i=1}^{A} h(r_i) \\ V_{RES} &= V - \sum_{i=1}^{A} v(r_i) = \sum_{\substack{i=1,j=1 \\ i<j}}^{A} v(r_i, r_j) - \sum_{i=1}^{A} v(r_i) \end{aligned} \tag{1.4}$$

While using mean-field approximation it is assumed that *A-1* nucleons create an external field through which a nucleon is moving. In this case the V_{MF} is considered as time average of interaction between the nucleon and its neighbours, which are described by non-correlated single-particle wave functions (for fermions, these are arranged in a Slater determinant). This method is therefore capable of reducing the strongly-interacting many-fermion system into a system of non-interacting quasi-particles placed in external potential $v(r)$. In this approach, the use of Schrödinger equation results in single-particle wave function as if calculating Schrödinger equation for one nucleon in an external field. The only problem is that the optimal field, with minimalized residual interaction between quasiparticles needs to be determined. The goal is to obtain optimal set of $\{\phi_\alpha(r)\}$, which can be done by minimizing the ground-state energy of the nucleus and using method of Lagrange undetermined multipliers. This will lead to Hartree(-Fock) equation:

$$\begin{aligned} \frac{-\hbar^2}{2m_N}\nabla^2\phi_\alpha(r) + V_{H(F)}(\phi_i(r_i))\phi_\alpha(r) &= \epsilon_\alpha\phi_\alpha(r); \\ i = 1, 2, ..., A, \qquad \alpha &= 1, 2, ..., \infty. \end{aligned} \tag{1.5}$$

which resembles Schrödinger equation, except that the potential $V(r)$ is replaced with a functional $V_{H(F)}$ with unknown wave functions $(\phi_i(r))$. However this mean-field potential depends mainly on radius of the nucleus *r* charge *Z* and mass number *A*. The formula 1.5 is usually used with only one particular type of potential. The most common types of potentials are discussed in the section below.

1.1.3 Spherical shell model

The nuclear shell model belongs to the most developed and understood models of the nucleus. It is based on the Pauli exclusion principle and it describes the nuclear structure in the form of energy levels analogous to the atomic orbit. The model explains energy gaps (an effect when the nucleus needs more excitation energy for a nucleon to go into a higher shell). These energy gaps occur with certain number of protons or neutrons, the so-called *magic numbers* (specifically 2, 8, 20, 28, 50, 82, 126) and the shell model explains them as fully occupied shells or closed shells. Evidence for the closed shells comes, $e.g.$, from observation of energy gaps in two-neutron (two-proton) separation energies, see Fig 1.10 in [14]. The shell model is based on principle that it is possible to write the nuclear Hamiltonian as a sum of independent-particle Hamiltonian plus the residual interaction V_{RES},

$$H = \sum_{i=1}^{A} \left[\frac{p_i^2}{2M} U(r_i) \right] + V_{RES} \tag{1.6}$$

where p_i represents the momentum of *i*'th nucleon, M represents the mass of the nucleus, r_i is the position vector for *i*'th nucleon and U represents the potential for the central single-particle field. Since the atomic nucleus does not have a well-defined centre, it is necessary to select a right single-particle potential. The nuclear forces are very attractive but only at a very short distance ($\approx$ 1 fm). In greater distances this attraction drops exponentially, so the first potential to consider is the infinite square-well potential (equation 1.7). The second considered potential, is the harmonic oscillator (equation 1.8), but these two potentials are unrealistic, for they have infinite walls and they give wrong magic numbers. More realistic single-particle potential can be calculated from the Wood-Saxon potential (equation 1.9). This single-particle potential is based on a mean single-particle field, which follows a nucleon density distribution in an experimentally determined nucleus. Unfortunately the disadvantage of the third potential is that it can not be solved analytically. The equation for infinite square potential is:

$$U(r) = \begin{cases} -V_0 & \text{if } r < R \\ \infty & \text{if } r \geq R \end{cases} \tag{1.7}$$

The harmonic oscillator potential is defined as:

$$U(r) = -V_0 \left[1 - \frac{r^2}{R^2}\right] \tag{1.8}$$

and the equation used to calculate Wood-Saxon potential is:

$$U(r) = \qquad -V_0 \Big\{1 + \exp\left(\frac{r-R}{a}\right)\Big\}^{-1} \tag{1.9}$$

For these equations, V_0 represents the depth of the potential well, a is the surface thickness, r represents the distance from the centre and R represents the radius of the nucleus. Even at this point, the shell model still fails in the correct reproduction of the experimentally observed magic numbers. To overcome this problem, in 1963 Maria Geoppert Mayer [15] and J. H. D. Jensen [16] have recieved the Nobel Price for the discovery of strong spin-orbit interaction present for each nucleon. This was finally found to be a missing term, which helped physicists to reproduce the correct magic numbers. The spin-orbit term is expressed as follows:

$$\hat{H}_{SO} = \xi \overrightarrow{l} . \overrightarrow{s}, \tag{1.10}$$

where ξ is an empirical parameter (usually negative), $\overrightarrow{l}$ represents the orbital angular momentum and $\overrightarrow{s}$ is the intrinsic spin of the nucleon. The whole influence of these calculations can be seen in Fig. 1.1.

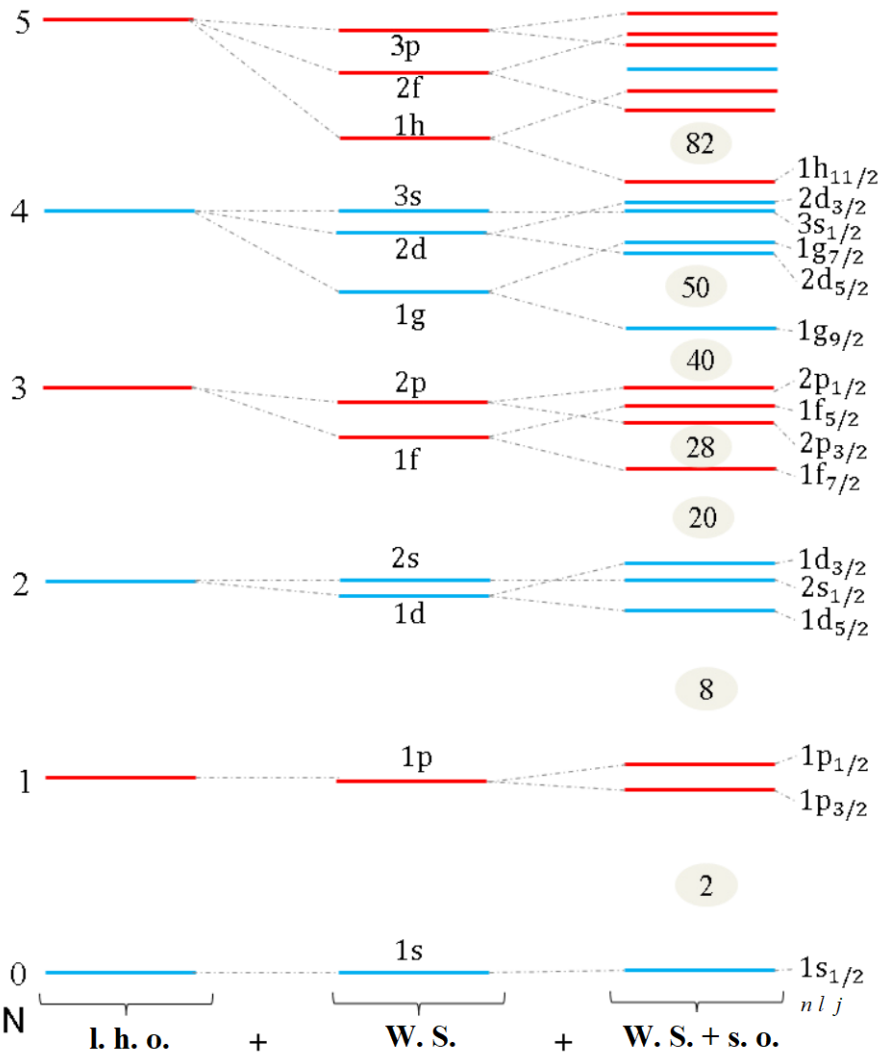

Figure 1.1: Representation of energy levels for the linear harmonic oscillator (l.h.o.), and Wood-Saxon (W.S.) potential without and with spin-orbit interaction (s.o.). Positive parity levels are marked by blue colour and negative parity levels are identified by red colour. Figure taken from [17].

In this figure, N is the main quantum number, l is orbital angular momentum and j is total angular momentum, which can be calculated as j=l+s. The number in circle shows correct magic numbers. When the number of nucleons in a nucleus forms a closed shell and one nucleon is added or removed, a single-particle behaviour can be assumed. This can be tested on nuclei with doubly-closed shells, such as ${}^{4}_{2}\mathrm{He}$, ${}^{16}_{8}\mathrm{O}$, ${}^{40}_{20}\mathrm{Ca}$, ${}^{48}_{20}\mathrm{Ca}$, ${}^{56}_{28}\mathrm{Ni}$, ${}^{132}_{50}\mathrm{Sn}$ and ${}^{208}_{82}\mathrm{Pb}$, with odd-mass nuclei in their close proximity. However the disadvantage of the shell model is that it breaks down when an excited nucleon pairs with another nucleon in higher shell. The formation of such pair which will in turn lower the energy of the state due to pairing correlations. Such effect may cause an intrusion of excited states across the closed

shell. An example of the intruder state according to the shell model calculation is the $1f_{7/2}$ state in ^{39}Ca and ^{39}K, see Fig. 1.2. Nonetheless it is an exceptional model when some of the nucleons can be characterized as the core plus independent particles [18].

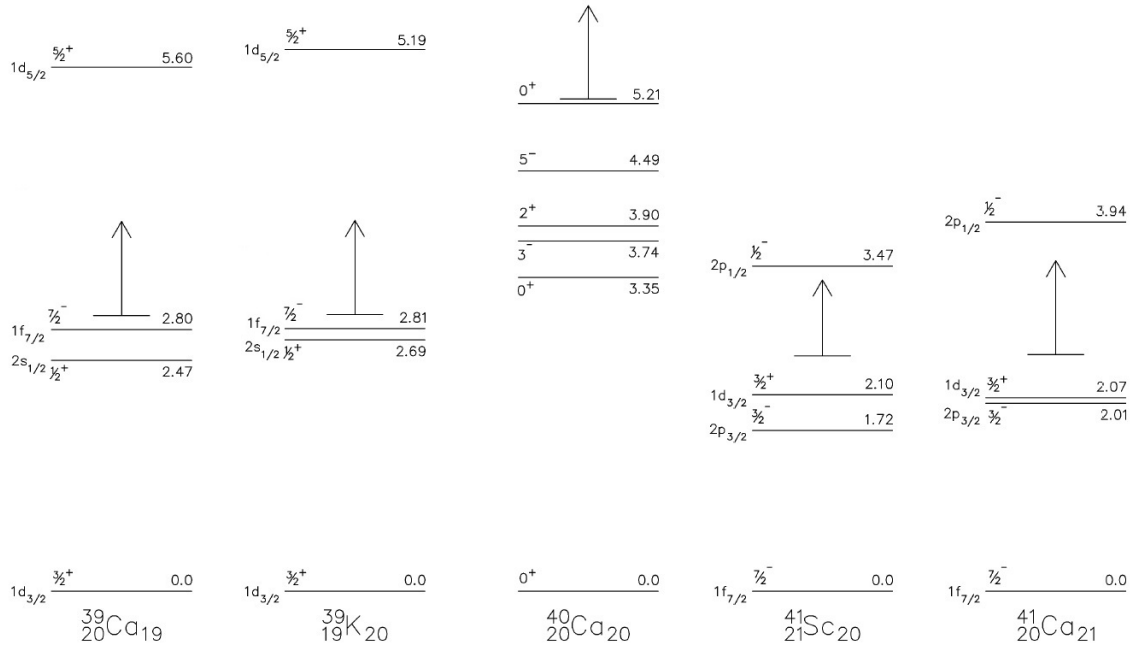

Figure 1.2: Single-hole and single-particle states in neighboring ^{40}Ca isotopes. Figure taken from [14].

1.1.4 Deformed nuclei

The shell model discussed above is useful when the nuclei are spherical or near-spherical. When the nucleus starts to be deformed (nuclei far from closed shells), it fails to predict its behaviour, because the forces between valence nucleons will result in collective motions. The most common type of deformation observed in nuclei is the quadrupole deformation. There are two types of quadrupole deformation: when nucleus is prolate (nucleus is in the form of rugby ball), and oblate (nucleus is in the form of a disk), see Fig. 1.3. The deformation of nuclei can be determined by measuring the intrinsic quadrupole moment Q_0, where $Q_0 = 0$ suggests a spherical nucleus and $Q_0 > 0$, $Q_0 < 0$ suggests prolate and oblate shape of nucleus, respectively. In even-even nuclei the first excited state is the 2^+ state, which will de-excite to 0^+ state, and the quadrupole moment is related to the reduced transition probability $B(E2)$ as:

$$Q_0 = \left[\frac{16\pi}{5}\frac{B(E2)e^2b^2}{e^2}\right]^{1/2} \tag{1.11}$$

This reduced transition probability $B(E2)$ includes information about the structure of the nucleus complementary to our knowledge of low-lying levels in nuclides. According to the Global Best Fit systematic, the reduced transition probability B(E2)↑ in e^2b^2 can be calculated as [19]:

$$B(E2)\uparrow = 2.6E^{-1}Z^2A^{-2/3} \tag{1.12}$$

where E^{-1} is the excitation energy in keV. The advantage is, that B(E2)↑ values are independent on nuclear models. The shape of axially symmetric nucleus can be described by quadrupole deformation parameter β_2 and it is related to the quadrupole moment as:

$$\beta_2 = \frac{Q_0\sqrt{5\pi}}{3ZR^2} \tag{1.13}$$

where R is the radius of the nucleus expressed as:

$$R = 1.2A^{1/3} \tag{1.14}$$

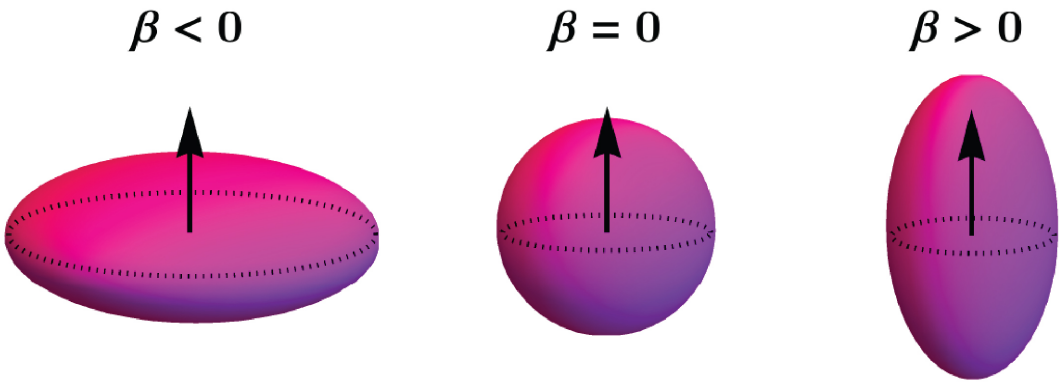

Figure 1.3: Examples of axially-symmetric deformations: (left) oblate shape, (center) sphere and (right) prolate shape. Arrows on prolate and oblate shape denote symmetry axis. Figure taken from [20].

1.1.5 Nilsson model

In 1953, S.G. Nilsson developed a new version of the single-particle shell model, the so-called Nilsson model [21]. As an extension of the deformed shell model, it gives description of new experimental observations on single-particle levels in deformed nuclei, such as ground state spins and parities of a large number of nuclei. The Wood-Saxon potential is

replaced by spheroidal potential, which can be expressed, e.g., in a form:

$$V = \frac{m(\omega_\perp^2(x^2+y^2)+\omega_z^2 z^2)}{2} - \kappa\hbar\omega_0[2\overrightarrow{l}\cdot\overrightarrow{s}+\mu l^2] \tag{1.15}$$

where $\omega_\perp = \omega_0(1+\frac{2}{3}\epsilon)$, $\omega_z = \omega_0(1+\frac{4}{3}\epsilon)$, ω_0 is the spherical oscillator frequency, parameters κ and μ adjust strength of $l\cdot$s and l^2 terms, and ϵ represents Nilsson deformation parameter. The parameter $\epsilon > 0$ suggests prolate and $\epsilon < 0$ oblate ellipsoid, respectively. The relation between ϵ and the parameter of quadrupole deformation β_2 can be expressed as:

$$\epsilon \approx \frac{\Delta R}{R_0} = \frac{3}{4}\sqrt{\frac{5}{\pi}}\beta = 0.946\beta \tag{1.16}$$

where ΔR is the difference between major (R_z) and minor (R_x) axis of ellipsoid and R_0 is the radius of a sphere with the same volume as the ellipsoid. The quantum numbers acquired from the spherical shell model are not good quantum numbers anymore, and a new set of quantum numbers needs to be defined. The reason is that deformed nuclei have three distinct symmetry and rotational axes, contrary to spherical nuclei. Nilsson therefore introduced new quantum numbers, such as n_z, K along with projections of original quantum numbers onto the symmetry axis, such as Λ, Σ, Ω, where n_z is the number of oscillator quanta along the direction of symmetry axis, K is the projection of the total angular momentum J of the nucleus onto the symmetry axis and Λ is the projection of orbital angular momentum l, Σ is the projection of the intrinsic spin s and Ω is the projection of total angular momentum of the odd particle j. The scheme of these quantum numbers in deformed nucleus is shown in Fig. 1.4. The effect of splitting the single-particle energy levels as a result of change in deformation parameter is depicted in Nilsson diagrams, as shown in Figs. 1.5, 1.6. In the Nilsson diagram, single-particle energy levels are characterized by a set of four quantum numbers: $\Omega[Nn_z\Lambda]$, where N is the total oscillator shell quantum number.

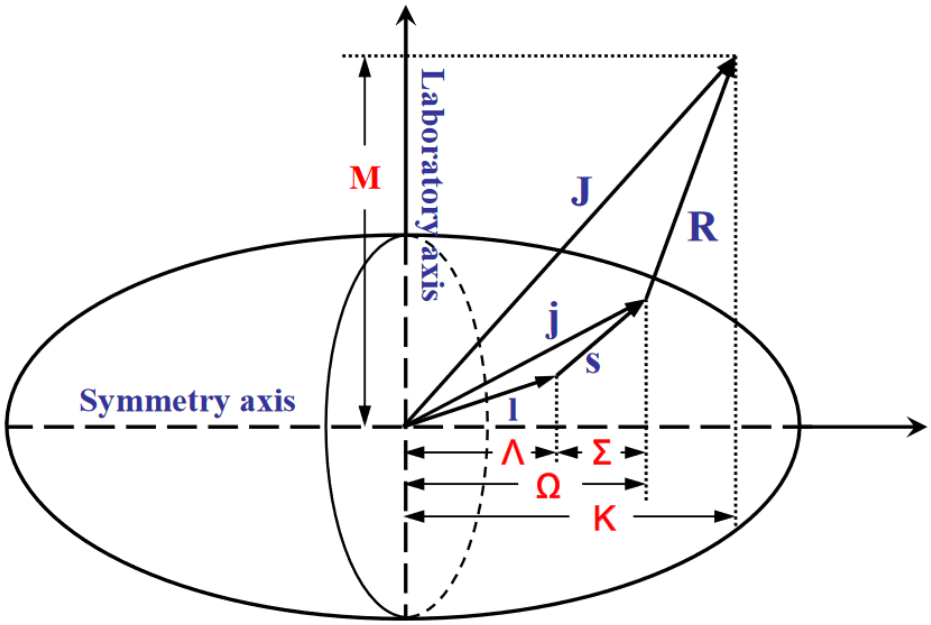

Figure 1.4: Graphic representation of asymptotic quantum numbers valid for deformed nuclei. Here quantum numbers M, K represent projections of the total angular momentum J of the nucleus onto laboratory (axis of rotation) and symmetry axis. R denotes total angular momentum of the core (collective rotations), while Λ, Σ and Ω are projection of the orbital angular momentum l, intrinsic spin s, and total angular momentum of the odd particle j [22].

1.2 Nuclear decay modes

Whenever the nucleus is in the excited state or lies off the β-stability line, it is subjected to radioactive decay. Radioactivity or radioactive decay is a statistical process, governed by an exponential law. The law defines the number of remaining radioactive nuclei present in the sample at time t as:

$$N(t) = N_0 e^{-\lambda_d t} \tag{1.17}$$

where N_0 is the number of radioactive nuclei at time zero and λ_d is the so-called decay constant. The activity A of the sample at time t can be then defined as:

$$A(t) = A_0 e^{-\lambda_d t} \tag{1.18}$$

The activity is given in the Becquerel unit, which is defined as one decay per second, and is related to the number of radioactive atoms as:

$$A(t) = \lambda_d N(t) \tag{1.19}$$

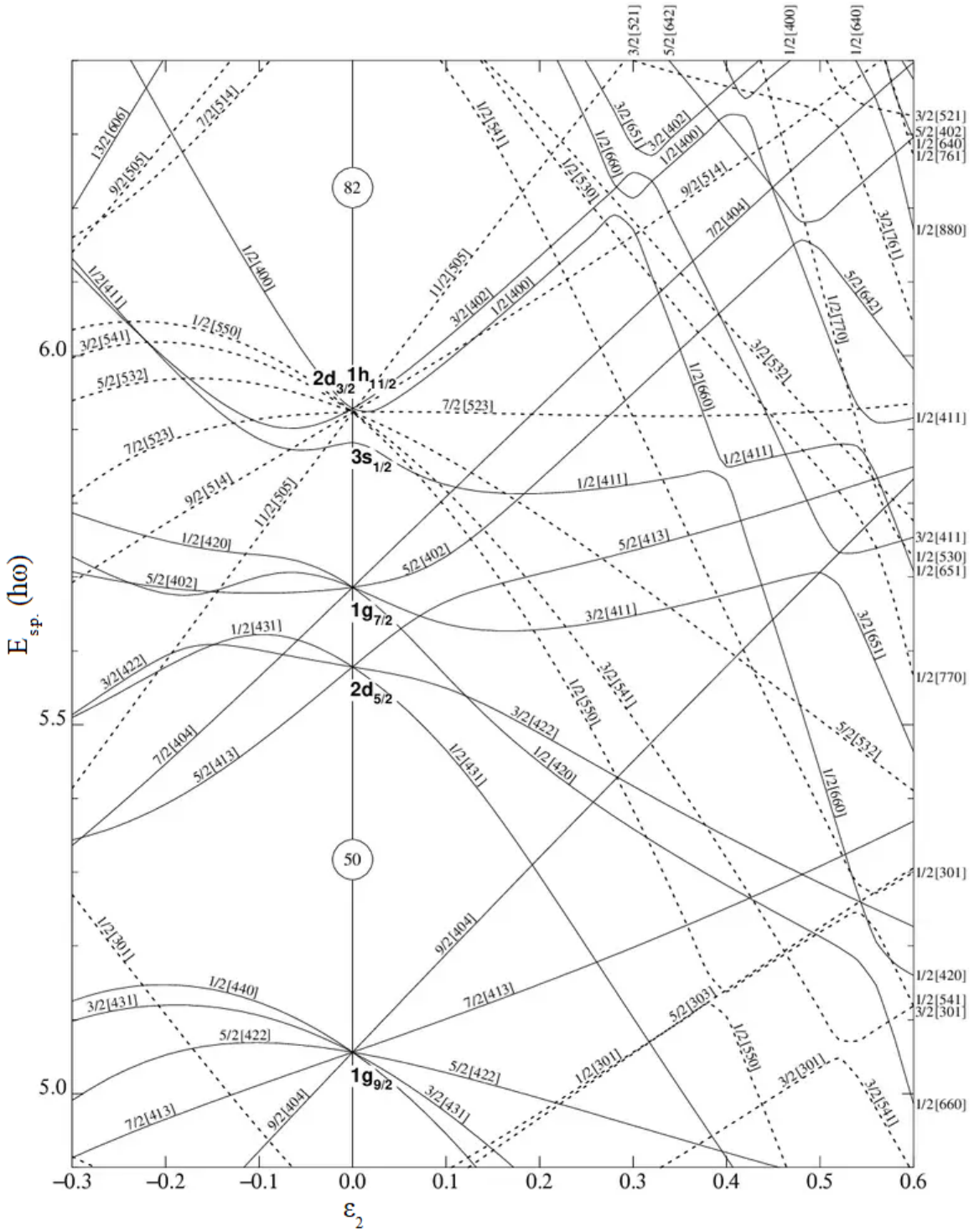

Figure 1.5: Splitting of energy levels as a function of deformation parameter for neutrons. The figure is taken from [23].

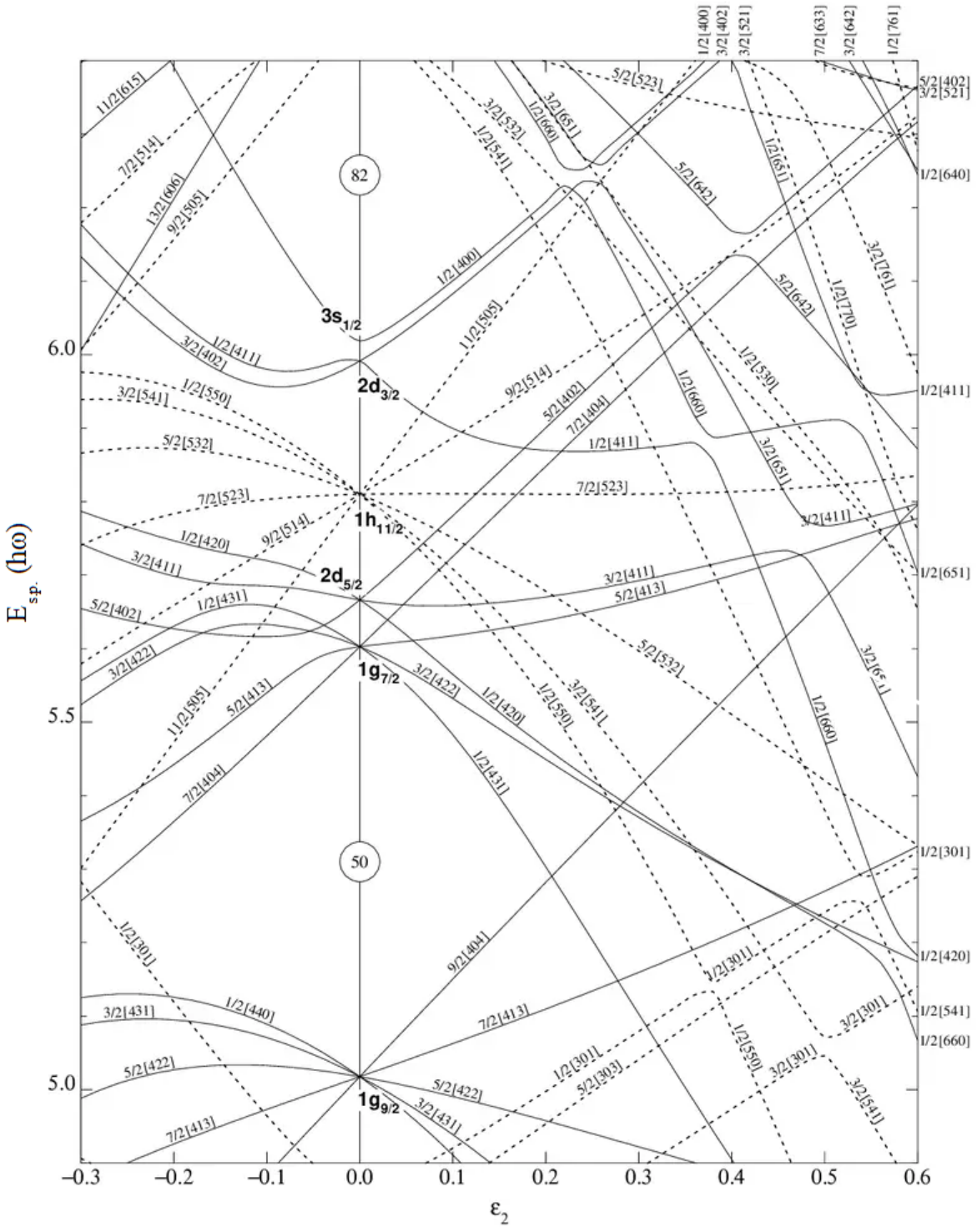

Figure 1.6: Splitting of energy levels as a function of deformation parameter for protons. The figure is taken from [23].

The most common term in nuclear physics is half-life, which determines time required for half of the sample to decay. The relation between half-life and decay constant is:

$$T_{1/2} = \frac{\ln(2)}{\lambda_d}. \tag{1.20}$$

For nuclei with multiple decay modes, the branching ratio b_i is established and it can be calculated as:

$$b_i = \frac{\lambda_{d,i}}{\lambda_d} \tag{1.21}$$

where $\lambda_{d,i}$ represents partial decay constant. With the branching ratio, a probability of the specific decay can be calculated.

In the very neutron-deficient nuclei of the present study, α decay is the dominant decay mode. By studying various types of nuclear decay, physicists can learn a lot about the behaviour and structure of that particular nucleus.

1.2.1 Alpha decay

In the α-decay process, the parent nucleus emits the so-called α particle. It is composed of two protons and two neutrons bound together, thus forming a system known as ${}^{4}_{2}He^{2+}$ nucleus. This process can formally be expressed in a form:

$${}^{A}_{Z}X_N \rightarrow {}^{A-4}_{Z-2}Y_{N-2} + {}^{4}_{2}He^{2+}_{2} + Q_\alpha \tag{1.22}$$

where X represents parent nucleus, Y denotes child nucleus, and Q_α is the total energy released in the α decay. The Q_α value can be calculated from the following equation:

$$Q_\alpha = (m_X - m_Y - m_\alpha)c^2 \tag{1.23}$$

This energy is divided between the kinetic energy of the child nucleus and the α particle.

$$T_\alpha = \frac{A-4}{A} Q_\alpha \tag{1.24}$$

Equation 1.24 defines the kinetic energy of the emitted α particle. From theoretical point of view, the α decay is a quantum tunneling of an α particle through (Coulomb) potential barrier [24]. It is schematically shown in Fig. 1.7. When the α particle carries out orbital

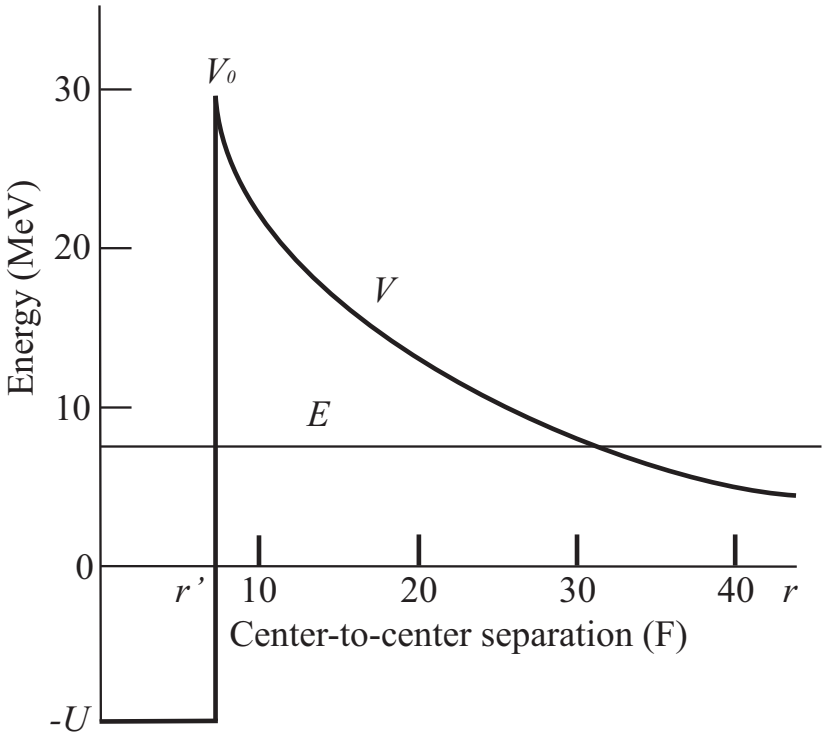

Figure 1.7: Schematic representation for α-decay tunnelling, where the potential between the child nucleus and α particle V is a square well with depth $-U$ and heigh being V_0. The α particle has total energy E. Figure adopted from [25].

angular momentum $l > 0$, the total potential is given as follows:

$$V(r) = \frac{1}{4\pi\epsilon_0}\frac{Z_\alpha(Z-2)e^2}{R} + \frac{\hbar^2 l(l+1)}{2\mu r^2} = \frac{1}{4\pi\epsilon_0}\frac{2e^2(Z-2)}{R_0(\sqrt[3]{A-4}+\sqrt[3]{4})} + \frac{\hbar^2 l(l+1)}{2\mu r^2} \quad (1.25)$$

where R_0 denotes the radius parameter of the nucleus (usually with value ≈ 1.2 fm), the first term is the Coulomb potential and the second term represents the centrifugal potential, in which a parameter μ denotes the reduced mass. The effect of adding the centrifugal potential to the definition describing the potential barrier can be seen in Fig. 1.8.

The barrier penetration probability of an α particle can be expressed as

$$P \approx \exp\left[-\left(\frac{2}{\hbar}\right)\int_0^d \sqrt{2m(V_0-E)}dr\right] = e^{-2G} \quad (1.26)$$

where d denotes the the width of the barrier and G is called Gamow factor, which (with considered approximation $r \ll R_c$, and R_c being the coordinate where $V(r)$ drops to value

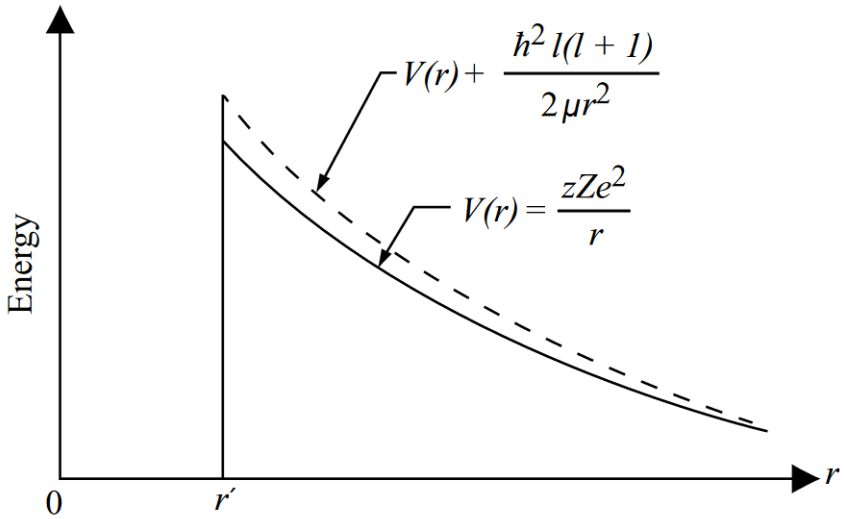

Figure 1.8: Schematic representation of barrier composed of only Coulomb potential and Coulomb coupled with centrifugal potential. Figure taken from [26].

of Q_α) is approximated by

$$G = 2\alpha Z\sqrt{\frac{2mc^2}{Q}}[cos^{-1}\sqrt{Q/V_0} - \sqrt{(Q/V_0)(1-Q/V_0)}], \tag{1.27}$$

whereby α is the fine-structure constant equal to 1/137, V_0 is the barrier height. The final expression for the probability of the emission of an α particle is:

$$\lambda_d = fe^{-2G}, \tag{1.28}$$

where f is the frequency with which the α particle is hitting the barrier. If the α particle is moving inside of the nucleus with speed:

$$v = \sqrt{\frac{2E_\alpha}{M}} \tag{1.29}$$

then f can be calculated as:

$$f = \frac{1}{2R}\sqrt{\frac{2E_\alpha}{M}} \tag{1.30}$$

where E_α represents the α-decay energy. The atom of helium is composed of two protons and two neutrons, therefore its spin equals zero, as both protons and neutrons occupy the 1s state. Not all of the transitions are permitted in α decay. The selection rules of α decay dictate which transition is permitted or forbidden. An α particle carries orbital angular momentum

l_α and the parity of a particle is derived from the angular wave function Y_{lm}, therefore the parity associated with α emission is defined by (-1)$^{l_\alpha}$. The selection rules can be written as follows: if $\pi_i = \pi_f$ then l_α must be even and if $\pi_i \neq \pi_f$ then l_α must be odd. [18]

1.2.1.1 Alpha-decay fine structure

The atomic nucleus can exists in different energy states. The lowest energy state is called the ground state and the rest are called excited states. Since the α decay is usually much slower than γ-ray emission, the parent nucleus is usually in the ground state. In case that an excited state is also long lived (a so called isomeric state in which the γ-ray emission is hindered), the α decay can depopulate an excited state. The α-decay fine-structure results from the possibility that other than the favoured state is populated by an α decay. An example of α decay populating several states in child nucleus is shown in Fig. 1.9. For the odd-A nuclei the Q-value of an α particle populating an excited state is:

$$Q_i = Q_{g.s.\rightarrow g.s.} - E_i^*, \tag{1.31}$$

where, Q_i is the Q-value of transition to *i*'th excited state, $Q_{g.s.\rightarrow g.s.}$ represents Q-value of α decay from ground state to ground state and E_i^* is the energy of *i*'th excited state in the child nucleus. Such process leads to observation of several distinguishable peaks in the spectra, generally called α-decay fine structure. The probability of which final state will be occupied is compromise between minimal change of the structure in the nucleus and maximal energy of the α particle [2]. In α decay we distinguish between unhindered (for example even-even isotopes connecting 0^+ states in parent and child nuclei) and hindered decays (the parent and child nuclei have different configurations, typically found in odd-A nuclei). The hindrance factor expresses the level of suppression of α decay. It indicates the difference of initial and final states in parent and child nuclei. The hindrance factor can be calculated as:

$$HF = \frac{T_{1/2\,exp}}{T_{1/2\,theor}}, \tag{1.32}$$

where $T_{1/2\,exp}$ is the experimental half-life of particular α decay and $T_{1/2\,theor}$ is the theoretical half-life, which can be calculated from equations 1.28 and 1.20. In general, the value of hindrance factor can be divided as follows:

- HF < 10: This is a so-called favoured transition. In this case the spin and parity of

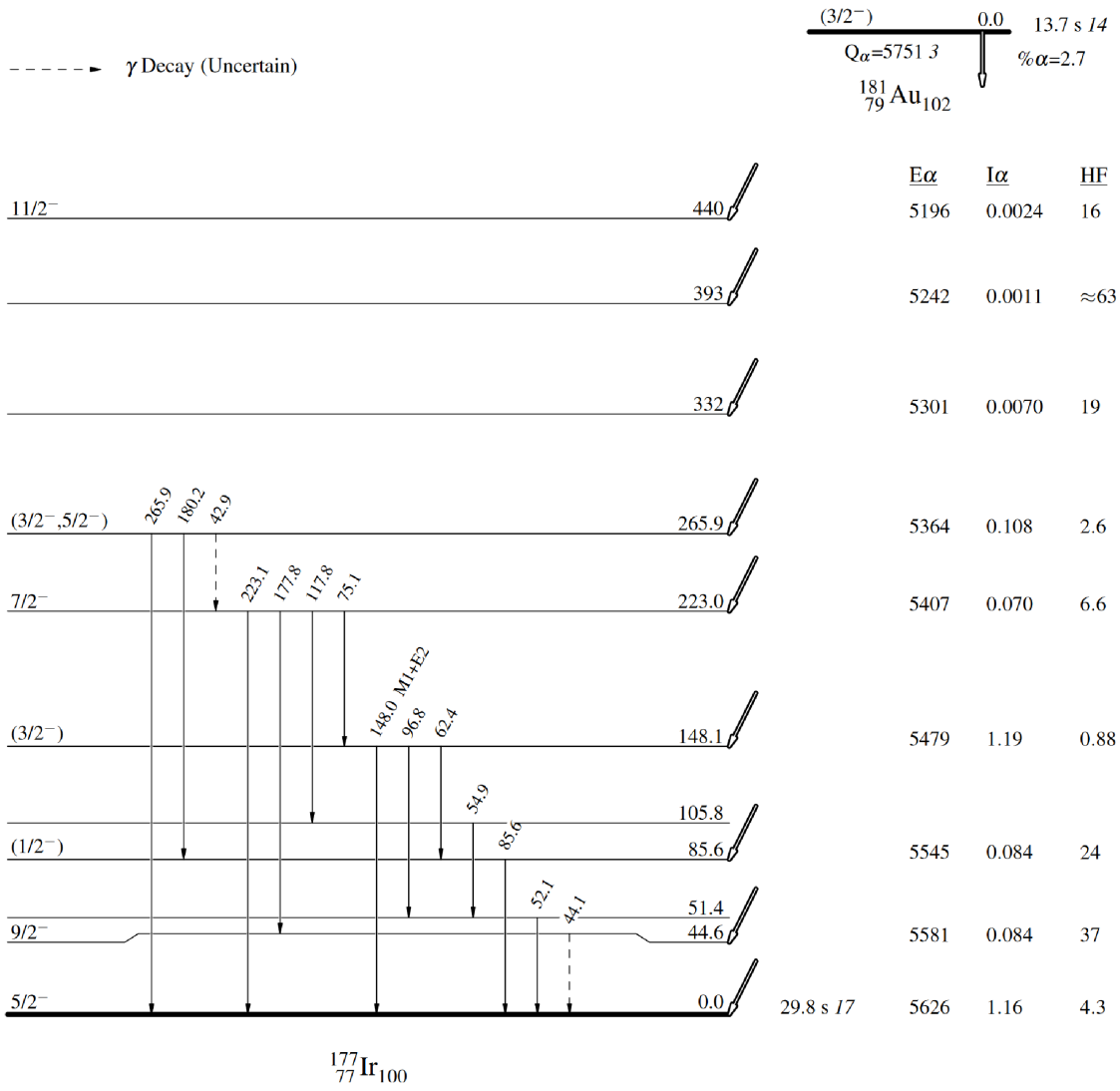

Figure 1.9: An example of α decay fine structure. The energies are displayed in keV. Figure taken from [27].

parent nucleus are the same as in the child nucleus.

- 10 < HF < 100: In α decays with in this range of hindrance factor, there is a spin difference between the parent and child nuclei.
- 100 < HF: transitions with value of the Hindrance factor in this range usually signify that the parity and spin of parent nucleus is different than in the child nucleus.

Finally the reduced α-decay width δ^2 can be obtained from the following expression:

$$\delta^2 = \frac{\lambda_\alpha^{exp}\hbar}{P}, \tag{1.33}$$

where λ_α^{exp} represent experimental α decay constant, $\hbar$ is the Planck's constant and P is the probability of barrier penetration according to the Rasmussen method [28]. Numerical calculations are required in order to obtain values of *HF* and δ^2.

1.2.2 Electromagnetic decay

In situation, when the excitation energy of the nucleus is not sufficient for evaporation of particles such as protons, neutrons, α particles, or the nuclear decay does not reach the ground state of the child nucleus, the nucleus can get rid of its energy excess via emission of electromagnetic radiation.

1.2.2.1 Gamma-ray emission

The process of de-excitation via γ-ray emission can be written as:

$$M_0^* c^2 = M_0 c^2 + E_\gamma + T_0, \tag{1.34}$$

where $M_0^*\mathrm{c}^2$ is the mass of the excited nucleus, $M_0\mathrm{c}^2$ is the mass of the nucleus after specific γ-ray emission, E_γ denotes energy of the emitted γ ray and T_0 is the kinetic energy of the recoiling nucleus. The energy factor, E_γ, plays an important role here, as will be shown later in the text [29]. In this process, the laws of conservation of angular momentum and parity dictate the selection rules, which define the electromagnetic character and multipolarity λ of the transition between the initial state with a spin and parity of I_i and π_i, and final state, I_f

π_f, of the nucleus. These rules can be written as follows:

$$|I_i - I_f| < \lambda < |I_i + I_f| \tag{1.35}$$

$$\begin{aligned} \pi(M\lambda) &= (-1)^{\lambda+1} \\ \pi(E\lambda) &= (-1)^{\lambda} \end{aligned} \tag{1.36}$$

where M and E denote magnetic and electric character of the transitions, respectively. It is obvious that not all multipoles may be emitted in particular transitions. Electric transitions are usually faster, and they are associated with the change of the charge density inside the nucleus, while magnetic transitions are mainly due to the current density. For example if $I_i = \frac{7}{2}^+$ and $I_f = \frac{1}{2}^+$, λ can take values 3 and 4 and since the parity did not change, the result multipolarity will be $M3$ or $E4$ [30].

The half-life of an nucleus de-exciting from an initial state i, to a final state f is:

$$T_{1/2} = \frac{\ln 2}{T_{fi}}. \tag{1.37}$$

where T_{fi} is the transition probability calculated as:

$$T_{fi}^{E\lambda} = 5.498 * 10^{22} f(\lambda) \left(\frac{E_\gamma[MeV]}{197.33} \right)^{2\lambda+1} B\left(E\lambda\right) [e^2 fm^{2\lambda}] 1/s, \tag{1.38}$$

$$T_{fi}^{M\lambda} = 6.080 * 10^{20} f(\lambda) \left(\frac{E_\gamma[MeV]}{197.33} \right)^{2\lambda+1} B(ML) [(\mu_N/c)^2 fm^{2\lambda-2}] 1/s, \tag{1.39}$$

$$f(\lambda) \equiv \frac{\lambda+1}{\lambda[(2\lambda+1)!!]^2}. \tag{1.40}$$

where $B(E\lambda)$ and $B(M\lambda)$ are reduced transition probabilities for the λ^{th} multipole electromagnetic transition. Experimental values of B are often given in the Weisskopf single-particle estimates [31] for reduced transition probabilities (B_W):

$$B_W(E\lambda) = \frac{1.2^{2\lambda}}{4\pi} \left(\frac{3}{\lambda+3} \right)^2 A^{2\lambda/3} e^2 fm^{2\lambda}, \tag{1.41}$$

$$B_W(M\lambda) = \frac{10}{\pi} 1.2^{2\lambda-2} \left(\frac{3}{\lambda+3} \right)^2 A^{(2\lambda-2)/3} (\mu_N/c)^2 fm^{2\lambda-2}. \tag{1.42}$$

In tables 1.1 and 1.2 below are demonstrated relevant numerical expressions, whereas the second column shows exact values, the third column presents the estimates and the last one

represents the relation between third and first column. It is necessary to note that $B_W(E\lambda)$ and $B_W(M\lambda)$ do not provide exact information, only order-of-magnitude approximations.

$E\lambda$	T($E\lambda$)(s^{-1})	$B_W(E\lambda)$($e^2fm^{2\lambda}$)	$T_W(E\lambda)(^{s-1})$
$E1$	1.587 x $10^{15}E^3B(E1)$	6.446 x $10^{-2}A^{2/3}$	1.023 x $10^{14}E^3A^{2/3}$
$E2$	1.223 x 10^9E$^5B(E2)$	5.940 x $10^{-2}A^{4/3}$	7.265 x $10^7E^5A^{4/3}$
$E3$	5.698 x 10^2E$^7B(E3)$	5.940 x $10^{-2}A^2$	3.385 x $10^1E^7A^2$
$E4$	1.694 x 10^{-4}E$^9B(E4)$	6.285 x $10^{-2}A^{8/3}$	1.065 x $10^{-5}E^9A^{8/3}$
$E5$	3.451 x 10^{-11}E$^{11}B(E5)$	6.928 x $10^{-2}A^{10/3}$	2.391 x $10^{-12}E^{11}A^{10/3}$

Table 1.1: $E\lambda$ denotes the type and order of the transition, $T(E\lambda)$ represent transition probabilities, $B_W(E\lambda)$ are Weisskopf single particle estimates and $T_W(E\lambda)$ are transition probabilities per unit time. The energies E are expressed in MeV and the reduced transition probabilities $B(E\lambda)$ are in $e^2fm^{2\lambda}$. Table taken from [25].

$M\lambda$	$T(E\lambda)$(s^{-1})	$B_W(M\lambda)$((μ_N/c)$^2fm^{2\lambda-2}$)	$T_W(M\lambda)(s^{-1})$
$M1$	1.779 x $10^{13}E^3B(M1)$	1.790	3.184 x $10^{13}E^3$
$M2$	1.371 x $10^7E^5B(M2)$	$1.650A2/3$	2.262 x $10^7E^5A^{2/3}$
$M3$	6.387 x $10^0E^7B(M3)$	$1.650A4/3$	1.054 x $10^1E^7A^{4/3}$
$M4$	1.899 x $10^{-6}E^9B(M4)$	$1.746A2$	3.316 x $10^{-6}E^9A^2$
$M5$	3.868 x $10^{-13}E^{11}B(M5)$	$1.924A8/3$	7.442 x $10^{-13}E^{11}A^{8/3}$

Table 1.2: $M\lambda$ denotes the type and order of the transition, $T(E\lambda)$ represent transition probabilities, $B_W(M\lambda)$ are Weisskopf single particle estimates and $T_W(M\lambda)$ are transition probabilities per unit time. The energies E are expressed in MeV and the reduced transition probabilities $B(M\lambda)$ are in (μ_N/c)$^2fm^{2\lambda-2}$. Table taken from [25].

1.2.2.2 Internal conversion

The alternative to de-excitation via γ-ray emission is internal conversion. This process has higher probability with increasing order of multipole, and decreasing energy of γ-ray transition, and is more probable in heavier nuclei. During internal conversion, the nucleus is transferring energy to an electron, which resides usually on inner shells of the atomic orbit (K, L). The internal conversion is unique in a sense that no real photon is emitted, therefore it is not an internal photon effect. The energy is transported via virtual photons which are mediating the Coulomb force. The reason why electrons on K shell are usually emitted is because they have a non-zero probability of entering the nuclear interior, as shown in Fig.

1.10 [29]. The electron emitted in this way is called conversion electron. Compared to the spectrum from β decay, electrons from internal conversion form a discrete spectrum, as shown in Fig. 1.11.

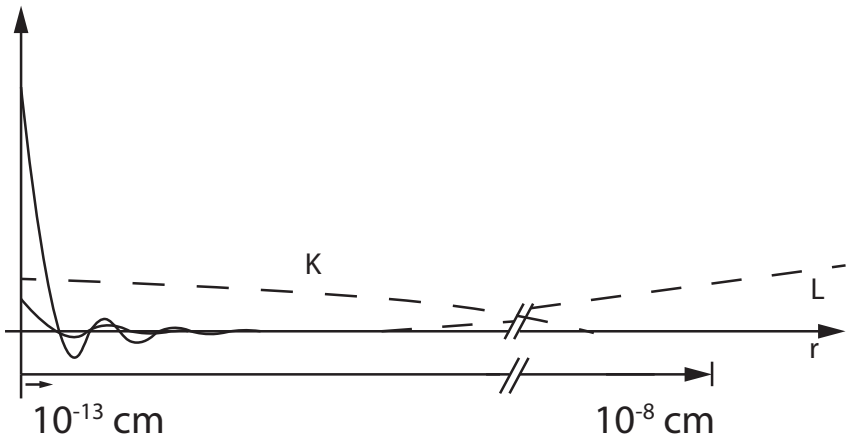

Figure 1.10: Scheme of different length scales associated with the nuclear (full lines at 10^{-13} cm scale) and electronic (dashed lines on a 10^{-8} cm scale) wave functions. Only the K (or s-wave) electrons have wave functions with non-vanishing amplitudes at the origin and will cause electron conversion to occur mainly via K-electron emission. [29].

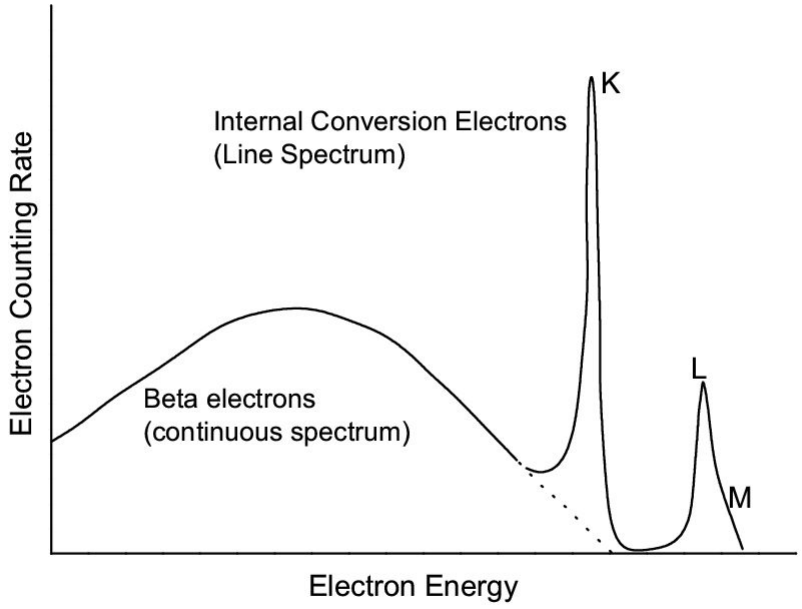

Figure 1.11: Example of spectrum with conversion electrons. Figure taken from [32].

The energy of emitted electron can be calculated from

$$T_e = \Delta E - B_e \tag{1.43}$$

where ΔE represents the energy of nuclear transition and B_e is the binding energy of electron. Since the nucleus can de-excite either via internal conversion or γ-ray emission, the internal conversion coefficient is established and it is defined as:

$$\alpha = \frac{\lambda_{IC}}{\lambda_\gamma} \tag{1.44}$$

where λ_{IC} represents number of conversion electrons from IC and λ_γ represents number of γ-ray transitions. The total decay probability is then defined as:

$$\lambda_t = \lambda_\gamma + \lambda_e. \tag{1.45}$$

Since the binding energy of electrons from each atomic shell is different, the kinetic energy of conversion electron will be different for electrons that originate from K shell, L shell etc. Therefore we are able to distinguish between α_K, α_L, α_M etc. The total internal conversion coefficient can be calculated as:

$$\alpha_{IC} = \alpha_K + \alpha_L + \alpha_M + ... \tag{1.46}$$

By knowing the internal conversion coefficient, it is possible to determine the multipolarity of the transition by comparing our measured coefficient with theoretical value, which can be obtained from dedicated code BrIcc [33].

The emission of the conversion electron will leave a vacancy in one of the lower atomic shells. Rapidly after, this vacancy is filled with an electron originating from higher shells. During this process, one or more characteristic X rays can be emitted. X rays are the same electromagnetic radiation as γ rays, but they originate from atomic shell and their energy is equal to the difference between the initial and final state of the electron that filled the vacancy. For example, if the electron originated from the L shell and filled a vacancy in the K shell, then the K_α X-ray will be emitted. In the same manner, if the vacancy in K shell will be filled with an electron from M shell, then the K_β X-ray will be emitted. This will create a vacancy in higher shells, and therefore L- or M- X-rays will be emitted. Since energy

	Electron binding energy in eV						
Element	K	L1	L2	L3	M1	M2	M3
Re	71676	12527	11959	10535	2932	2682	2367
Os	73871	12968	12385	10871	3049	2792	2457
Ir	76111	13419	12824	11215	3174	2909	2551
Pt	78395	13880	13272	11564	3296	3027	2645
Au	80725	14353	13734	11919	3425	3148	2743
Hg	83102	14839	14209	12284	3562	3279	2847

Table 1.3: Electron binding energies [34] in eV displayed for several elements.

differences between the atomic shells are different for each element, the emitted X-rays are called characteristic. The Table 1.3 shows binding energies of electrons for several elements. A competitive process to X-ray emission is the Auger effect, which is similar to the internal conversion. The difference is that during the Auger effect, the emitted electron, called Auger electron, recieves energy from the excitation energy of the atom. When an electron from higher shells fills the vacancy in lower shell, instead of emission of characteristic X-rays, the released energy is transfered to another electron in higher shells, which is then emitted. This leads to formation of multiple vacancies in the atomic shell. The probability that X-ray emission will take place instead of Auger effect is called fluorescence yield. Lastly, there exists also special case of Auger effect, called Coster-Kronig transition. In this case, the vacancy is filled with an electron from a higher subshell of the same shell. If the energy is then transferred to an electron from the same shell, this emitted electron is called Coster-Kronig electron. The complete process for Auger electrons is shown in Fig. 1.12.

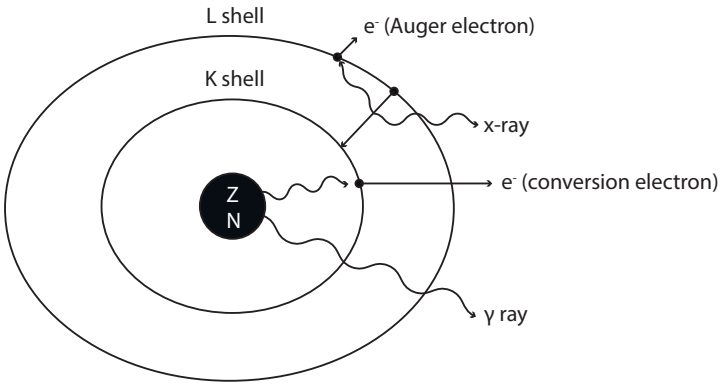

Figure 1.12: Scheme of internal conversion along with Auger electron emission.

1.2.3 Nuclear isomers

Isomers are nuclei in excited states which have delayed decay compared to prompt electromagnetic emission. The minimum half-life of isomers is not exactly defined, therefore, the main condition is usually the measurability of half-life. The range of isomeric half-lives is enormous because they vary from ≈ 1 ns to years. An example of long lived isomer is the 16^+ excited state at 2446.09(8) keV in ^{178}Hf, which has half-life of 31(1) years [35]. The disintegration of an isomer can occur via α or β decay, proton emission, spontaneous fission or via γ-ray emission. There are three known types of nuclear isomers as illustrated in Fig. 1.13.

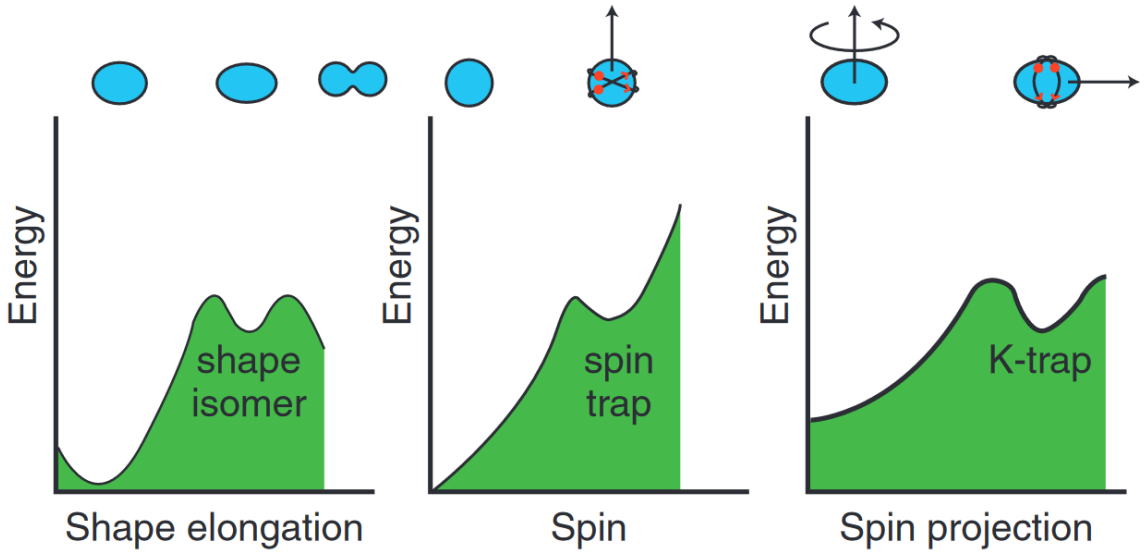

Figure 1.13: Illustration of excitation energy as a function of different nuclear variables. Additional energy minima cause different kinds of isomers. Figure taken from [36].

Shape isomers

These isomers have secondary energy minimum related to the shape of the nucleus. They have shorter half-lives compared to the ground state decay due smaller energy barriers. Shape isomers usually do not de-excite to the ground state due to different deformation. They are often found in heavy nuclei, for example in Am isotopes [37].

Spin isomers

In these isomers, the emission of γ rays is hindered by a large change in nuclear spin. Therefore, γ rays will have a high multipole character. Spin isomers are generally located at

low energy states, which slows down the decay. An example of spin isomer is the 9^- excited state at 77.2(12) keV in ^{180}Ta. The ground state in this isotope has spin and parity of 1^+, therefore, the multipolarity of a γ transition connecting this excited state and ground state is $M8$. The estimated half-life of this isomer is $\approx 10^{15}$ years [38].

K-isomers

K-isomers (also known as the "K-trap" isomer) are similar to the spin isomers, but they they are focused on the orientation of the spin vector, not on its magnitude. The projection of the total nuclear spin along the symmetry axis of the nucleus is represented by the Nilsson number K. In K-traps, the de-excitation is hindered via large difference in K. They are usually found in axially symmetric, deformed nuclei. The selection rule for K-traps is:

$$\Delta K \leq \lambda. \tag{1.47}$$

However, there are cases, where this rule is violated due to symmetry-breaking process. In such cases the "K-forbidden" transitions are hindered, instead of forbidden [39]. An example is the 8^- excited state at 1141.729,keV in ^{180}Hf [40]. It has a $K = 8$ and half-life of 5.47 h. The γ transition with the highest intensity depopulating this excited state is 57.547 keV γ ray. It populates the 8^+ excited state at 1084.183 keV with $K = 0$, which violates the selection rule.

Seniority isomers

In 1943, Giulio Racah introduced a new quantum number called seniority ν [41]. It was defined as the number of unpaired particles coupled to the angular momentum $J = 0$. In general, low-seniority states occur at low energy. For example, the seniority of the ground state in even-even semi-magic nuclei is $\nu \approx 0$ and low energy yrast states with angular momenta J = 2,4,6... is $\nu \approx 2$. A seniority isomer is expected to occur when the energy difference in the $(2j$ - 1) $\rightarrow (2j$ - 3) transition is small enough to produce a long-lived state that decays via $E2$ gamma-ray emission or beta emission [42]. Smaller energy differences are usually found in two states with the same seniority, while two states with different seniority have typical splitting about 1 MeV. An example of seniority isomers is shown in Fig. 1.14. On the left side are shown excited states with $\nu \approx 2$, while on the right side are also excited states with

$\nu = 4$. Numbers between states denote calculated $B(E2)$ values in $B(E2;\ 2_1^+ \rightarrow 0_1^+)$ units of the two-particle system with assumed interaction conserving seniority. Values between levels with same $\nu \approx 2$ seniority are significantly smaller, indicating isomeric states.

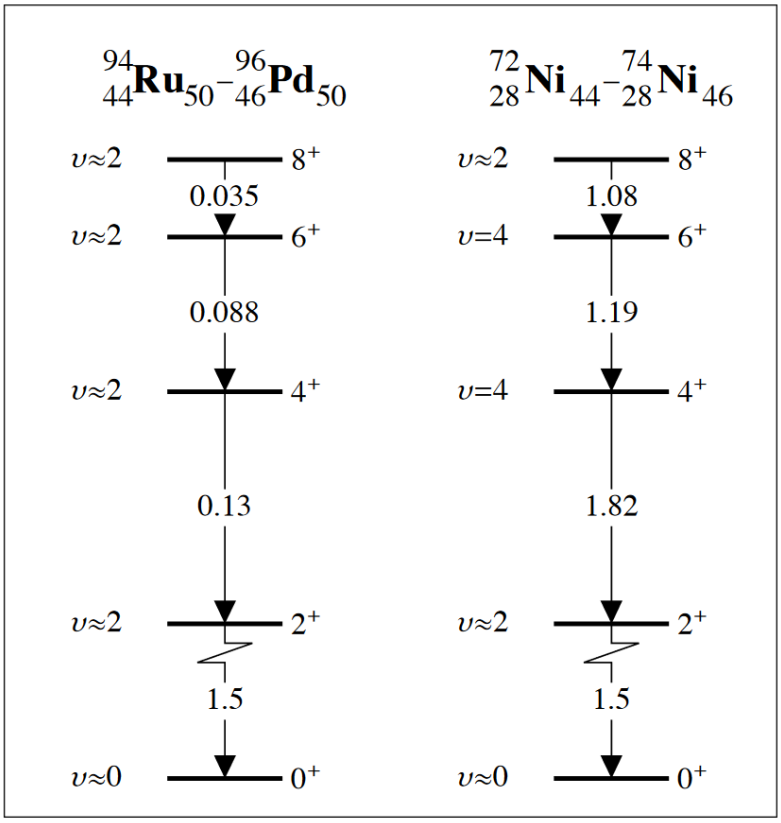

Figure 1.14: $E2$ transitions between yrast states of (left) N = 50 isotones and (right) Z = 28 isotopes. Calculated $B(E2)$ values are shown between the levels. Figure taken from [43].

Chapter 2

Experimental Techniques

2.1 The Heavy ion fusion-evaporation reactions

In the experiments S17 and JR115, heavy-ion fusion-evaporation reactions were used. In this reaction a compound nucleus is created ($\approx 10^{-22}$ s after the projectile hits the target). The created compound nucleus is highly excited and has a very high spin. It will start its de-excitation process almost immediately. The quickest way to lose energy is to emit nucleons, so in $\approx 10^{-19}$ s particle emission starts. This continues until it is not favourable anymore. The next process is the γ-ray emission, which is divided in two parts, statistical and discrete γ rays. Statistical γ rays will carry away energy until they hit the yrast line, which is a state of the nucleus with minimum energy for the particular angular momentum. Up to this point, the nucleus has still high spin, since particle emission and statistical γ rays, change the spin only slightly. Now starts the emission of discrete γ rays which primarily carry away angular momentum. The whole process of γ-ray emission ends $\approx 10^{-10}$ s after the creation of compound nucleus, which means that these γ rays can only be registered at the target position. The scheme of this process is shown in Fig. 2.1.

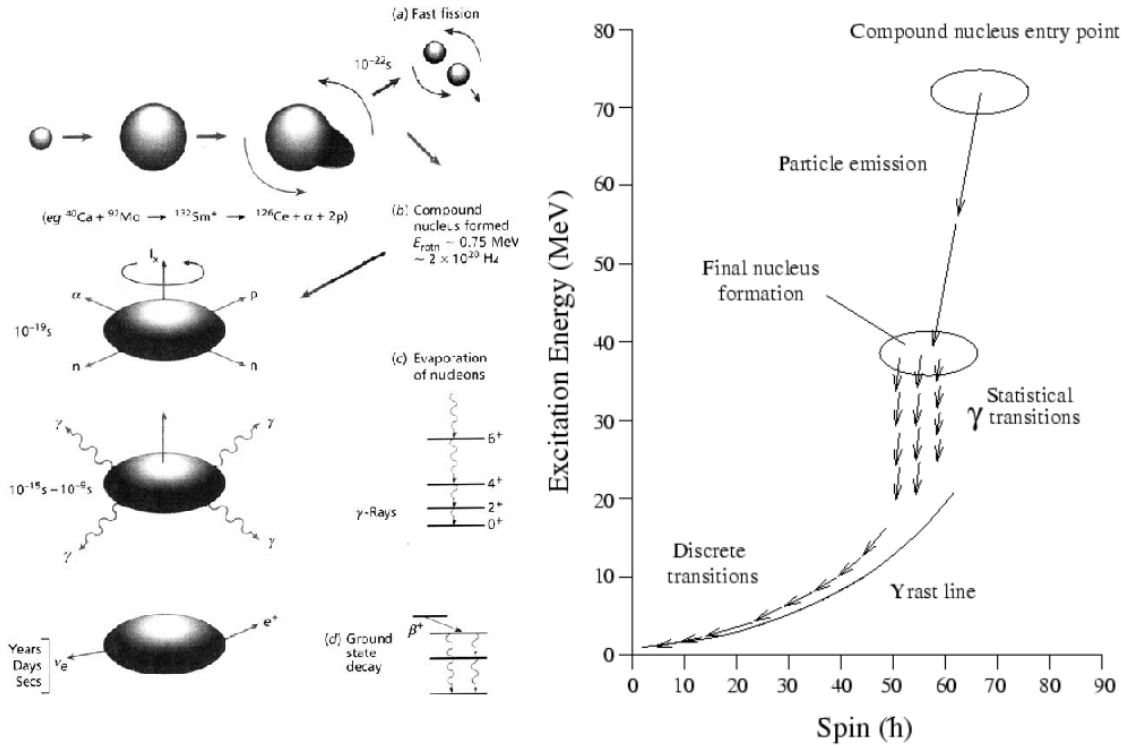

Figure 2.1: Schematic representation of the fusion-evaporation process (left) [44] along with de-excitation of compound nucleus (right)[45]

2.2 Experimental setup

For acceleration of heavy ions at JYFL, the K-130 isochronous cyclotron accelerator is used. K-130 operates on a principle that the magnetic field inside is increasing with the radius of the ions, which creates constant frequency of the ions. The ions are produced by and injected to the K-130 cyclotron from the electron cyclotron resonance (ECR) ion sources. Typical energies of ions entering the accelerator are tens of keVs. The maximum energy that can be reached with this accelerator is given by the formula:

$$E = 130\frac{Q^2}{A}, \tag{1.1}$$

where Q is the charge and A is the atomic mass number of the accelerated particle. The mass resolving power of the K130 cyclotron is around 0.02% [46].

2.2.1 The JUROGAM II array

The main goal of the JUROGAM II array is to measure prompt γ rays. The JUROGAM II array is composed of two types of high-purity germanium (HPGe) detectors: tapered single-crystal Phase I detectors [47] and four-fold segmented Clover detectors [48]. They are placed around the target chamber in a sphere-like arrangement in four rings, with 15 Phase I detectors in first two rings and 24 Clover detectors in remaining two rings. The angles θ relative to the beam direction are shown in Table 2.1.

Ring no.	Midpoint angle θ	Number of detectors in the ring	Detector geometry
1	157.6°	5	Phase I
2	133.57°	10	Phase I
3	104.5°	12	Clover
4	75.5°	12	Clover

Table 2.1: Position of detectors in the Jurogam II array. The 2^{nd} column shows angles θ relative to the beam direction.

The photopeak efficiency of the JUROGAM II array is 5.5% at 1332 keV [49]. The signals from the detectors are directly digitized with Lyrtech VHS-ADC cards and the determination of detected γ-ray energies is done by a moving window deconvolution (MWD) algorithm [50] that is part of the analog-to-digital converters (ADC) cards with field-programmable gate-array (FPGA).

2.2.1.1 Anti-Compton suppression shield

Detectors of the JUROGAM II array are equipped with the Bismuth Germanate (BGO) anti-compton shielding for background suppression, as shown in Fig. 2.2. Each BGO shield is composed of backcatcher and side shield elements. The backcatcher prevents forward Compton-scattered events from escaping through the large angular section located behind the Clover. With the help of the backcatcher it is possible to improve the maximum peak-to-total ratio up to 95% for 1.33 MeV according to calculations [51], in case the thickness of the backcatcher is $\approx$ 2.5 cm of BGO. The side shields are split into two pieces of BGO with thickness of the rear section $\approx$ 2 cm and $\approx$ 1 cm for the front section.

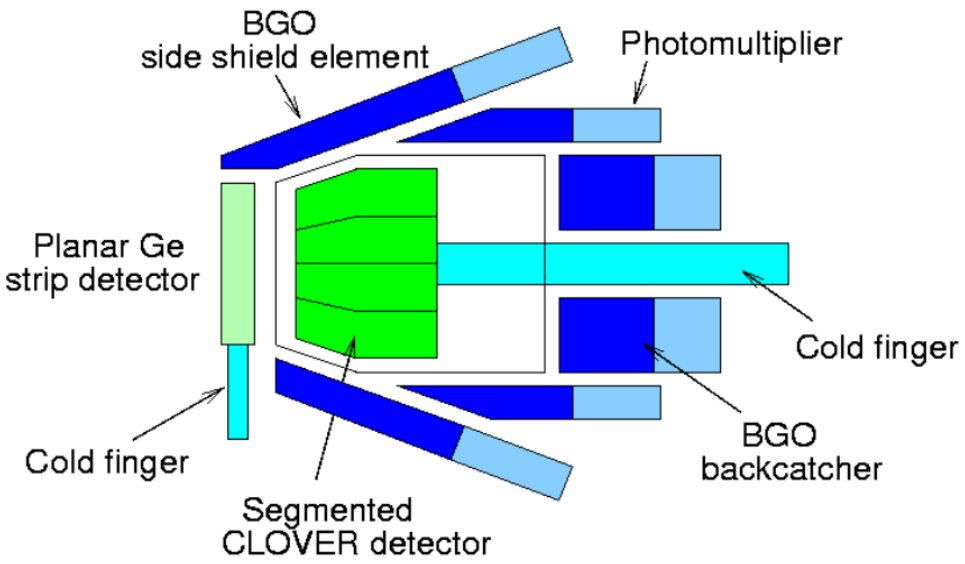

Figure 2.2: Side view of Clover detector in focal plane along with its BGO suppression shield. Figure taken from [8].

2.2.1.2 Add-back technique

In germanium detectors used in the present work, the dominant type of interaction of γ radiation with energy in a range of 0.2 - 7 MeV with matter is the Compton scattering. This means, that a probability of the γ ray hitting one germanium crystal, depositing a part of its energy, and then scattering to another, neighbouring crystal, leaving the rest of its energy there is quite high. For high-energy γ rays, the number of scatters can be even higher. These partial energy depositions within one detector are time correlated, and can therefore be summed together to recover a full, original, γ-ray energy. This summation of events is known as the add-back technique. It is commonly used in a case of clover-type HPGe detectors, such as those in the JUROGAM II array, where a 200 ns time window is usually applied to sum events. The use of the add-back technique will result in a better photopeak efficiency, and improved peak-to-total ratio. However, a peak's FWHM will get slightly worse [52].

2.2.1.3 Doppler effect

In case of a thin target, recoils (fusion-evaporation reaction products) will retain a significant part of the projectile energy. This means that recoils, which are emitting γ rays, have enough velocity (several % of speed of light) for Doppler effect to be considered. If the source of electromagnetic radiation (γ rays) is the recoiling nucleus, then the HPGe detectors

in each Ring of the JUROGAM II array are the observer. The Doppler effect will shift the γ-ray energy (E_γ) with varying wavelength, which is tied to the recoil velocity v according to

$$E_\gamma = E_0(1 + \frac{v}{c}\cos(\theta)), \tag{2.1}$$

where E_0 represents the initial energy of γ quanta, c is the speed of light and θ is the angle between the detector and the trajectory of ion beam. [53].

2.2.2 The SAGE spectrometer

The Silicon And GErmanium (SAGE) spectrometer is a highly segmented silicon detector that is usually used in combination with the JUROGAM II array for improvement of in-beam measurements. As the name already suggests, the Silicon And GErmanium (SAGE) spectrometer is primarily intended for simultaneous measurements of prompt γ rays and electrons. This technique is mainly used to obtain experimental internal conversion coefficients. In experiments, it is coupled with the JUROGAM II array and the RITU separator as graphically shown in Fig. 2.3, thus providing a powerful spectrometer enhancing the sensitivity of in-beam spectroscopic studies. It also brings one limitation to experimental setup, that 5 Phase I detectors (Ring 1) have to be removed from the JUROGAM II array. When SAGE is used, number of Phase I Compton detectors on the JUROGAM II is decreased to 10 (from 15 when SAGE is not used). Even though the detector is segmented into 90 parts, its total active area is 96 %. Each pixel of this silicon detector is connected to a high-gain charge sensitive preamplifier. Because this detector is capable of detecting not only electrons, but also other charged particles (like α particles, protons etc.), its position is 95.5 cm upstream of the target. The scheme is shown in Fig. 2.4.

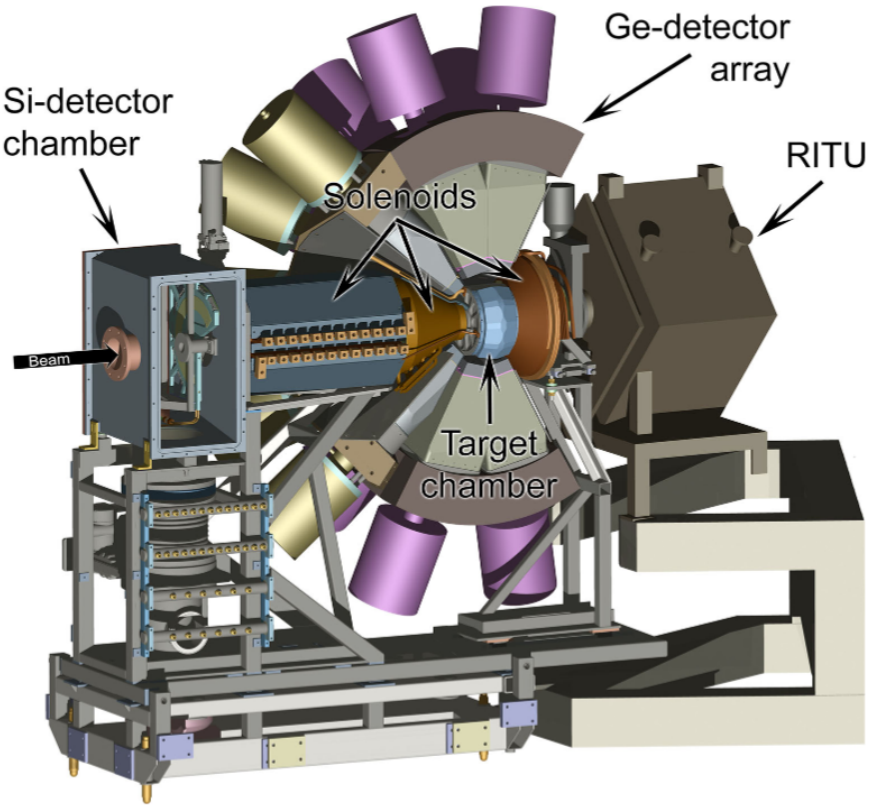

Figure 2.3: The scheme of SAGE connected to JUROGAM and combined with the JUROGAM II array and the RITU separator. Figure taken from [54].

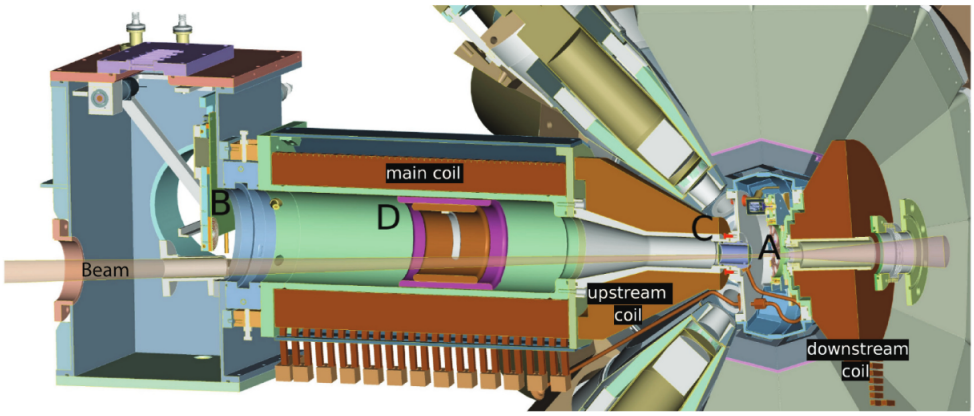

Figure 2.4: Detailed scheme of SAGE setup. "A" represents target position, "B" is the silicon detector, "C" is the carbon foil, used to separate the high vacuum of the whole system and gas inside of RITU, and "D" which represent the high-voltage barrier, used to reduce delta-electron background. Figure taken from [55].

2.2.3 The RITU gas-filled recoil separator

For the study of heavy elements, the Recoil Ion Transport Unit (RITU) was constructed. It is used to separate products from fusion-evaporation reactions recoiling from the target,

and unwanted particles. Electric and/or magnetic fields are used for the separation. The inside of the separator is filled with diluted He gas to ensure better transmission efficiency of the recoiling products. The He gas is separated from the high vacuum in the rest of the system by a set of 50 μg/cm^2 carbon foils. As a consequence of ions hitting gas atoms, the charge state distribution of these drifting ions will narrow and the average charge state (q_{avg}) of ions will be transported to the focal plane resulting in minimal image size.

The scheme of the RITU separator can be is shown in Fig. 2.5 and it is composed of three magnetic quadrupoles and one magnetic dipole. The magnetic dipole is situated right behind the first quadrupole magnet. The role of the first quadrupole is to improve matching of the recoils to the acceptance of the dipole magnet, which deflects the ions and separates them according to their mass. The last two quadrupoles then focus the beam to the focal plane. When compared to vacuum separators, the RITU separator has lower mass-resolving power, but on the other hand its transmission is considerably better. Usually the RITU separator is operated at pressure of 0.6 mbar with He as a filling gas.

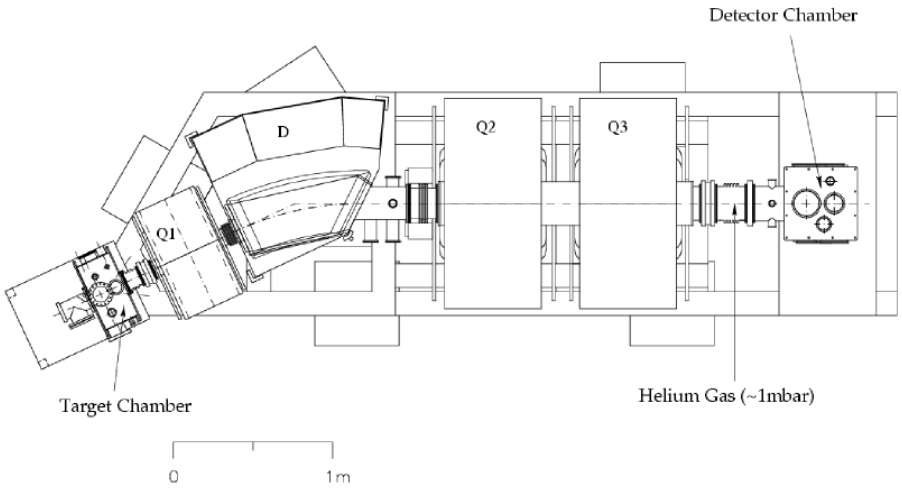

Figure 2.5: The scheme of the RITU gas-filled recoil separator viewed from the top. Figure taken from [7].

The ions are bend according to Lorentz force as

$$F = ma = \frac{mv_{\perp}^2}{\rho} = Q|(\overrightarrow{v}\, x\, \overrightarrow{B})| = eq_{avq}v_{\perp}B$$
$$\frac{mv_{\perp}}{eq_{avq}} = B\rho \tag{2.2}$$

where m represents the mass of the ion, ρ is radius of the curvature, a is the centrifugal acceleration, $v_{\perp}$ is the velocity perpendicular to the magnetic field, Q is the charge and B

is the magnetic field. In this case the magnetic rigidity is defined by the product of $B\rho$ and the RITU separator is capable of operating with magnetic rigidities as high as 2.2 Tm. The magnetic rigidity can be written as:

$$B\rho = 0.0227\frac{A}{Z^{\frac{1}{3}}}. \tag{2.3}$$

For recoils produced in ion induced fusion-evaporation reactions the transmission efficiency of the RITU separator depends heavily on type of experiment and ranges from 7% to 90% [56].

2.2.4 The GREAT focal plane spectrometer

At the focal plane of the RITU separator is the detection system: the GREAT (Gamma Recoil Electron Alpha Tagging) spectrometer. It consists of multi-wired proportional counter (MWPC), double-sided silicon strip detectors (DSSD), four Clover HPGe detectors and PIN-detectors. All of these detectors are used to measure the decay properties of isotopes transported by the RITU separator and to correlate the measured particles (as α particles, conversion electrons, γ and X-rays) with recoils [8].

2.2.4.1 Multi-wire proportional counter

The MWPC detector is used to distinguish recoils from their decays and it is situated right behind the RITU separator. The MWPC detector is composed of horizontal and vertical wiring used to achieve position sensitivity of the detector. These electrodes are placed inside of the gas filled chamber (usually isobutane), with thin Mylar windows, which serve the purpose of separating the isobutane inside the MWPC detector and He gas inside the RITU separator. The second reason for using Mylar foils is that the transmission of ions through them is higher than through metallic windows. The MWPC detector is also called the gas counter, because it is capable of registering the energy losses dE of particles, but it can not discern the particles. A time-to-amplitude converter (TAC) is giving us the position of recoil passage by using the time difference of signals coming from the fast anode (metallized foil) and slow wire planes read through delay lines.

2.2.4.2 Double-sided silicon strip detector

The most important detector at the focal plane is the double-sided silicon strip detector (DSSD), which is situated 240 mm downstream from the MWPC detector. The DSSD is divided into two parts, each with the implantation area of 60 mm^2 x 40 mm^2 with the strip pitch equal to 1 mm. Space resolution of one DSSD is 2400 pixels, therefore both of them form the space resolution of 4800 pixels. The thickness of the DSSD used in this work is 300 μm. The great advantage of the DSSD is that it gives energy, time and position information. By looking at the signal from MWPC and the DSSD, it is possible to easily distinguish whether the signal in the DSSD belongs to a recoil or whether it is the product of radioactive decay. This will be discussed more in detail later in the text, see chapter 2.4.2. Another advantage of the DSSD is that it can register the subsequent α decays of recoils in horizontal strips and internal conversion electrons in vertical strips.

2.2.4.3 PIN diodes

Another detectors at focal plane are 28 PIN diodes which form a box detector upstream from the DSSD. They are used to detect protons, α particles and conversion electrons, that escaped from the DSSD detector. Each PIN diode has dimensions of 28 mm x 28 mm and a thickness of 500 μm. The geometrical efficiency of PIN diodes is 30 %.

2.2.4.4 The focal plane Germanium detectors

Two types of germanium detectors are located in the focal plane, the planar strip detector and clover-type HPGe detectors. The former one is located 10 mm behind the DSSD detector in the vacuum chamber of the GREAT spectrometer. It is separated by a 5 mm thin Beryllium window. This detector has an active area of 120 mm x 60 mm and it is 15 mm thick. On both faces is a 5 mm strip pitch which provides position information that can be correlated with the remaining detectors of the GREAT spectrometer. The planar detector is used to detect X-rays, low energy γ rays and high energy β particles. The simulated efficiency of this detector is shown in Fig. 2.6.

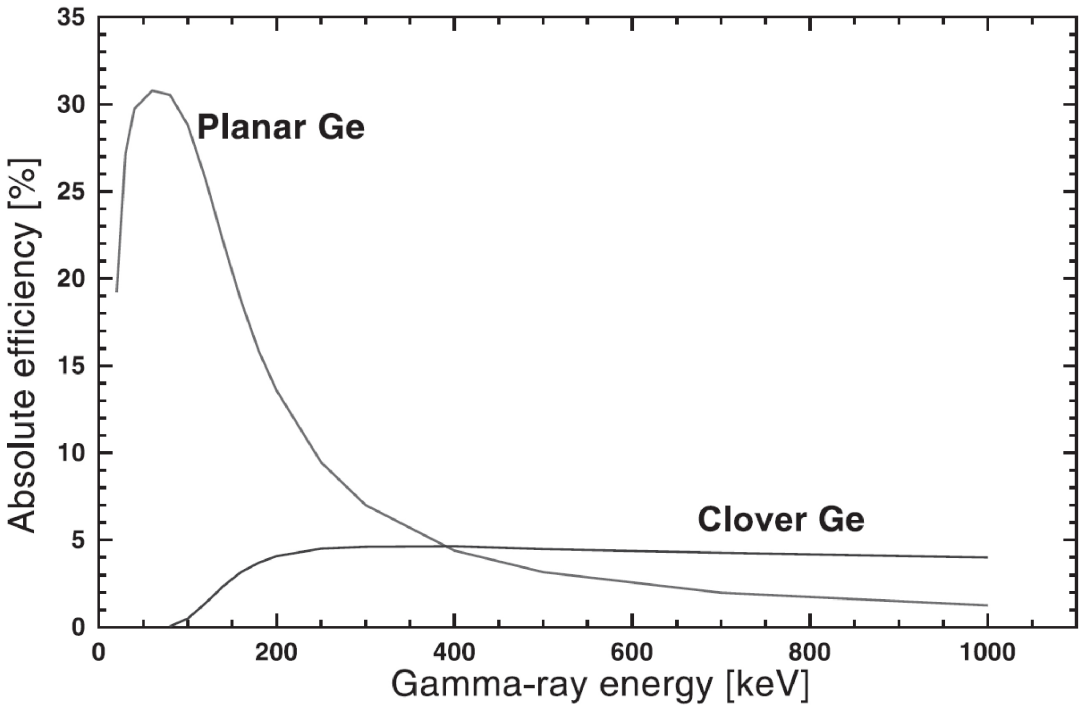

Figure 2.6: Efficiency of γ rays for focal plane Germanium detectors simulated in GEANT4. Figure adopted from [8]

For the detection of high energy γ rays there are Clover Germanium detectors placed on top of the vacuum chamber as well as on the sides or behind the implantation detector. Each Clover detector has 70 mm diameter, is 105 mm long and is segmented into four crystals. Morover, each Clover detector is surrounded by a suppression shield with bismuth germanate crystal, which is 185 mm long. This BGO shielding suppress the Compton scattering and therefore improve the peak-to-total ratio. The setup of detectors at the focal plane can be seen below in Fig. 2.7.

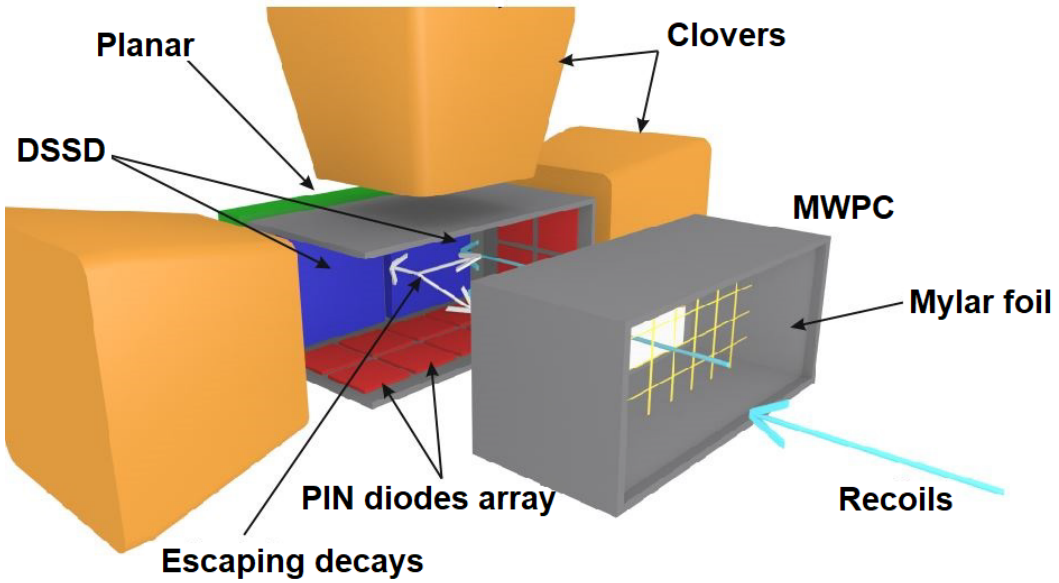

Figure 2.7: The scheme of the focal plane from top and bottom view. Figure taken from [57].

2.2.5 Energy calibration

The energy calibrations for focal-plane HPGe Clover detectors and planar Ge detector was done by using a ^{152}Eu - ^{133}Ba (gamma) calibration source. In case of the DSSD, a standard energy calibration with triple alpha source (^{241}Am, ^{239}Pu and ^{244}Cm) was used for an external calibration. However, during an experiment the recoils are implanted into the DSSD detector, thus an additional internal calibration was performed, using peaks corresponding to known characteristic α decays obtained from the measured data (experiment S17). The extraction of the peak positions in calibration spectra together with their errors was achieved by fitting the peaks with the Gaussian function in the program ROOT [58]. The function used to convert channels to the energy was a linear function for the DSSD detector and a quadratic function for the two germanium detectors. FWHM of focal plane HPGe Clover detectors was determined to be 2.79(34) keV at the 356 keV γ ray of ^{133}Ba nuclei, 3.08(53) keV at the 963 keV γ ray of ^{152}Eu nuclei for the planar Ge detector and 23.8(24) keV at the 5848 keV α-decay energy of the ^{179}Au nuclei for the DSSD detector.

Results of energy calibrations for detectors are presented in Figs. 2.8, 2.9, 2.10 for focal plane HPGe Clover detector, planar Ge detector and the DSSD, respectively. The PIN diodes were calibrated using the ^{133}Ba electron source. Only approximately one half of the PIN diodes could be calibrated. Their calibration was also difficult to perform due to insufficient number of calibration peaks, which was a result of high energy threshold set in

the experiment. The result of PIN diodes calibration is shown in Fig. 2.11.

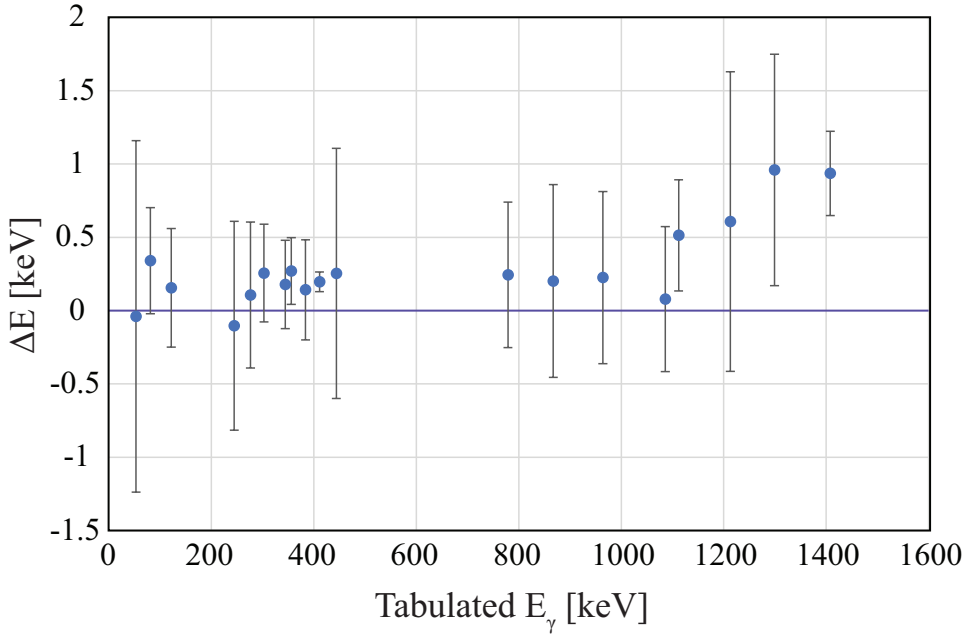

Figure 2.8: Energy differences ΔE for the measured and tabulated [59] transition energies after the calibration of the focal plane HPGe Clover detectors with the ^{133}Ba-^{152}Eu calibration source. In this figure, measured energies from a total focal plane HPGe Clover detectors energy spectrum have been used.

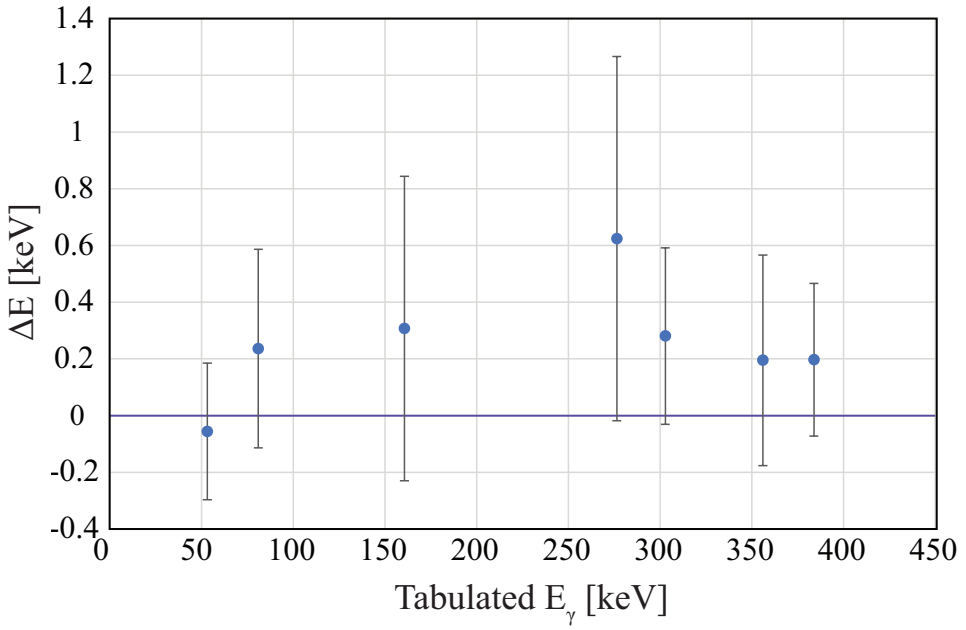

Figure 2.9: Energy differences ΔE for the measured and tabulated [59] transition energies after the calibration of the planar Ge detectors with the ^{133}Ba calibration source. In this figure, measured energies from a total planar Ge detectors energy spectrum have been used.

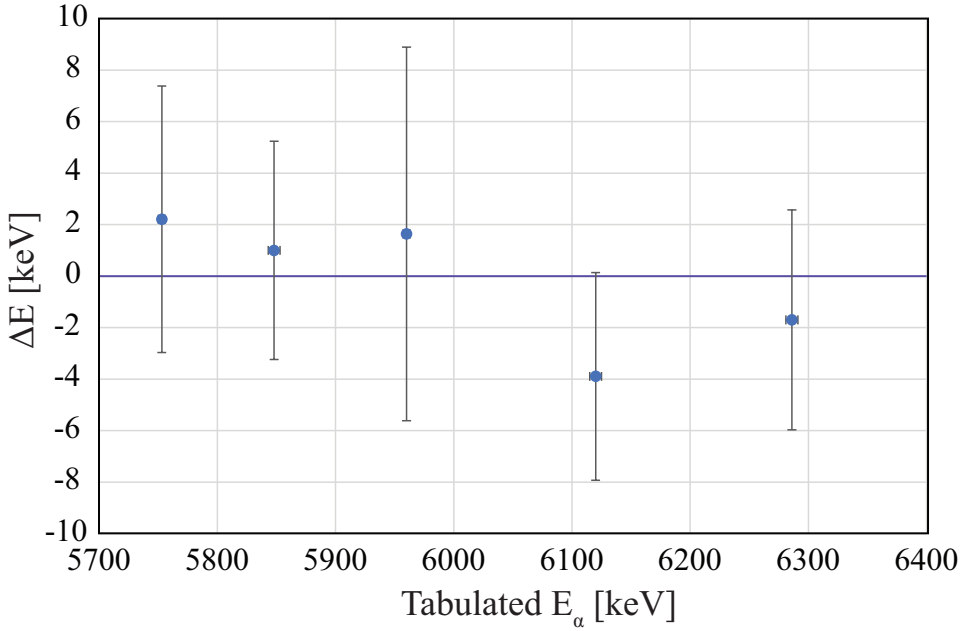

Figure 2.10: Energy differences ΔE for the measured and tabulated [59] transition energies after the calibration of the DSSD detectors with the triple alpha calibration source (^{241}Am, ^{239}Pu and ^{244}Cm). Data plotted for all y-strips of the DSSD together.

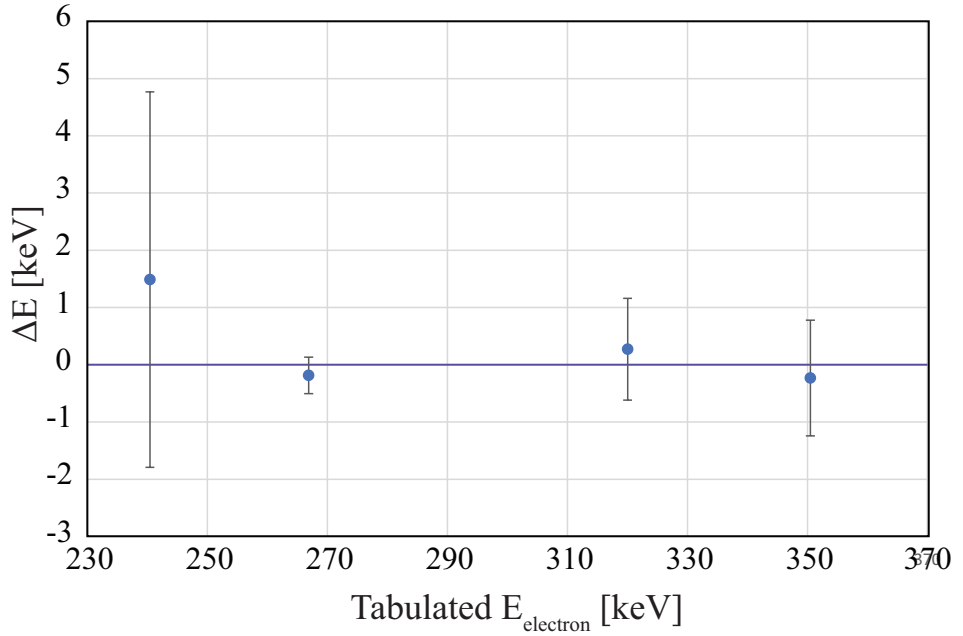

Figure 2.11: Energy differences ΔE for the measured and tabulated [60] transition energies after the calibration of the PIN diodes with the ^{133}Ba electron calibration source. In this figure, measured energies from 8 operational PIN diodes energy spectrum have been used.

The efficiencies of the detectors were taken from [61].

2.3 Total Data Readout System

Standard data acquisition systems (DAQ) collect data in defined time gates. This means that a certain dead-time is formed and in experiments with high count rates it could lead to loss of useful data. The total data readout (TDR) [62] technique works on another principle, which is collecting all of the data separately from all the detectors and assigning them a time stamp (additional to an energy stamp) by DAQ 100 MHz clock, without any trigger condition. Therefore, the TDR can operate with precision of 10 ns. Subsequently, the software reconstructs events and creates necessary trigger and correlation conditions.

The operational scheme of TDR is shown in Fig. 2.12. Shaping amplifiers with constant fraction discriminators (CFDs) are used to convert energy and time stamps from all the detectors. The data then continues to analog-to-digital converter (ADC) cards, which are used to assign time stamps to individual signals. For better synchronization a metronome unit is used. In the Data Buffering, collection, merging and signals from all detectors are arranged according to their time stamp. Afterwards the event builder is used to reconstruct the data with pre-set software trigger and correlation conditions [62].

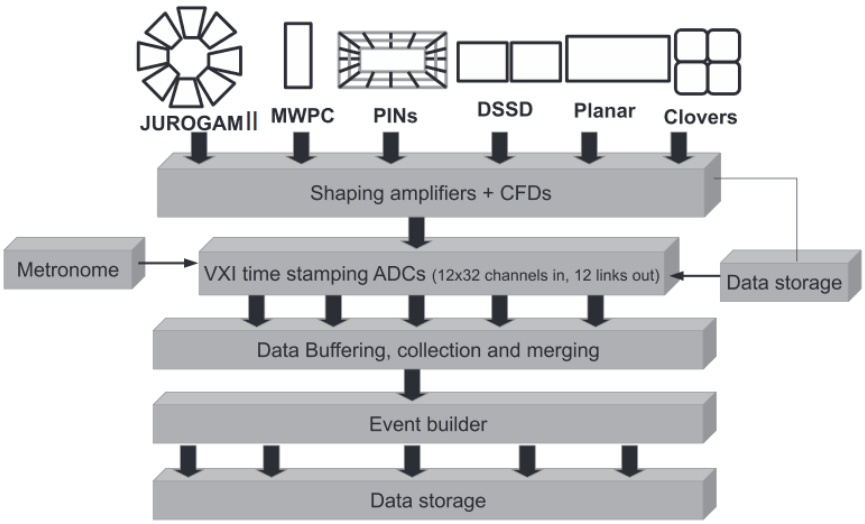

Figure 2.12: A scheme depicting electronics of the GREAT TDR system. Figure taken from [62].

2.4 Data analysis methods

One of the main benefits of the TDR system just discussed, is the possibility of using various tagging techniques in the data analysis. Two of those techniques used in this work, the recoil gating and recoil-decay tagging, are described below.

2.4.1 Recoil gating

Firstly it is necessary to identify the recoils. The MWPC detector plays a very important role in this separation because the decays in the DSSD did not pass through MWPC, therefore they will not produce the signal in this detector. By using signals from MWPC and the DSSD it is possible to create matrix (ToF vs dE/dx see Fig. 2.13), which can be used as a gate to purify the spectra of undesired events. This is so called recoil gating.

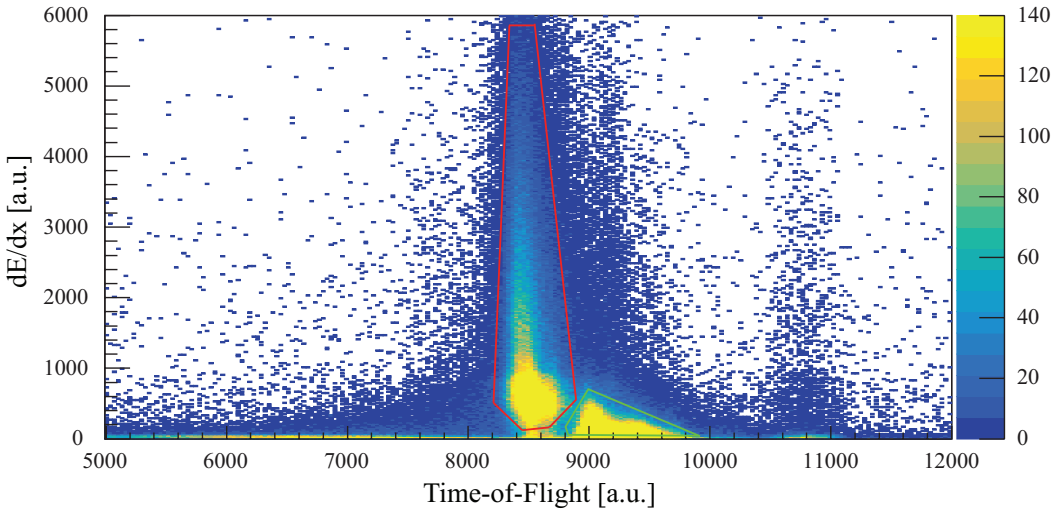

Figure 2.13: The Time-of-Flight between the MWPC and the DSSD vs. energy loss dE/dx measured in MWPC during experiment S17. This matrix was used to select the nuclei of interest - recoils, from the unwanted particles that passed through the MWPC. The red line marks the 2-dimensional gate used for selection of recoils and the green line marks the beam particles.

2.4.2 Recoil Decay Tagging

During in-beam experiments the detectors at the target position register a lot of γ radiation from different sources. The reason is that all reaction products (including *e.g.* undesired reaction channels, fission fragments) are all highly excited. Therefore, they emit γ rays, which are detected along with γ rays emitted during the interaction of projectiles with the

target or walls, thus creating a significant background. To lower the background and to assign the source of these γ rays, the recoil-decay tagging technique (RDT) [9] is used. The first prerequisite is that the desired recoil needs to emit characteristic α particles or protons. When a recoil is implanted into the DSSD, this event will be stored in a "tagger", which is a container storing events for specific pixel with all correlated events from focal and target planes, in defined time window. If the recoil undergoes a decay process (α decay, proton emission), and the characteristic particle is registered within the same pixel as the recoil, these two events are put into tagger as one chain of consecutive events. Later, it is possible to identify the recoil and create a correlated event chain. It is possible that another recoil hits this pixel and therefore causes a miscorrelation. The best use of RDT can be achieved when:

- the recoils are evenly scattered, so that the active area of the DSSD is utilized fully,
- the rate of recoils is small enough, so that the probability of second recoil hitting a pixel with active tagger is negligible,
- the half-life of recoils is long enough, so that the recoils are able to get through the separators and be implanted into the DSSD, but at the same time short enough, so that the decay would happen after they are implanted,
- the daughter nuclei has to decay with different energy than the recoil.

Chapter 3

Experimental results

The main focus of this work is the α-decay spectroscopy and study of the α-decay fine structure in neutron-deficient isotopes ^{179}Hg and ^{177}Au, together with their decay products. In the offline analyses, data from two experiments with code names S17 and JR115 were investigated. Both experiments were performed at the Accelerator laboratory of the University of Jyväskylä (JYFL), Finland. Results of the focal-plane data analyses are presented in this work. Analyses of in-beam data were subject of different studies, namely studies of ^{179}Au [57], and ^{177}Au [63], respectively. The experimental setup used in the S17 experiment consisted of the Jurogam II array, the RITU separator coupled with the GREAT and the SAGE spectrometers. In the experiment JR115, the standard setup consisting of the Jurogam II array in conjunction with the RITU separator and the GREAT spectrometer was used. Data were analysed with the data analysis system GRAIN [64], the data analysis framework ROOT [58] and the fitting program HDTV [65]. Measurable quantities obtained in this work include $e.g.$ E_α, E_γ, $T_{1/2}$, b_i etc.

3.1 Previous studies of ^{179}Hg and ^{175}Pt

Prior to the present study, one characteristic α decay was known for the ^{179}Hg isotope. This α decay was first observed by A. G. Demin [66] with $E_\alpha = 6076(12)$ keV and half-life of 3.5(4) s. Later on, a somewhat different energy and half-life values $E_\alpha = 6270(15)$ keV and $T_{1/2} = 1.09(4)$ s were attributed to the ^{179}Hg α decay by Hansen *et al.* [67, 68]. Moreover, a branching ratio $b_\alpha = 53$ % was estimated. Another study with more or less the same energy $E_\alpha = 6288(5)$ keV was carried out by [69]. Recently, a different branching ratio $b_\alpha = 75(4)$ %

was reported in [70], using correlated α-decay chains. The hindrance factor (*HF*) was determined as 1.4(2) and the decay was attributed as $(7/2^-)$ ground state to $(7/2^-)$ ground state. The ground state configuration of ^{179}Hg was assigned as $(7/2^-)$ [514] and $7/2^-$ [503] orbitals arising from the $f_{7/2}$ and $h_{9/2}$ shells, respectively.

In contrary, the child nucleus ^{175}Pt has four known characteristic α decays. Three of these α-decay branches with energies of 5831(10), 5964(5), 6038(5) keV and branching ratios of 4.7, 55, 4.8 %, respectively, were thoroughly studied in the past [68, 69, 71, 72]. Recently, the fourth α-decay branch with E_α = 5819(4) keV was identified via α-γ coincidences [11]. All of these α decay branches depopulate the ground state in ^{175}Pt. The newly observed α decay populates $(9/2^-)$ excited state at 207.9(5) keV in ^{171}Os. Subsequently, this excited state can de-excite via emission of 207.9(5) keV γ ray which populates the $(5/2^-)$ ground state or via emission of 130.8(4) keV γ ray feeding the $(7/2^-)$ excited state at 76.7(3) keV in ^{171}Os. In Fig. 3.1, the α-decay level scheme of ^{175}Pt deduced in [11] is given. In the same study a $(9/2^-)$ excited state at 130.9(6) keV in ^{175}Pt was observed. This excited state de-excites via emission of 130.9(6) keV γ ray down to the $(7/2^-)$ ground state in ^{175}Pt. The similarity between the 130.8(4) keV and 130.9(6) keV transitions led to the search for the α decay populating the $(9/2^-)$ excited state at 130.9(6) keV in ^{175}Pt which could reveal a decay pattern in the above-described decay chain.

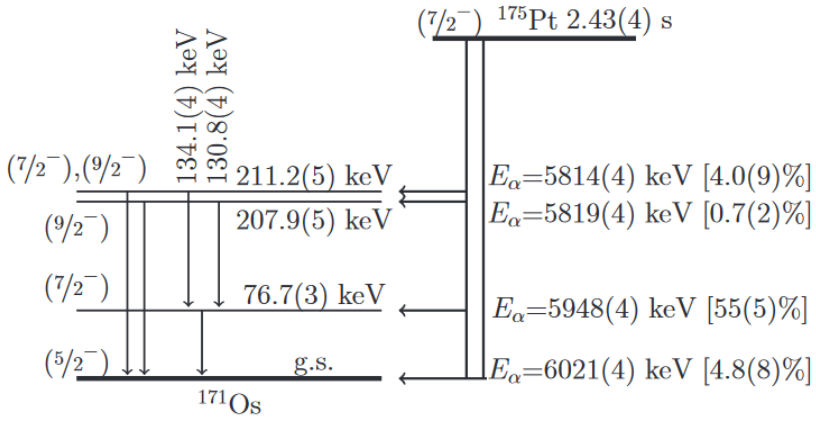

Figure 3.1: The α-decay scheme of ^{175}Pt. Figure was taken from [11].

3.2 Results of the S17 Experiment

Experiment S17 was performed on October 21 - November 4, 2013 at JYFL, Finland. The main goal of the experiment was to study shape coexistence in ^{179}Au. The fusion-evaporation reaction $^{100}_{44}$Ru($^{82}_{36}$Kr, 3n)$^{179}_{80}$Hg was used to produce nuclei of interest. The $^{82}_{36}$Kr^{15+} ion beam, accelerated to an energy of 352 MeV by the K-130 cyclotron, was impinged on the self-supporting $^{100}_{44}$Ru target with a thickness of 350 μg/cm^2. The beam intensity was on average 5 particle nA (pnA). The total α-particle energy spectrum measured with the DSSD detector is shown in Fig. 3.2.

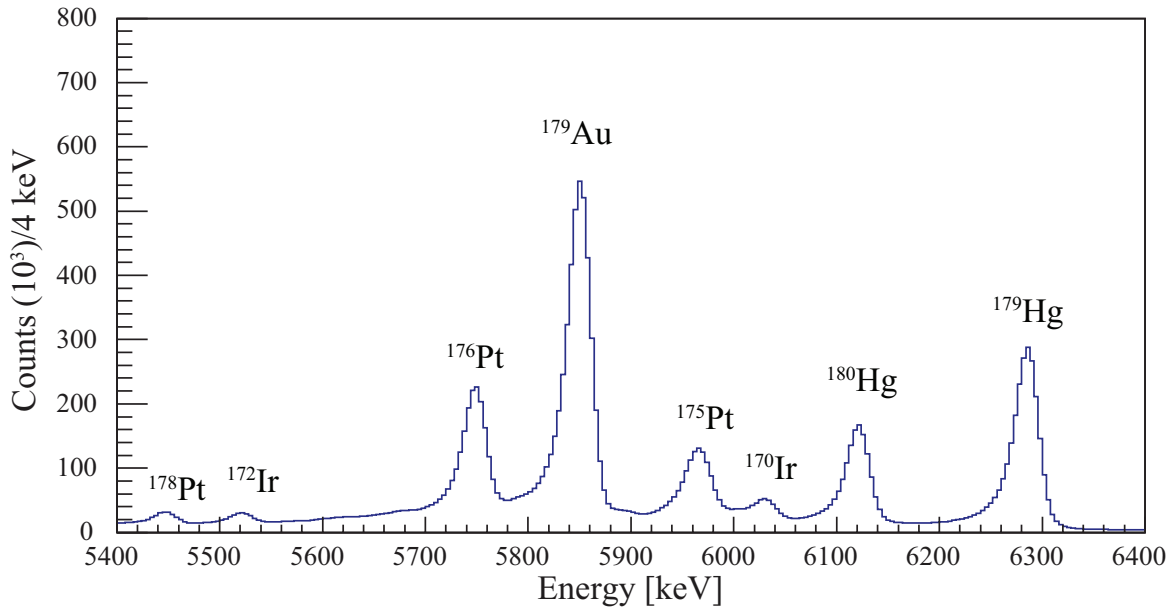

Figure 3.2: Energy spectrum of α particles from the reaction $^{82}_{36}$Ru + $^{100}_{44}$Ru, measured with the DSSD detector and vetoed by the MWPC. Experiment S17.

The GREAT spectrometer at the focal plane of the RITU separator allows us to study the nuclear α decay with a high precision. The first step in the analysis was the investigation of the α-decay chains. For this purpose the ER-α_1-α_2 correlation matrix was constructed. Correlation (search) times $\Delta t(\alpha_1 - \mathrm{ER}) \leq 3$ s between the recoil (ER) and parent alpha (α_1) and $\Delta t(\alpha_2 - \alpha_1) \leq 7$ s between parent alpha (α_1) and child alpha (α_2) were used. The matrix is shown in Fig. 3.3. In this matrix, three α-decay chains were identified as:

- ^{178}Hg [$E_\alpha = 6430(6)$keV] $\rightarrow$ ^{174}Pt [$E_\alpha = 6038(4)$keV],
- ^{180}Hg [$E_\alpha = 6120(5)$keV] $\rightarrow$ ^{176}Pt [$E_\alpha = 5753(3)$keV],

- ^{179}Hg [E_α = 6287(5)keV] $\rightarrow$ ^{175}Pt [E_α = 6034(5), 5970(6), 5836(4)keV].

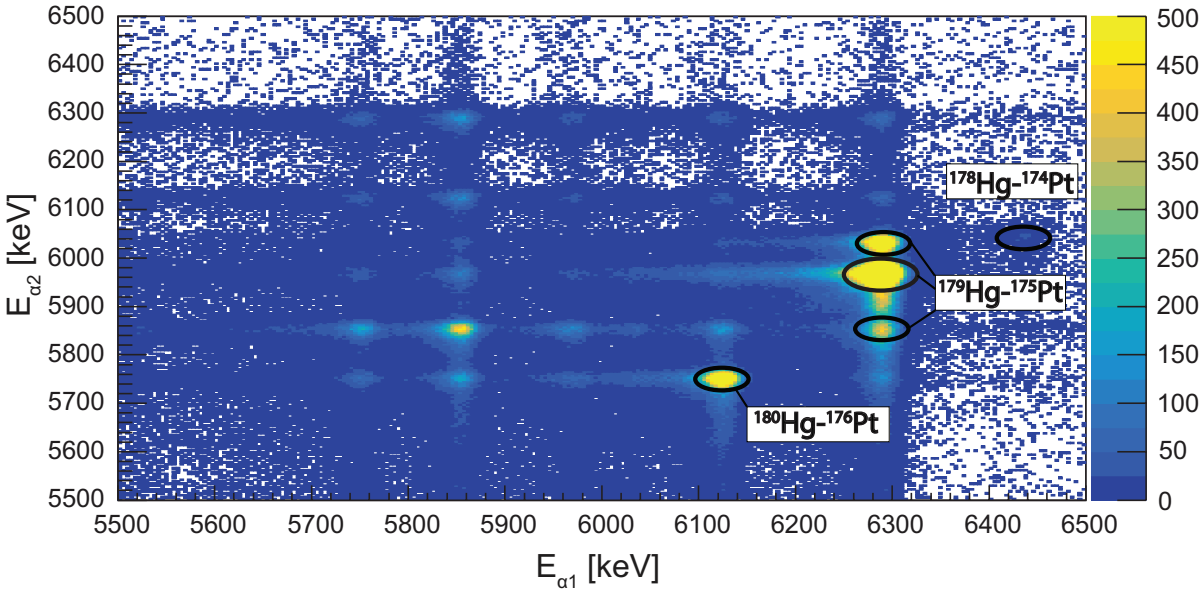

Figure 3.3: The ER-α_1-α_2 matrix of correlated α-decay events, measured with the DSSD detector. A time windows $\Delta t(\alpha_1 - \mathrm{ER}) \leq 3$ s between recoil (ER) and parent alpha (α_1) along with $\Delta(\alpha_2 - \alpha_1) \leq 7$ s between parent alpha (α_1) and child alpha (α_2) were used. True correlations are labelled, whereas the rest are random correlations. Experiment S17.

According to the branching ratios for the ^{175}Pt α decay reported in [69], the (7/2$^-$) g.s. to (5/2$^-$) g.s. α decay with an energy of 6034 keV should have the same intensity as the 5836 keV α decay populating the 211.2 keV energy level in ^{171}Os, as shown in Fig. 3.1. As can be seen in the matrix shown in Fig. 3.3, the 6034 keV α-decay peak is significantly stronger than the 5836 keV α-decay peak. This difference can be explained by a high conversion coefficient for the 76.8 keV $M1$ transition feeding the (5/2$^-$) ground state in ^{171}Os, see Fig. 3.1. In ref. [11], the conversion coefficient α_K(76.8 keV) = 11.6(9) is given. This means that a significant number of conversion and Auger electrons are produced in the 5970 keV α decay feeding the 76.8 keV excited state in ^{171}Os. Subsequently, their energy adds up with the 5970 keV alphas, thus increasing the final intensity of the observed 6034 keV g.s. to g.s. α-decay peak. This process of energy summing in the DSSD detector has been tested and confirmed by the simulation of the ^{175}Pt α decay. In this simulation, conversion coefficients for transitions depopulating the low-lying negative-parity states in ^{171}Os (see Fig. 3.1) were adopted from [33]. Results of this simulation are presented in Fig. 3.4. In this figure, a simulated spectrum (red) and measured data (blue) are displayed together. One can see that positions of the ^{175}Pt α-decay peaks (labelled with energies) and their respective intensities

in the two spectra are almost identical. This confirms our interpretation in regards to the ^{175}Pt α decay.

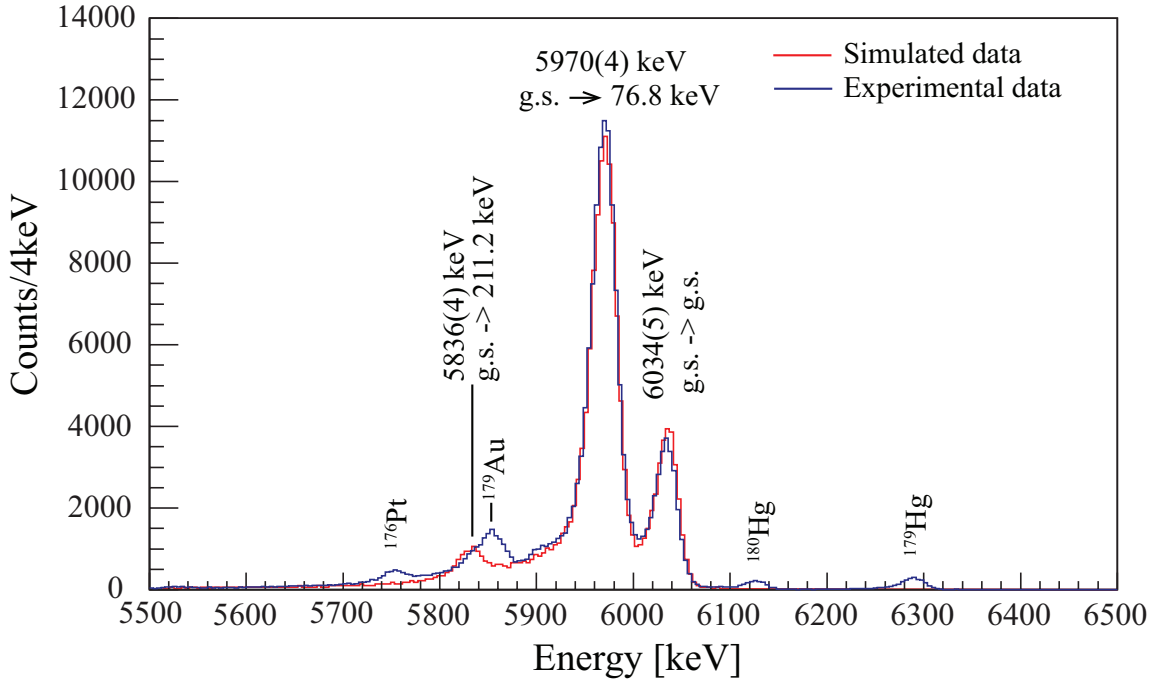

Figure 3.4: Results of the simulation of the ^{175}Pt α decay. Measured (blue) and simulated (red) data are shown. Energy spectrum of measured α decays was obtained by gating on the 6287 keV parent α decay in the ER-α_1-α_2 matrix shown in Fig. 3.3. Peaks that are not in the simulation, but appear in the measured data are contamination from other decays. The peak at position 5836(4) keV in the simulated data is part of multiplet with significant contamination from the ^{179}Au α decay with energy of 5854(7) keV.

However, four α-decay branches of ^{175}Pt were observed in [11]. Two of these observed α-decay branches have energy difference of 4 keV. Since it is not possible to distiguish between two α-decay peaks with 4 keV energy difference in the DSSD detector, a background subtracted α-γ matrix has been constructed. First, an α-γ coincidence matrix was constructed using search times: $\Delta t(\gamma-\alpha) \leq 200$ ns between α-decay and γ-ray events and $\Delta t(\alpha-\text{ER}) \leq 3$ s for correlated α decays. Afterwards, a second matrix was constructed using modified search times $\Delta t(\alpha-\gamma) \leq 200$ ns. This second matrix was then subtracted from the original one. The final background subtracted matrix is shown in Fig. 3.5. By gating on the 131 and 134 keV γ-ray transitions (see Fig. 3.1) respectively, in the α-γ matrix, two α decays with energies of 5836(4) and 5840(7) keV are observed. This confirms the existence of the g.s. $\rightarrow$ g.s. plus three fine-structure α-decays in ^{175}Pt.

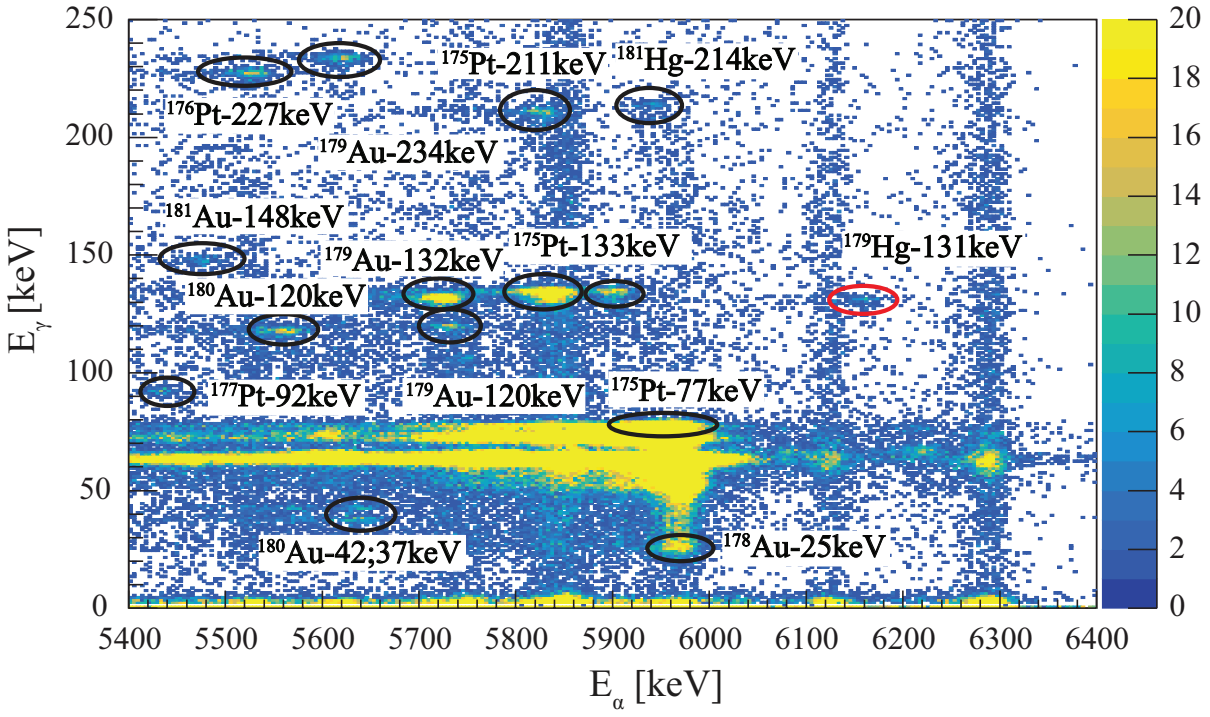

Figure 3.5: The α-γ coincidence matrix, measured with the DSSD detector and focal plane HPGe Clover and planar detectors. Time windows used to search for α-γ coincidences are $\Delta t(\gamma-\alpha)=200$ ns, together with $\Delta t(\alpha-\mathrm{ER})\leq 3$ s for correlated α decays. Due to presence of Pt, Ir, Os and Re x rays, coincidences with $E_\gamma = 60$ - 75 keV are present in the matrix.

The new α-decay branch in ^{179}Hg

In the analysis of the α-γ matrix (see Fig. 3.5), a previously unidentified coincidence between 6156(7) keV α decay and the 131.3(7) keV γ ray was observed. The sum of the α-decay Q value with 131.3 keV γ ray is equal to 6428(7) keV. This is within the error bars of the Q value 6431(5) keV, which belongs to the ^{179}Hg ground state to ground state α decay. By gating on the 6156 keV α-decay peak in the α-γ matrix, the 63.6, 67.1 and 131.7 keV γ rays are observed. Two remaining transitions with energies 63.6(6) and 67.1(5) keV were identified as $K_{\alpha 1}$ x rays in Os and Pt, respectively. For better identification of the isotope, a spectrum of child alphas (shown in Fig. 3.6) correlated with $E_{\alpha 1}=6156$ keV in the ER-α_1-α_2 matrix (see Fig. 3.3), was constructed. In this spectrum, the ^{175}Pt α decays are observed, together with α decay of ^{176}Pt. The energy gate is contaminated with the ^{180}Hg α decay with an energy of 6120(5) keV, which in turn causes a presence of the ^{176}Pt α decay in the gated spectrum. The remaining peaks are random correlations. Finally, the distribution of time differences $\Delta t(\alpha$-ER) for the 6156 keV α particles in coincidence with 131.3 keV γ rays is shown in Fig. 3.7. The α decays, inside (black) rectangles in Fig. 3.8a were selected

to be correlated with the detection of recoil. An exponential decay curve with a constant background was used to fit the data. The resulting half-life is 0.98(9) s. This value agrees with the known half-life $T_{1/2} = 1.05(3)$ s [73] of the 6287 keV α decay of ^{179}Hg. Based on these arguments, the 6156 keV α decay was assigned as the decay of ^{179}Hg populating the 131.3 keV excited state in ^{175}Pt.

Basic characteristics of the newly observed 6156 keV α-decay branch in ^{179}Hg were ex-

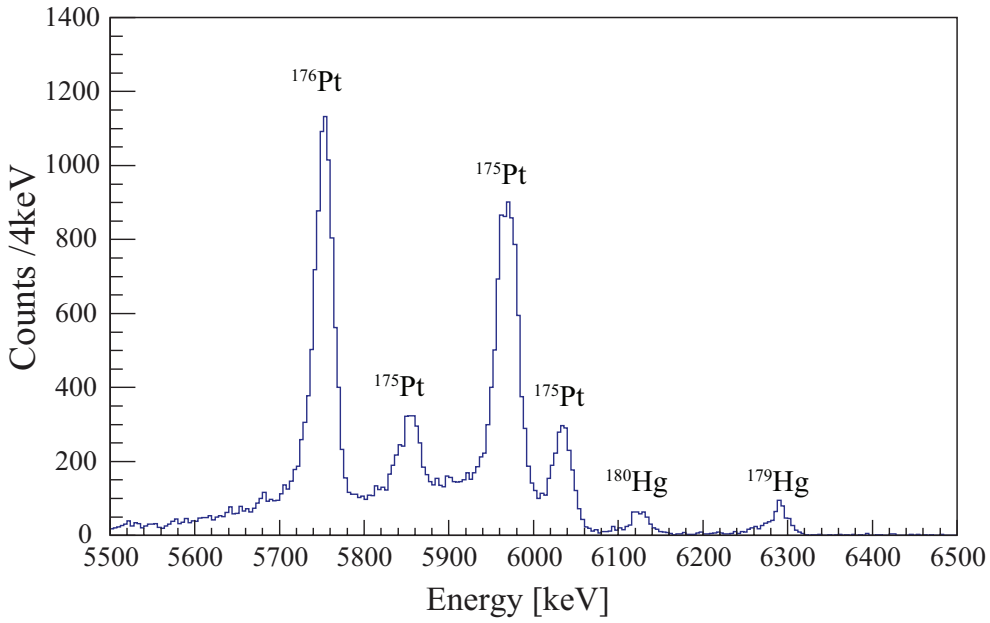

Figure 3.6: Energy spectrum of child α decays correlated with the 6156 keV parent α decay in the α-α matrix shown in Fig. 3.3. 3.3.

tracted from the measured data. The partial branching ratio $b_\alpha(6156)$ was determined using the total $b_\alpha = 75(4)\%$ [70] divided as follows: (a) the number of 6287 keV alphas detected in the DSSD detector, see Fig. 3.2, (b) the number of 131.3 keV γ rays observed in coincidence with 6156 keV α decays shown in Fig. 3.5, normalized to detection efficiency of the planar Ge detector [74] and corrected for background contribution, see section below. This gives us $b_\alpha(6156) = 0.20(8)\,\%$. In accordance to that, the previously reported total b_α needs to be lowered to 74.8(41) %. The obtained branching ratios were used in the further analysis to calculate reduced α decay widths for both α decay branches using the Rasmussen method [28]. The change in angular momentum $\Delta L = 0$ along with $\Delta L = 2$ was assumed for α decays populating the ground state and the 131.3 keV excited state in ^{179}Hg, respectively. The values are 1.7(7) keV and 65(7) keV for $E_\alpha = 6156(7)$ keV and 6287(5) keV, respectively. Lastly, hindrance factors were calculated as 41(19) and 1.2(3) for the α decay populating 131.3 keV excited state and ground state in ^{175}Pt, respectively. They were calculated relative to reduced

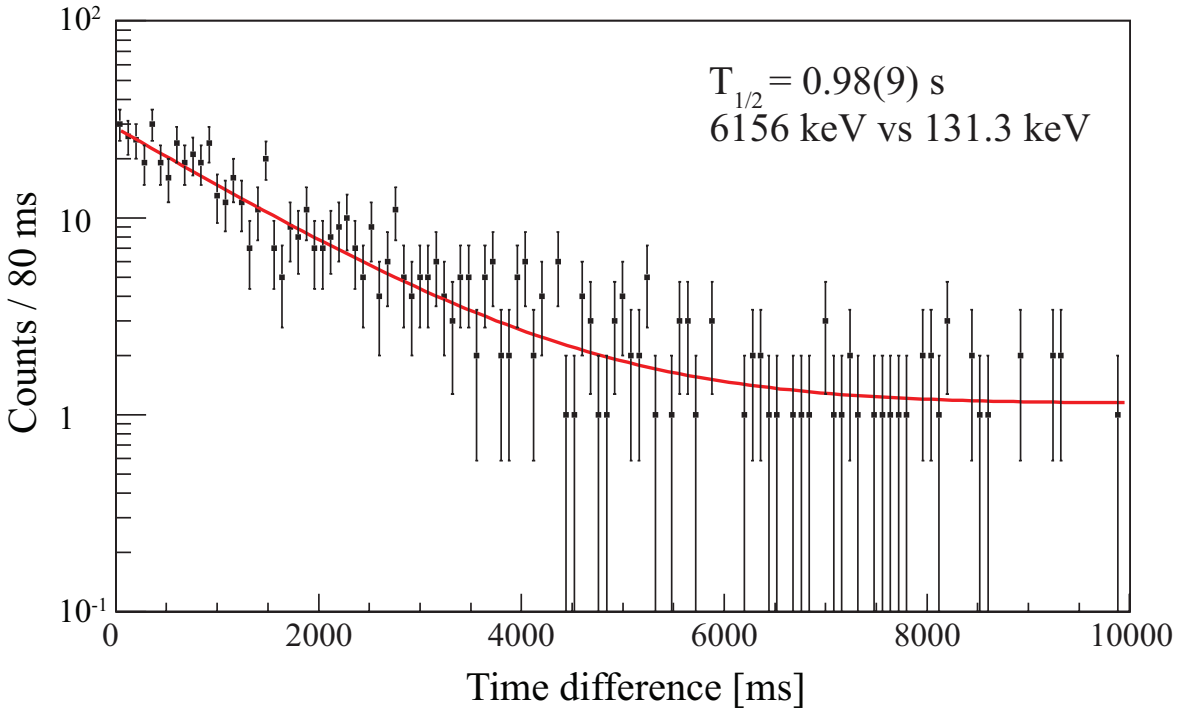

Figure 3.7: Time distribution of ^{179}Hg α decay leading to 131.3 keV excited state in ^{175}Pt. Search times $\Delta t_1(\alpha\text{-ER}) < 3$ s and $\Delta t(\gamma\text{-}\alpha) < 200$ ns were used along with a (black) 2-dimensional gate used in 3.8a. An exponential decay curve with a constant background was used to fit the data points and is shown as a solid red line. The measured half-life is 0.98(9) s

α decay widths for unhindered 0^+ to 0^+ decays in neighbouring even-even nuclei, ^{178}Hg and ^{180}Hg.

Inspection of the α-γ coincidence data displayed in Fig. 3.5 allowed the conversion coefficient of the 131.3 keV transition in ^{175}Pt to be measured for the first time. In the matrix 3.8a, the 131 keV γ-ray and Pt K$_\beta$ x-ray events were selected using the (black) 2-dimensional gates. To quantitatively characterize the background contribution of these events, the average number of events in (red) 2-dimensional gates defined separately for both types of "good" coincident events was evaluated and subtracted. From this calculation, a total number of 78(30) Pt K$_\beta$ x-ray events and 68(33) and 131 keV γ-ray events were obtained, respectively. The number of Pt K$_\beta$ x rays was then normalized to Pt K x rays using intensities from [33]. The conversion coefficient α_K(131 keV) was calculated to be 3.9(23). Owing to a large uncertainty of experimentally deduced conversion coefficient, two different transition multipolarities are possible: $\alpha_K(M1) = 2.32(4)$ and $\alpha_K(E4) = 2.57(4)$. Since the 131.3 keV transition is seen as prompt, the higher order multipolarities are excluded and $M1$ multipo-

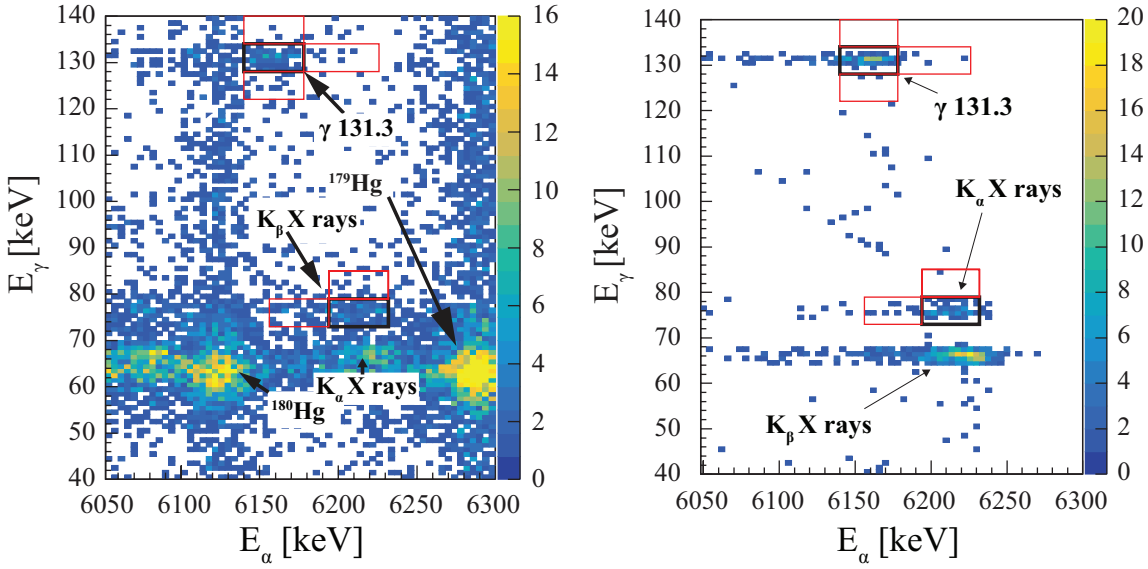

(a) Experimental data

(b) Simulated data

Figure 3.8: (a) The background subtracted α-γ coincidence matrix measured with the DSSD and the focal-plane planar Ge detector, and (b) the simulated data. Time conditions used to search for coincidences: $\Delta t(\alpha$ - ER $) < 3$ s and $\Delta t(\gamma - \alpha) < 200$ ns. The data in panel (b) were simulated in GEANT4. The energy of α particles in coincidence with Pt k_β x rays is shifted due to α-particle and conversion-electron energy summing.

E_α[keV]	b_α [%]	δ^2[keV]	HF	E_{level} [keV]	Multipolarity
6287(5)	74.8(42)	65(7)	1.2(3)	0	
6156(7)	0.20(8)	1.7(7)	41(19)	131.3(5)	$M1$

Table 3.1: Summary of ^{179}Hg α-decay characteristics deduced in this work. Alpha-decay energy (E_α), branching ratio (b_α), reduced width (δ^2), and hindrance factor (HF), together with the energy level populated by the α decay (E_{level}) and multipolarity ($M\lambda$) of the γ ray de-exciting the energy level.

larity is assigned to this transition. The results are summarized in Table 3.1. The α-decay scheme of ^{179}Hg deduced in this work is presented in Fig. 3.9. To confirm our results, a GEANT4 simulation [75] was performed.

3.2.1 Simulation of the ^{179}Hg decay

A simulation of the ^{179}Hg α decay was performed in GEANT4. Firstly, an implantation depth of the ^{179}Hg nuclei in the DSSD detector needed to be calculated as it was later used as an input in the simulation of the α decay process. The SRIM/TRIM software [76] was used to calculate the ionisation losses of projectiles and ^{179}Hg nuclei in different parts of the experimental setup. This was used to calculate the energy of ^{179}Hg nuclei entering the DSSD

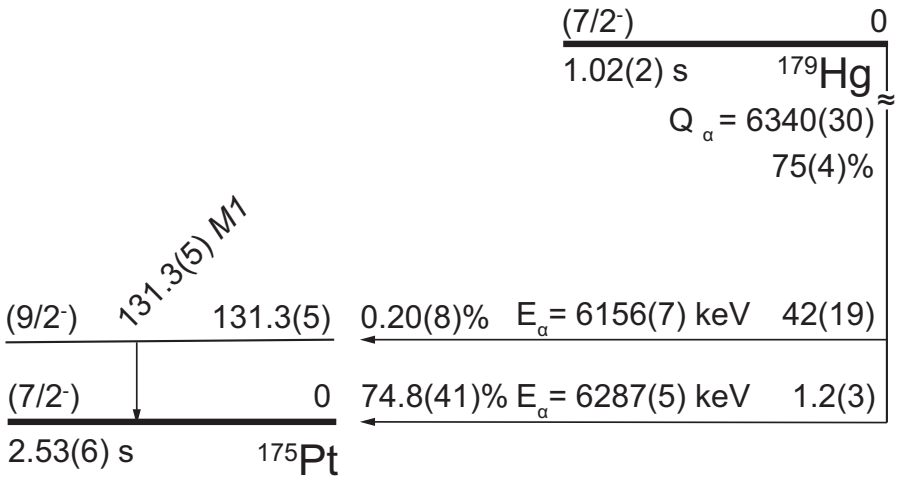

Figure 3.9: The α-decay scheme of ^{179}Hg deduced in this work.Ground-state properties of ^{179}Hg and ^{175}Pt are adopted from [11, 70], respectively.

detector and, thereafter, to determine the maximum implantation depth of ^{179}Hg nuclei into the DSSD detector. The ionisation losses of projectiles in the target are lower compared to ^{179}Hg nuclei. For this very reason, a production of compound nuclei was assumed to take place at the rear end of the target. The energy losses of projectiles in the target were calculated to be 8.4 MeV. The Q-value of the aforementioned nuclear reaction $Q = 177.1$ MeV was calculated using the online Q-value calculator (QCalc) [77]. The energy of ^{179}Hg nuclei at the entrance of the RITU separator was 166.5 MeV. Because the RITU separator is filled with diluted He gas, energy losses in this part of the experimental setup were neglected. Subsequently, the ^{179}Hg nuclei passed through the MWPC detector, which is composed of two Mylar foils, one Al coated anode, and the detector's volume is filled with isobutane gas with pressure of 2 - 3.5 mbar. In the MWPC detector, the initial energy was reduced by another 37 MeV. Finally, the ^{179}Hg ions with an energy of 129.5 MeV were implanted into into one of the DSSD detectors, and their implantation depth was determined to be 15.3 μm. Results of this simulation are summarised in Table 3.2. Following that, a simulation of the ^{179}Hg α decay was performed. An $M1$ multipolarity was assumed for the 131.3 keV transition. The basis for this assumption is the tentatively assigned $I^{\pi} = (9/2^{-})$ for the 130.9 keV excited state in ^{175}Pt [11]. The α-γ matrix as a result of the simulation is presented in Fig. 3.8b. When looking at matrices shown in Fig. 3.8, it can be immediately noticed that the position of α - Pt K x-ray coincidences is shifted compared to the position of α - 131.3 keV γ-ray coincidences in both. This is due to the summing effect of α-particle energies with energies of conversion, Auger and Coster-Kronig electrons. Because of atomic relaxation after internal

conversion of the 131.3 keV transition, K_β x rays can be emitted. By measuring the number of 131.3 keV γ rays and the K $_\beta$ x rays, the K-internal conversion coefficient can be deduced.

Particle	Material	Ionization losses dE/dx [MeV]	Depth [μm]
^{82}Kr (projectile)	^{100}Ru (target)	8.4	0.28
^{179}Hg	MWPC	37	12002.78
^{179}Hg	DSSD	129.5	15.3

Table 3.2: Simulated data for ionisation energy losses (3^{rd} column) of the projectile and ^{179}Hg ions in the target, MWPC and DSSD detectors, respectively. The nuclear reaction $^{100}_{44}$Ru($^{82}_{36}$Kr, 3n)$^{179}_{80}$Hg and initial beam energy of 352 MeV were used. The 1^{st} column gives particles for which the ionization losses were calculated. The 2^{nd} column represents different parts of the experimental setup. The 4^{th} column represents the thickness of the target and the MWPC detector along with the implantation depth in the DSSD detector. In case of the MWPC detector, following materials had to be taken into account: Mylar foils, isobutane gas, anode and Al coating [78].

3.2.2 Discussion - ^{179}Hg

The decay scheme of ^{179}Hg and its decay characteristics are shown in Fig. 3.9 and Table 3.1, respectively. The suggested (9/2$^-$) spin-parity assignment for the 131.3 keV excited state in ^{175}Pt [11] is now supported by the calculated value of hindrance factor HF = 41(19) since the most probable assignment for the ground state of ^{179}Hg is (7/2$^-$) [79]. The calculated conversion coefficient α_K(131.3 keV) = 3.9(23) suggest the $M1$ multipolarity for the 131.3 keV γ-ray transition which further corroborates the (9/2$^-$) assignment.

Similar transitions can be seen in neighbouring ^{175}Pt isotones. In ^{173}Os, a 128 keV transition between the 9/2$^-$ excited state at 219.6 keV and (7/2$^-$) excited state at 91.6 keV was observed [80]. An $M1$+$E2$ multipolarity was assigned to the 128 keV transition. In the level scheme, it was placed as an interband transition in the rotational band 2 (see Fig. 3 in [80]). The ground state in ^{173}Os dominated by the 5/2$^-$ [523] Nilsson configuration [80]. Another similar situation was observed in ^{171}W, where the 131.4(1) keV transition depopulates the (9/2$^-$) excited state at 233.2 keV down to the (7/2$^-$) excited state at 101.7 keV. This 131.4 keV transition was assigned an ($M1$) character. It is a known interband transition between bands E and F (see Fig. 1 in [81]), built on top of the 5/2$^-$ ground state, identified as the 5/2$^-$ [523] Nilsson configuration. Furthermore, in ^{169}Hf a 130.0(1) keV γ ray

is emitted from the (9/2$^-$) excited state at 288.73 keV. It populates the (7/2$^-$) excited state at 158.79 keV. The multipolarity of this 130.0 keV γ ray was deduced to be ($M1$+$E2$) with assigned 5/2$^-$ [512] band [82]. The evolution of the 131.3 keV transitions in neighbouring isotones is shown in Fig. 3.10.

A similar trend in the evolution of the 131.3 keV transition can be observed in the neighbouring Pt isotopes. In ^{177}Pt the 116.1(5) keV γ ray was observed to depopulate the 9/2$^-$ excited state at 197.4 keV down to the 7/2$^-$ excited state at 81.2 keV. In this case, the 116.1 keV γ-ray transition is part of the 5/2$^-$ [512] ground state band with assigned ($M1$+$E2$) multipolarity [83]. The trend slightly changes in ^{179}Pt, because the 110.7 keV transition, connecting (9/2$^-$) excited state at 255.5 keV with (7/2$^-$) excited state at 144.8 keV does not have a multipolarity attributed. Moreover, it is build on the 5/2$^-$ [512] intrinsic state, with no connection to the 1/2$^-$ [521] ground state band [84]. In ^{181}Pt there is a 118.88(9) keV transition which goes down from (9/2$^-$) 235.4 keV excited state to the (7/2$^-$) excited state at 116.65 keV. Here, the 118 keV γ-ray transition has ($M1$) character and it is a 7/2$^-$ [514] in-band transition [85]. Lastly, in ^{183}Pt a 115.2(1) keV transition was observed. It connects the (9/2$^-$) excited state at the 149.91 keV with 7/2$^-$ excited state at 34.74 keV. This 35 keV state was observed to be isomeric with 7/2$^-$ [514] Nilsson configuration. Compared transitions are shown in Fig. 3.11. Unfortunatelly, none of the 9/2$^-$ excited states were seen to be populated by an α decay and most of the neighbouring isotopes are populated by EC decay.

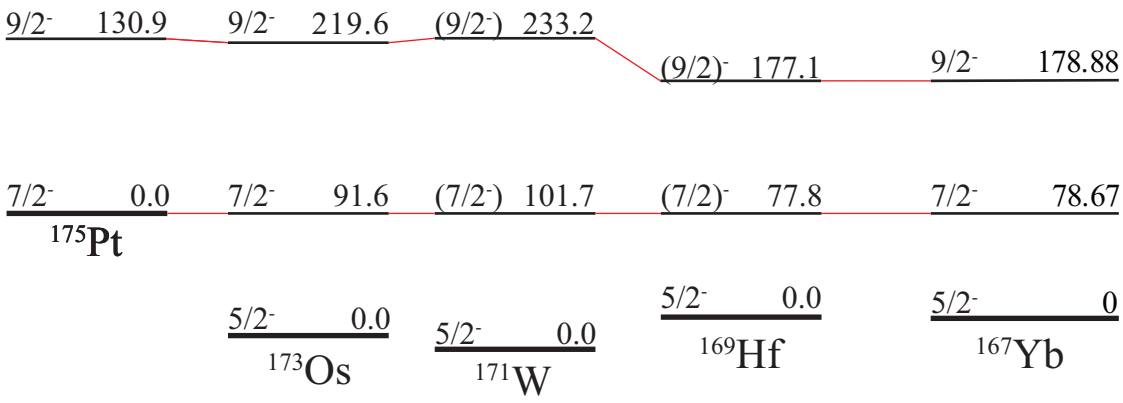

Figure 3.10: Systematics of the 9/2$^-$ and 7/2$^-$ states together with the ground states in neighboring isotones. The data are taken from present work and from [60].

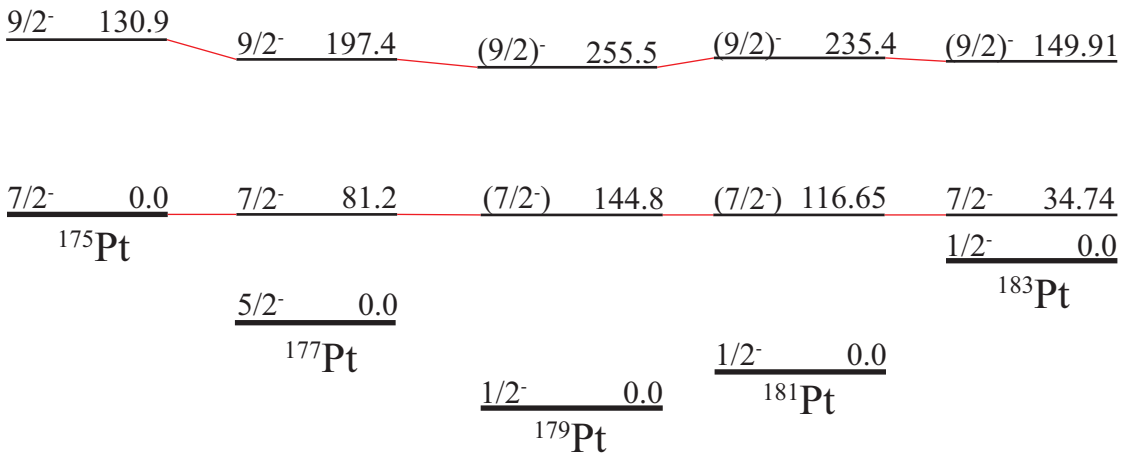

Figure 3.11: Systematics of the $9/2^-$ and $7/2^-$ states together with the ground states in neighboring Pt isotopes. The data are taken from present work and from [60].

3.2.3 Other α-γ coincidences

In this section, the remaining prompt α-γ coincidences observed in the corresponding α-γ matrix shown in Fig. 3.5 were analyzed. First, α-decay energies were compared with the most up-to date tables [59], [60]. Subsequently, total $Q_{\alpha,total}$ values were calculated. The assignment for all of them has been done and the complete list is shown in Table 3.3. In case of α decay of ^{179}Au, the g. s. $\rightarrow$ g. s. α decay was observed with energy $E_\alpha = 5855(6)$ keV. This energy is slightly different from previous 5848(4) keV measured in [86]. Furthermore, three fine-structure α decays of ^{179}Hg were identified in [86]. Their respective energies are 5718(10) keV, 5705(15) keV and 5600(10) keV. However, the analysis of the α-γ coincidence matrix 3.5 from the S17 experiment revealed different energies: 5745(6) keV, 5733(5) keV, 5725(5) keV and 5624(6),keV while gating on 105 keV, 119 keV, 132 keV and 234 keV γ rays, respectively. The comparison of α-energy projections (left) acquired from this work and (right) spectra from [86] are shown in Fig. 3.12. The shift in α-decay energies is caused by the summing of α-particle energies with conversion and Auger electrons. For example, the 5745(6) keV α decay, which should feed the same 132 keV excited state as 5725(5) keV α decay, was observed with higher energy. The 105.9(5) keV γ-ray transistion was assigned as a de-excitation from the 131.9 keV level down to the excited state at 26.1(4) keV in ^{175}Ir. This 26.1 keV excited state is depopulated by the prompt 26.1 keV $M1$ transition [86]. The conversion coefficient of the 26.1 keV transition is $\alpha_K(M1) = 56(3)$, [33]. Therefore, a conversion electron with an energy of 12.68 keV [33] will be emitted directly after the α decay and its energy will be summed with the α decay energy. Subsequently, an atomic relaxation

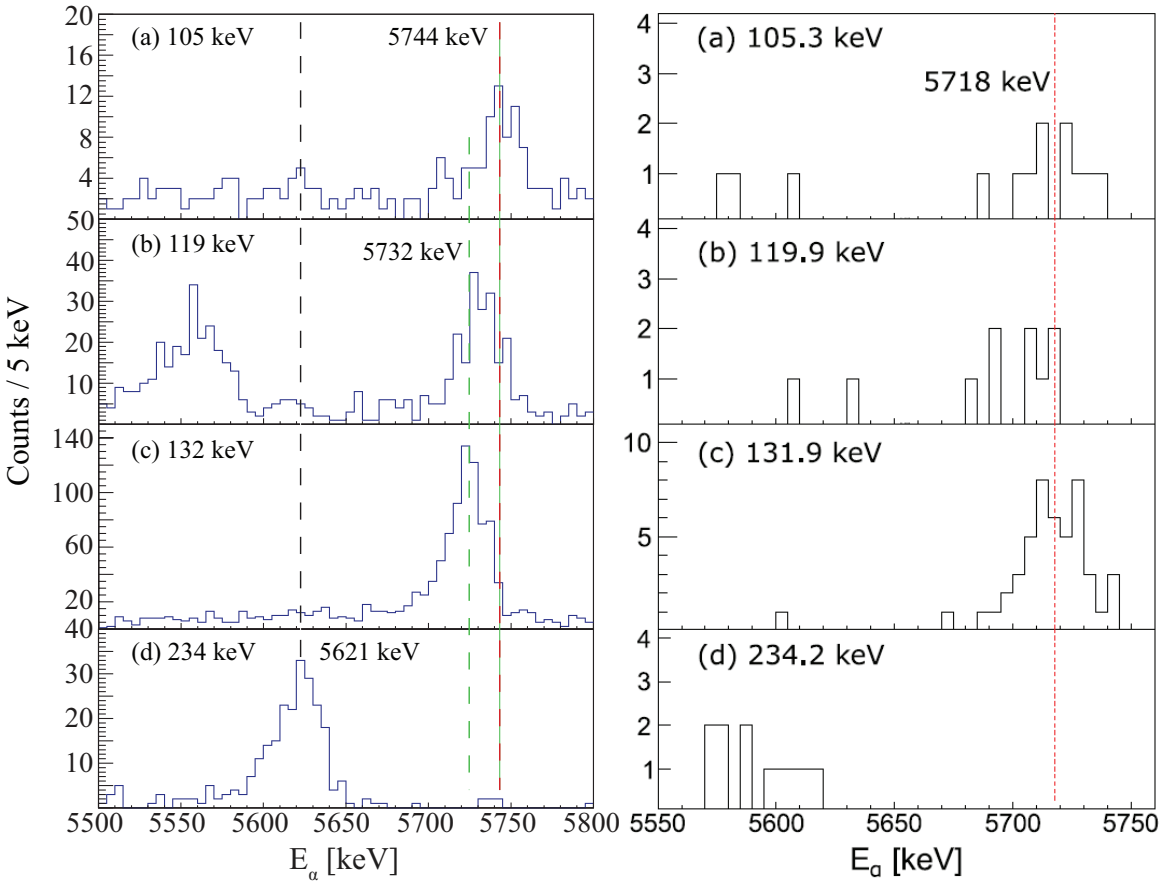

Figure 3.12: Projections on the α-energy axis from the α-γ coincidence matrix 3.5 gated on γ rays indicated in left corner. (left) Data from the S17 experiment. (right) Figure taken from [86].

occurs, and a 12.43 keV Auger electron may be emitted. This changes the summed 5745 keV α decay, observed in this work, to 5720 keV, which correspond to the 5718(10) keV published in [86]. The 5725(7) keV α decay is not affected, because the 132 keV transition populates the ground state in ^{175}Ir and therefore no additional electrons can be summed with the energy of α particle. Similar situation was observed in the remaining ^{179}Au α decays populating excited states at 146.0(7) keV and 260.3(7) keV in ^{175}Ir. The same effects of conversion and Auger electron summing was observed in the α decay of ^{180}Au. Recently, six fine-structure α decays with energies 5354(20), 5425(20), 5485(10), 5512(15), 5598(8) and 5639(7) keV were observed in [87]. Three α decays with energies 5642(6) keV, 5638(6) keV and 5563(6) keV coincident with 36.7(7) keV, 42.0(6) keV and 117.7(6) keV γ rays, respectively, were identified in Fig. 3.5. The emaining α-decay branches have $b_\alpha < 5$ % and were not observed in our data. The comparison between α-energy projections gated on respective γ rays (left) measured in this work with (right) observed in [87] are shown in Fig. 3.13.

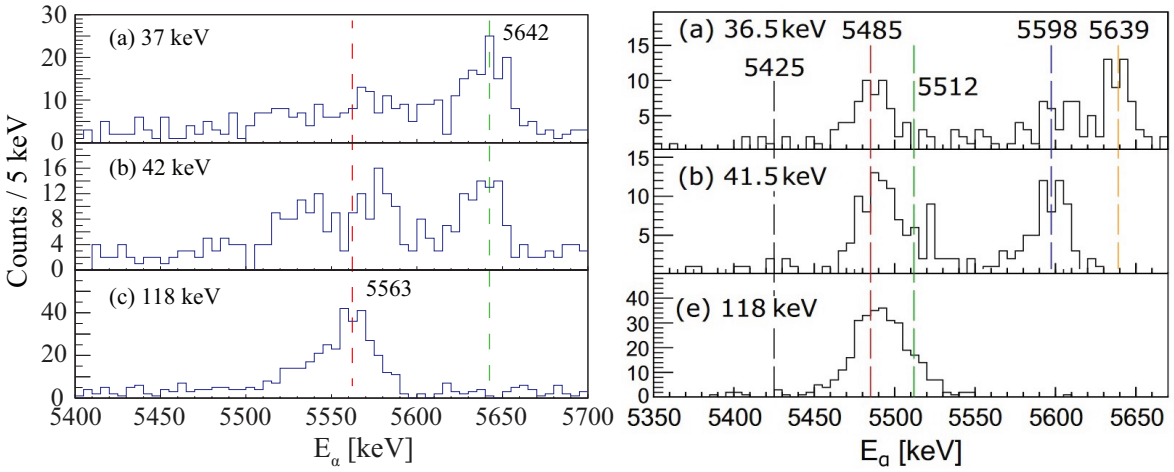

Figure 3.13: Projections on the α-energy axis from the α-γ coincidence matrix 3.5 gated on γ rays indicated in left corner. (left) Data from the S17 experiment. (right) Figure taken from [87].

Notice the shift of α-decay peaks in spectra gated on the 42 keV and 118 keV transitions. Moreover, in [87] the 5639 keV peak is not present in the spectra gated on the 42 keV transition. Both of these effects can be attributed to the conversion and Auger electrons summing. The conversion coefficient of the 37 keV transition is $\alpha(37,\, M1) = 19.8(12)$ [33]. As such, it is a strongly converted transition causing production of the conversion electrons with an energy of 24.28 keV. Adding up the energy of Auger electrons leads to the shift in 37 keV in α-particle energy. By subtracting this energy from the 5642 keV alphas, one gets an energy value of 5605(6) keV. Within the experimental uncertainties, it agrees with the energy of the 5598(8) keV α decay leading to the 78.0(4) keV excited state in ^{176}Ir. The same correction will change the 5563(6) keV α-decay energy to a new value of 5486(6) keV, which agrees well with the 5485(10) keV energy published in [87].

For completeness, the delayed α-γ coincindence matrix was constructed, see Fig. 3.14. In this matrix, the search times for α-γ coincindences were set to 200 ns$\leq \Delta t(\gamma - \alpha) \leq$ 700 μs along with $\Delta t(\alpha - \mathrm{ER}) \leq 3$ s for α decays correlated with registered recoils. The goal of this analysis was to search for delayed γ rays and therefore identify possible isomeric states. A clear coincidence between the 6005(6) keV α decay and the 147.5(6) keV γ ray can be seen. This coindicence belongs to the known 6006(5) keV α decay of ^{181}Hg which populates the 147.4(10) keV excited state. The 147.4 keV excited state was identified to be a 2.2(3) μs isomer [69]. For verification, a time difference spectra between 6005 keV α decays and

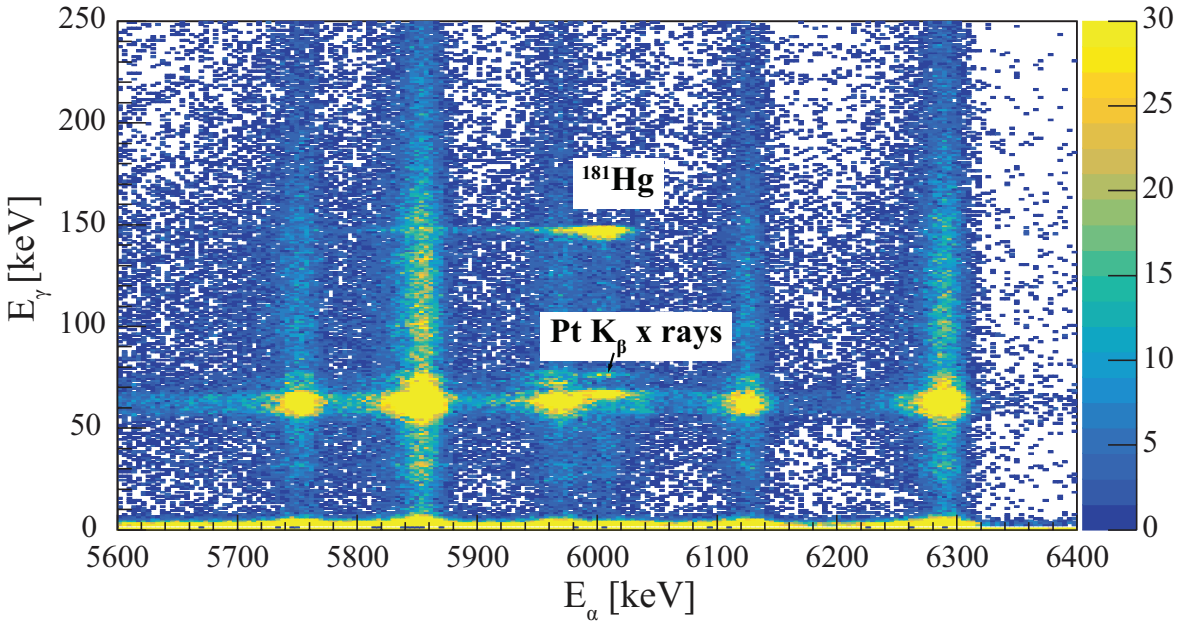

Figure 3.14: The delayed α-γ coincidence matrix from the S17 experiment, measured with the DSSD detector and focal plane planar detector. Time windows used for coincidence search are $\Delta t(\gamma - \alpha) \leq 700\,\mu$s, and $\Delta t(\alpha - \mathrm{ER}) \leq 3$ s for correlated α decays. The non-marked coincidences arise from random coincidences between Re, Os, Ir and Pt x rays and main α decays (see Fig. 3.2).

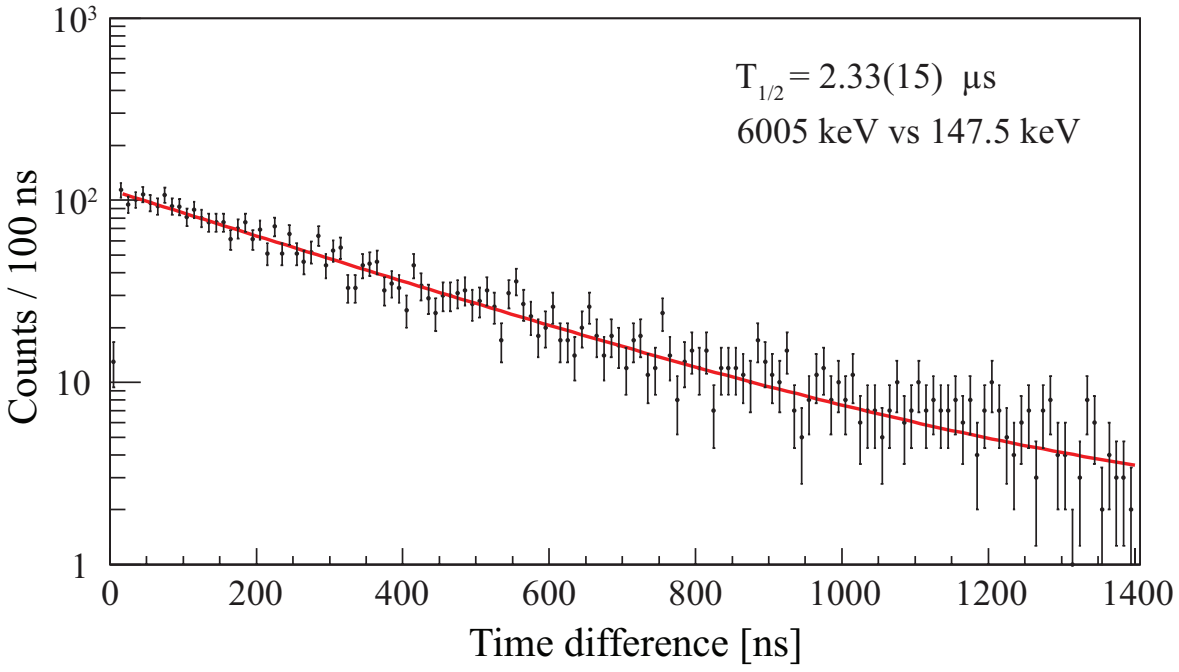

Figure 3.15: Distribution of time differences between 6005 keV α decays in coincidence with 147.5 keV γ rays, see Fig. 3.14. An exponential decay curve with a constant background was used to fit the data points and is shown as a solid red line. The measured half-life is 2.33(15) μs.

Parent nucleus	E_α^{exp} [keV]	E_α^{tab} [keV]	E_α^{tab} Reference	Child [keV]	E_γ [keV]	$Q_{\alpha,tot}$	$I_i \rightarrow I_f$
^{176}Pt	5529(4)	5537(10)	[69]	^{172}Os	229.0(10)	5885(5)	$5/2^- \rightarrow 7/2^-$
^{177}Pt	5433(5)	5435(10)	[69]	^{173}Os	92.5(7)	5651(5)	$2^+ \rightarrow 0^+$
^{181}Hg	5945(8)	5934(9)	[69]	^{177}Pt	214.2(6)	6293(8)	$1/2^- \rightarrow (3/2^-)$
^{181}Hg	6008(6)	6005(4)	[69]	^{177}Pt	147.8(6)	6292(4)	$1/2^- \rightarrow 1/2^-$
^{178}Au	5967(9)	5961(10)	[88]	^{174}Ir	26.0(10)	6130(9)	$(7^+, 8^+) \rightarrow$ (-)
^{179}Au	5744(8)	5718(10)	[86]	^{175}Ir	105.9(7)	5981(8)	$(1^+) \rightarrow$ (-)
^{179}Au	5732(7)	5705(15)	[86]	^{175}Ir	119.8(6)	5983(7)	$(1^+) \rightarrow$ (-)
^{179}Au	5725(7)	5718(10)	[86]	^{175}Ir	132.0(6)	5988(7)	$(1^+) \rightarrow$ (-)
^{179}Au	5621(8)	5600(10)	[86]	^{175}Ir	234.0(5)	5983(8)	$(1^+) \rightarrow$ (-)
^{180}Au	5637(10)	5639(7)	[87]	^{176}Ir	37.7(7)	5803(10)	$(1^+) \rightarrow$ (-)
^{180}Au	5574(11)	5598(8)	[87]	^{176}Ir	43.0(6)	5744(11)	$(1^+) \rightarrow$ (-)
^{180}Au	5562(9)	5485(10)	[87]	^{176}Ir	117.7(6)	5806(9)	$(1^+) \rightarrow$ (-)
^{181}Au	5476(7)	5479(5)	[89]	^{177}Ir	150.0(6)	5750(7)	$(1^+) \rightarrow$ (-)

Table 3.3: Table of identified α-γ coincidences. The 2^{nd} and 6^{th} column denotes measured energies of α and γ-ray transitions, while the 3^{rd} represents tabulated values. The 4^{th} column contains references for the E_α^{tab}. The 7^{th} column represents the $Q_{\alpha,tot}$. The last column represent initial I_i and final I_f spins and parities for γ-ray transitions in child nuclei. In the case of ^{178}Au, the spin and parity of the initial level are unknown.

147.5 keV γ rays was created, see Fig. 3.15. The resulting half-life of this isomeric state was determined to be $T_{1/2}$(147.5 keV) = 2.33(15) μs. This agrees with the published value 2.2(3) μs [69].

3.3 Previous study of ^{177}Au

The first study of ^{177}Au α decay was performed by A. Siivola [71]. There, one α-decay branch was observed with E_α = 6.15(1) MeV and $T_{1/2}$ = 1.3(4) s. Later on, a second α decay branch was assigned to the ^{177}Au α decay by H. Gauvin *et al.* [72] with E_α = 6.15(1) MeV. A somewhat different half-life $T_{1/2}$ = 1.18(7) s was measured by P. J. Sellin *et al.* [90]. The half-life was differentiated for both α-decay branches in the study by F. G. Kondev *et al.* [91], with $T_{1/2}$ = 1.180(12) s and $T_{1/2}$ = 1.462(32) s for the 6.12 MeV and 6.16 MeV α decays of ^{177}Au, respectively. In the same study, both states depopulated by an α decay were characterized by Nilsson configurations. For the ^{177}Au ground state a tentative ($1/2^+$, $3/2^+$) assignment was proposed. The suggested configuration was $d_{3/2}$ $1/2^+$ [411] at oblate deformation or $d_{3/2}$ $3/2^+$ [402] at prolate deformation. For the isomeric state depopulated by 6.12 MeV α

decay, the $h_{11/2}$ 11/2$^-$ [505] Nilsson configuration was assigned. Later on, the ^{177}Au α decay was studied by A. N. Andreyev *et al.* [92]. There, branching ratios were calculated as b_α = 40(6) % and b_α = 66(10) % for 6161(7) keV and 6124(7) keV α decays, respectively. Moreover, reduced α decay widths were determined as δ^2 = 29(5) keV and δ^2 = 82(14) keV for the α decay depopulating the ground state and (11/2$^-$) isomeric state in ^{177}Au, respectively. For easier distinction, ^{177}Au^g and ^{177}Au^m were used. Moreover, the 6124 keV α decay was established to depopulate the (11/2$^-$) isomeric state at 189(16) keV in ^{177}Au down to the (11/2$^-$) excited state at 226(18) keV in ^{173}Ir. Recently, a new 5932(12) keV α decay branch in ^{177}Au was identified by R. D. Harding *et al.* [86]. It decays from the (11/2$^-$) isomeric state at 181.9(4) keV in ^{177}Au to the (9/2$^-$) excited state at 424.4(13) keV in ^{173}Ir. Moreover, the reported branching ratios were 56(8)% and 64% for the ^{177}Au^m and ^{177}Au^g, respectively. The two branches from the ^{177}Au^m α decay were divided as $I_{\alpha,rel}(5932) = 1.5(5)$ % and $I_{\alpha,rel}(6125) = 98.8(5)$ %. The α decay level scheme, deduced in [86], is shown in Fig. 3.16.

3.4 Results of the Experiment JR115

In this section, the data collected in the experiment JR115, carried out on October 18 - October 30, 2012 at JYFL, Finland, are presented. The ^{177}Au nuclei were produced in the fusion-evaporation reaction $^{92}_{42}$Mo($^{88}_{38}$Sr, p2n)$^{177}_{79}$Au. The self-supporting $^{92}_{42}$Mo target (98 % enrichment) with 600 μg/cm^2 thickness was bombarded by the $^{88}_{38}$Sr^{16+} ion beam, accelerated to an energy of 399 MeV by the K-130 cyclotron. The average beam intensity was approximately 2 pnA. Total α-particle energy spectrum measured with the DSSD detector is shown in Fig. 3.17.

In order to identify measured, and potentially unknown α-γ coincidences, $i.e.$ to study the α-decay fine structure in this mass region of nuclear chart, the data were analysed in a similar fashion as those from S17 experiment. Firstly, the total α-particle spectrum measured in the DSSD detector was analyzed, see Fig. 3.17. There, the peaks at 6118 keV and 6154 keV were identified as α decay of ^{177}Au. Considering the number of various evaporation channels open in the reaction, the presence of the α-decay fine structure should be significant. Time- and energy-wise, no constraints were given by any particular isotope in contrast to analysis of S17 experimental data. Search times $\Delta t(\alpha_1 - \mathrm{ER}) \leq 4$ s between the detection of

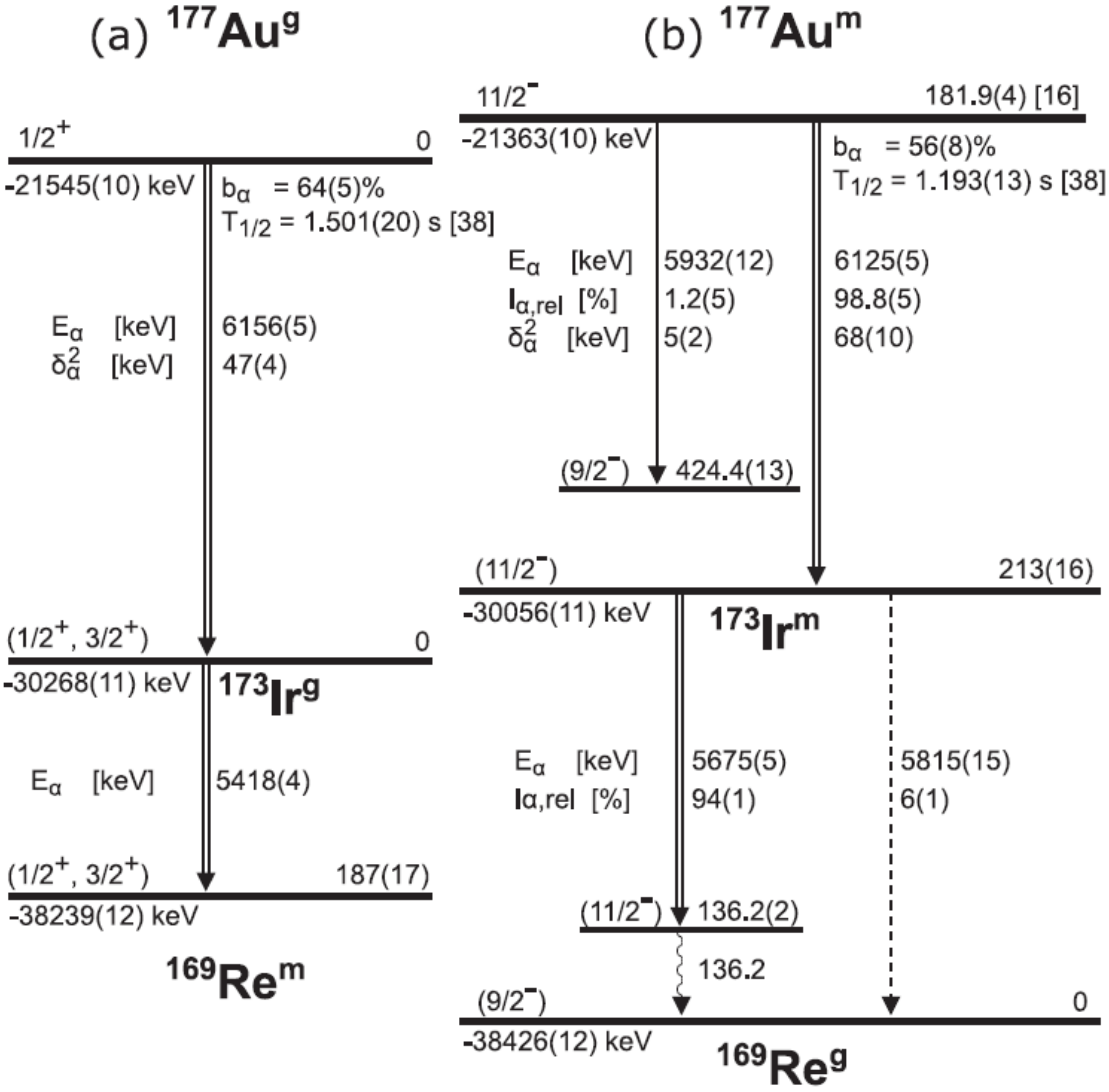

Figure 3.16: The α-decay scheme of ^{177}Au. Figure was taken from [86]

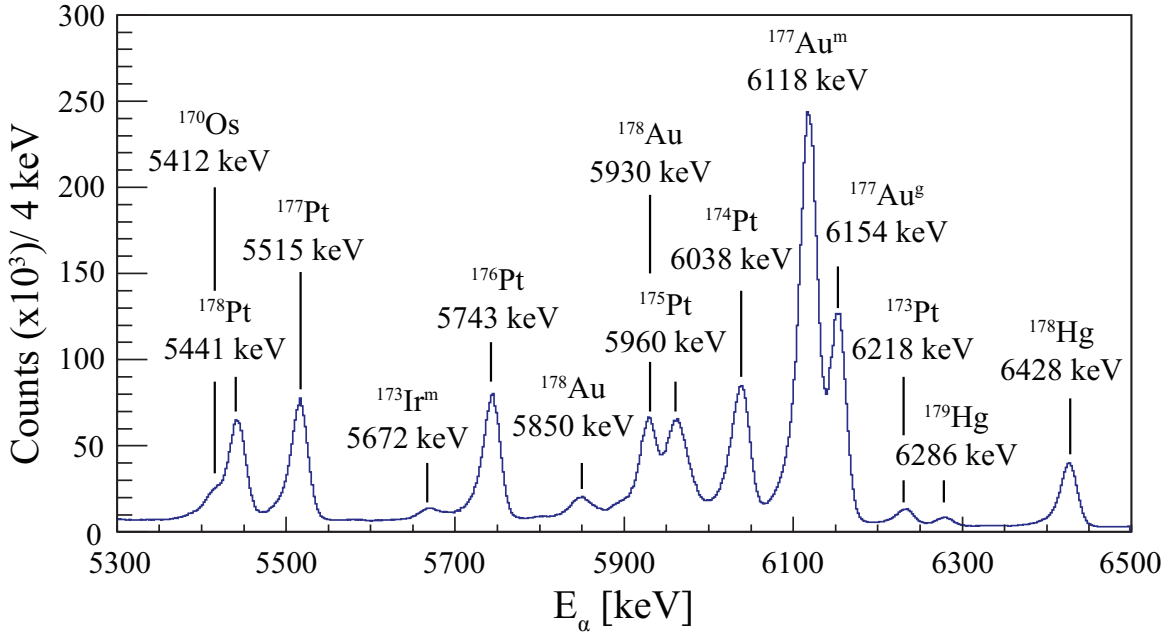

Figure 3.17: Energy spectrum of α particles (vetoed by MWPC) from the reaction $^{92}_{42}\mathrm{Mo} + ^{88}_{38}\mathrm{Sr}$, measured in the DSSD detector, from the Experiment JR115.

recoil and parent alpha (α_1) together with $\Delta t(\alpha_2 - \alpha_1) \leq 9$ s between the parent alpha (α_1) and child alpha (α_2) were used to sort the data into the ER-α_1-α_2 correlation matrix, shown in Fig. 3.18. The list of identified isotopes, including their α-decay energies and half-lives is presented in Table 3.4.

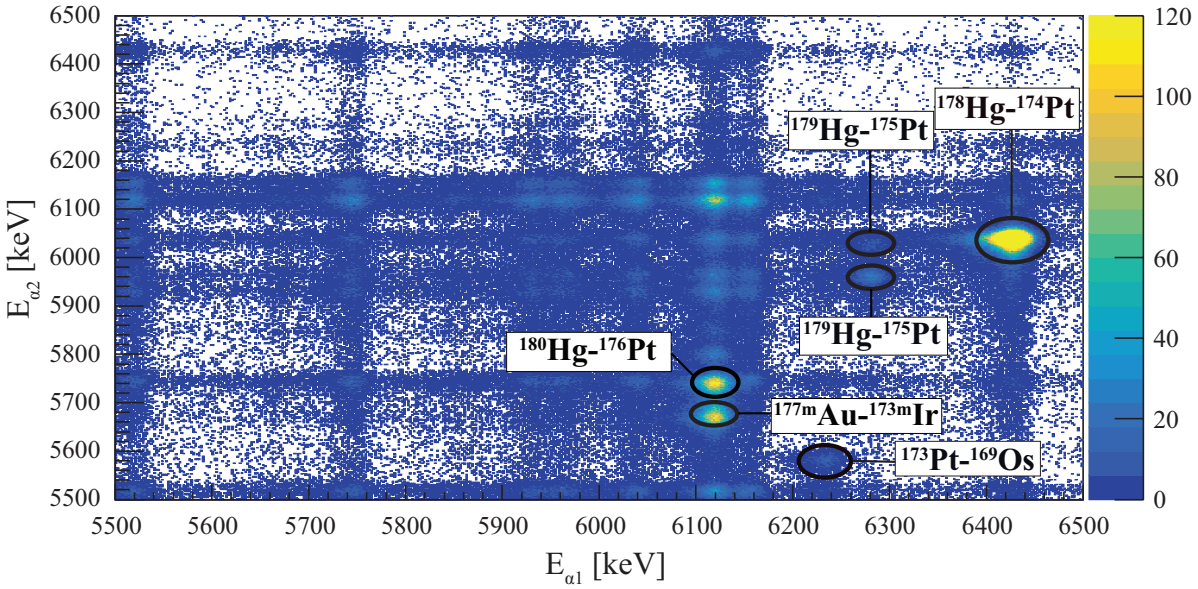

Figure 3.18: The ER-α_1-α_2 matrix of correlated α-decay events, measured with the DSSD detector. Correlation times: $\Delta t(\alpha_1 - \mathrm{ER}) \leq 4$ s between the recoil and parent alpha, together with $\Delta t(\alpha_2 - \alpha_1) \leq 9$ s between α_1 and α_2 was used. Black ellipses denote true correlations. Experiment JR115.

Parent nucleus	$E_{\alpha 1}^{exp}$ [keV]	$E_{\alpha 1}^{tab}$ [keV]	$T_{1/2}$ [s]	Child nucleus	$E_{\alpha 2}^{exp}$ [keV]	$E_{\alpha 2}^{tab}$ [keV]	$T_{1/2}$ [s]
^{173}Pt	6233(6)	6211(6)	0.382(2)	^{169}Os	5584(5)	5577(8)	3.4(2)
^{177}Au	6119(5)	6110(10)	1.18(7)	^{173m}Ir	5672(4)	5670(6)	2.20(5)
^{178}Hg	6427(5)	6430(6)	0.27(3)	^{174}Pt	6040(4)	6038(4)	0.90(1)
^{179}Hg	6282 (6)	6288(5)	1.07(5)	^{175}Pt	6030(7)	6038(10)	2.52(8)
^{179}Hg	6282 (6)	6288(5)	1.07(5)	^{175}Pt	5961(5)	5960(3)	2.52(8)

Table 3.4: Identified parent alpha (α_1) - child alpha (α_2) correlations in the ER-α_1-α_2 matrix from the experiment JR115, shown in Fig. 3.18. The 2^{nd} and 6^{th} columns represent experimental α-decay energies, the 3^{rd} and 7^{th} columns show tabulated α-decay energies and 4^{th} and 8^{th} columns represent values of half-lives for parent and child nuclei, respectively. Tabulated energies and half-lives were adopted from [59].

In Fig. 3.18, a suspicious correlation between 6119(5) keV and 5741(6) keV α decays was observed. The first indication is the α decay of ^{180}Hg correlated with ^{176}Pt α decay. Tabulated α-decay energies of these two isotopes are 6120(5) keV and 5753(3) keV [59], respectively. However, in the $^{88}_{38}$Sr + $^{92}_{42}$Mo fusion-evaporation reaction, the ^{180}Hg isotope is a compound nucleus in a highly excited state. The first process of de-excitation is the evaporation of particles, which occurs in $\approx 10^{-19}$s. The time necessary for the nuclei to reach the DSSD detector is $\approx$ 300 - 500 ns. However, the enrichment of the $^{92}_{42}$Mo target was 98 %, hence some portion of heavier Mo isotopes could be present in the target as well. This could in turn cause detection of the ^{180}Hg nuclei in the focal plane of RITU. Another explanation are random correlations of the dominant evaporation channel ^{177}Au being correlated with the α decay of 2p2n evaporation channel producing ^{176}Pt nuclei. Based on the arguments presented above, the correlation of 6119(5) keV and 5741(6) keV α decays was assigned as ^{180}Hg - ^{176}Pt.

3.4.1 Fine structure in ^{177}Au

Similarly to Sec. 3.2, also here the measured data were first sorted into the α-γ matrix using the search time Δt (α-ER) $\leq$ 4 s and Δt(γ-α) $\leq$ 200 ns. Since no condition for α decay time was present, only α particles which were detected within 4 s after the recoil implantation in the DSSD detector were taken into account. Due to many evaporation channels open, the

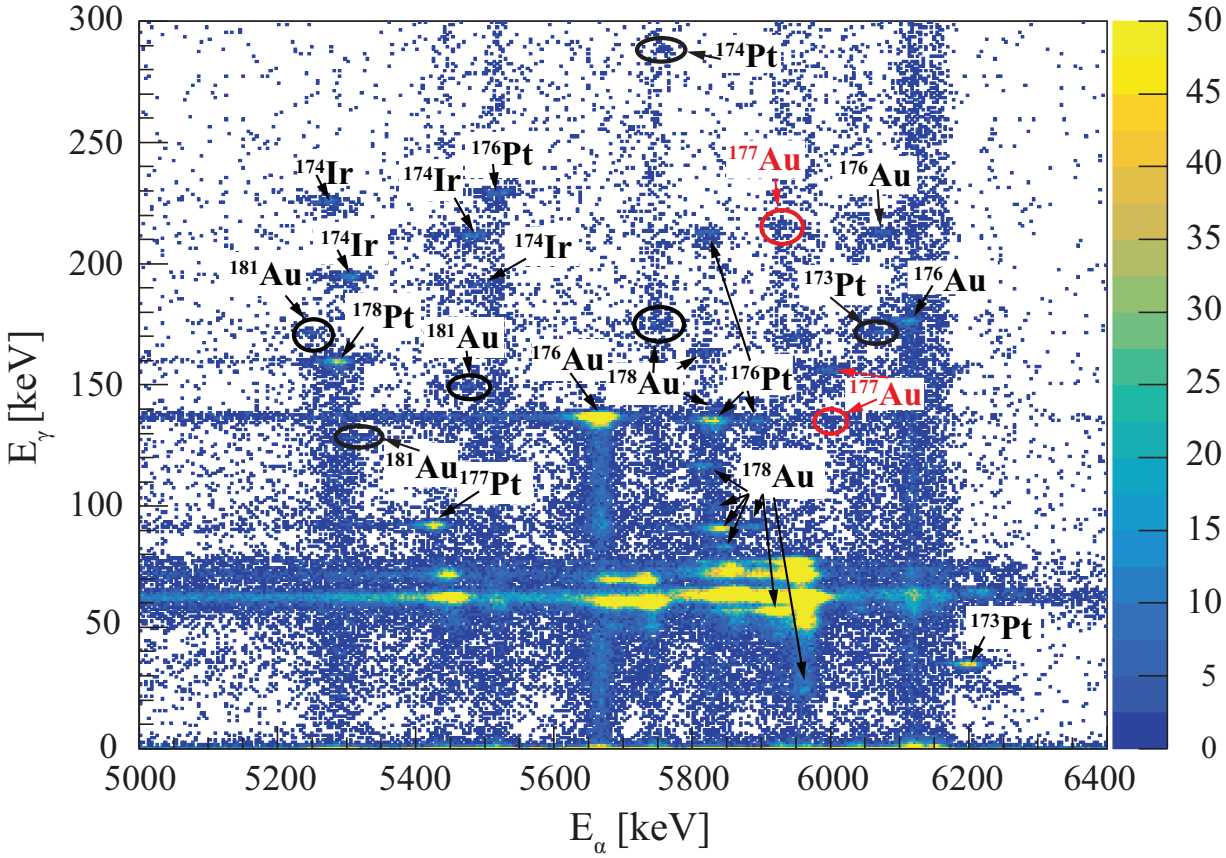

Figure 3.19: The α-γ coincidence matrix, measured with the DSSD detector and focal plane HPGe Clover and planar detectors. The time windows used for coincidence search are $\Delta t(\gamma - \alpha) = 200$ ns, together with $\Delta t(\alpha - \mathrm{ER}) \leq 4$ s for correlated α decays. Due to the presence of Re, Os, Ir and Pt x rays, coincidences with $E_\gamma = 60$ - 75 keV are produced. The coincidences marked in black are further discussed in Sec. 3.4.3

α-γ coincidence matrix shown in Fig. 3.19 is plentiful in number of observed coincidences. In order to lower the contamination of random coincidences, four background matrices were created and subsequently subracted from the original matrix. Search times used in these background matrices were:

- Δt (ER-α) ≤ 4 s and Δt(γ-α) ≤ 200 ns,
- Δt (α-ER) ≤ 4 s and Δt(α-γ) ≤ 200 ns,
- 6 s $\leq \Delta$t (α-ER) ≤ 10 s and Δt(γ-α) ≤ 200 ns,
- Δt (α-ER) ≤ 4 s and 400 ns $\leq \Delta$t(γ-α) ≤ 600 ns.

The final background subtracted matrix is shown in Fig. 3.19. Two newly observed α decays at 5998(5) keV and 5932(6) keV were attributed to fine structure in the α decay of ^{177}Au (red

labels in Fig. 3.19), based on the analysis of α-γ coincidences (see Fig. 3.19) and ER-α_1-α_2 correlations (shown in Fig. 3.18).

The 5998(5) keV α decay is seen in coincidence with the 156.1 keV γ ray, see Fig. 3.19. The total Q value calculated as $Q_{\alpha,tot} = Q_\alpha(5998) + E_\gamma(156) = 6295(5)$ keV agrees with the $Q_\alpha(6156) = 6298$ keV for the ^{177}Au^g α decay. Child α_2 decays correlated with the $E_{\alpha_1} = 5998$ keV in the ER-α_1-α_2 3.18 are shown in Fig. 3.20. A strong correlation with the 5415(4) keV α decays can be seen. This energy is in good agreement with the ^{173}Ir^g α decay with E_α = 5418(4) keV [93]. The ^{173}Ir^g α decay was attributed to depopulate the (1/2$^+$, 3/2$^+$) ground state. The remaining correlations seen in Fig. 3.20, are present due to long search times used the ER-α_1-α_2 correlation matrix. A small peak marked as ^{173}Ir^m is discussed further in the text. This α decay branch was already tentatively assigned in [86], where a 6000(20) keV α decay was observed. Unfortunately, no γ rays in coincidence with the 6000(20) keV α decay were reported in [86]. To further consolidate the assignment of 156.1 keV γ ray to the 5998 keV α decay, a half-life of the 5998 keV α decay was measured. The logarithmic time distribution of the 5998 keV α decays from Fig. 3.18 is presented in Fig. 3.21. In order to separate the decays of interest from other correlations, 5998 keV α decays in coincidence with 156.1 keV γ rays in Fig. 3.19 were used. The data points were fitted using the K. H. Schmidt method [94]. This procedure gives $T_{1/2}(156) = 1.60(21)$ s, which agrees with the 1.501(20) s g. s. $\rightarrow$ g. s. decay of ^{177}Au. This establishes a new α decay branch of ^{177}Au, populating the 156.1 keV excited state in ^{173}Ir as depicted in the decay scheme shown in Fig. 3.22.

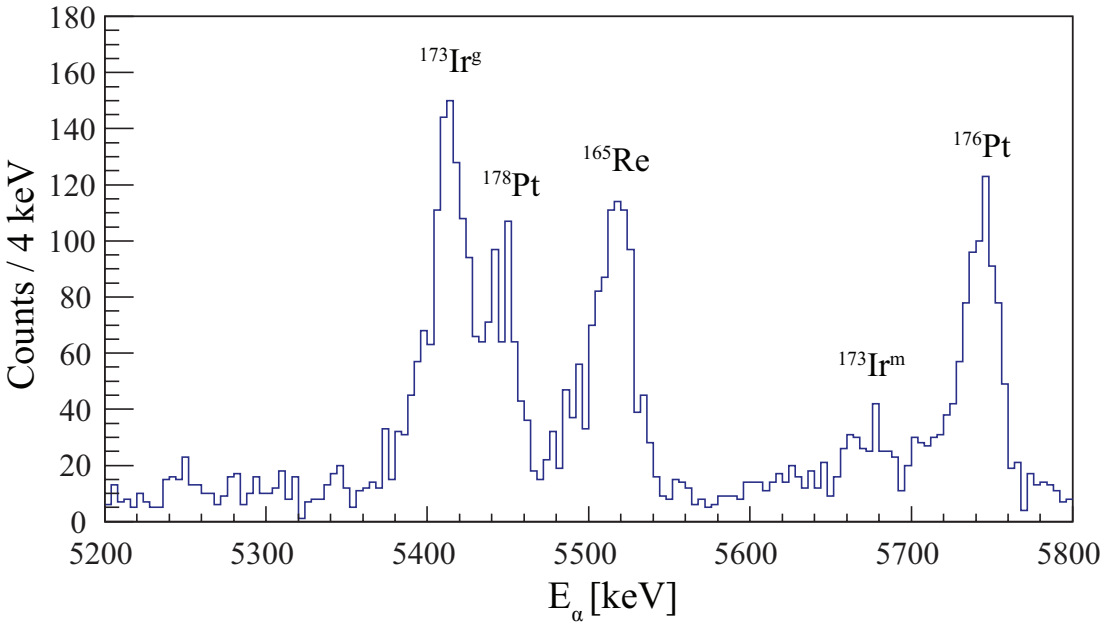

Figure 3.20: Child α_2 decays correlated with the 5998 keV parent α_1 decays. The same search times were used as in the ER-α_1-α_2 correlation matrix, see Fig. 3.18. Random correlation with ^{165}Re, ^{176}Pt and ^{178}Pt are present due to long search times.

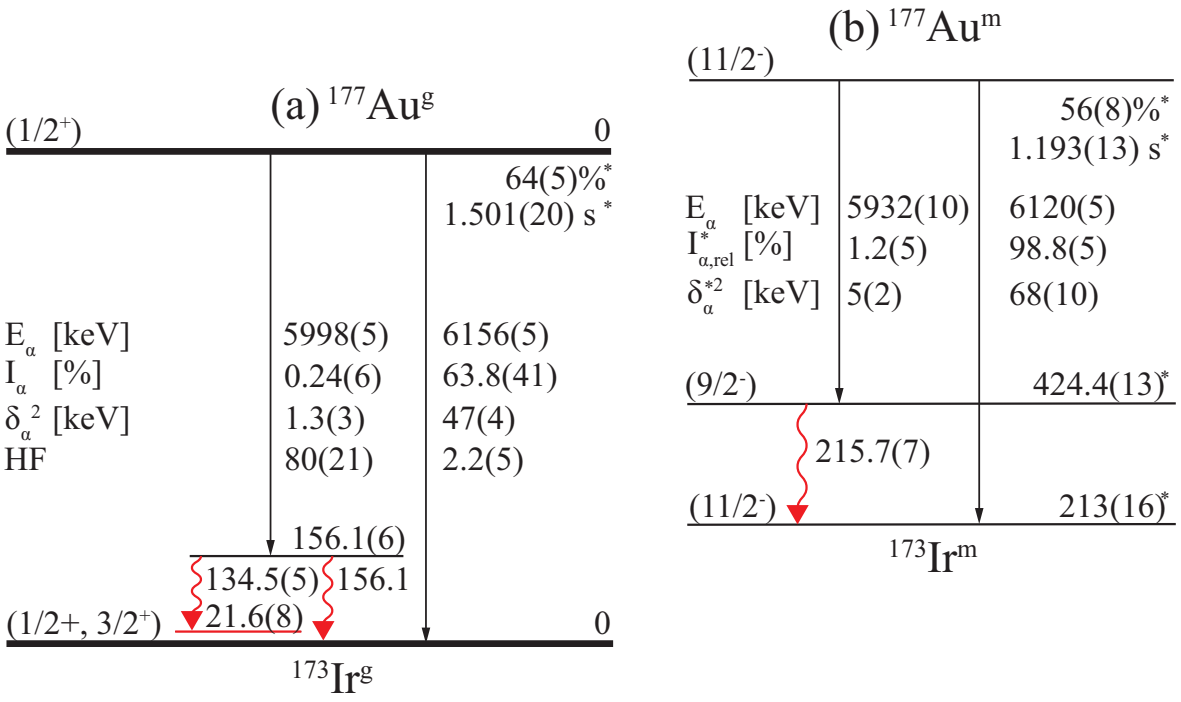

Figure 3.22: The α-decay scheme of ^{177}Au deduced in the present work. Newly observed transitions are indicated in red colour. Values marked by an asterisk are adopted from [86].

Alpha-decay events with an energy of 5998(5) keV were also found to be in coincidence with the 134.5 keV γ rays, see Fig. 3.19. The total Q value of this coincidence equals to

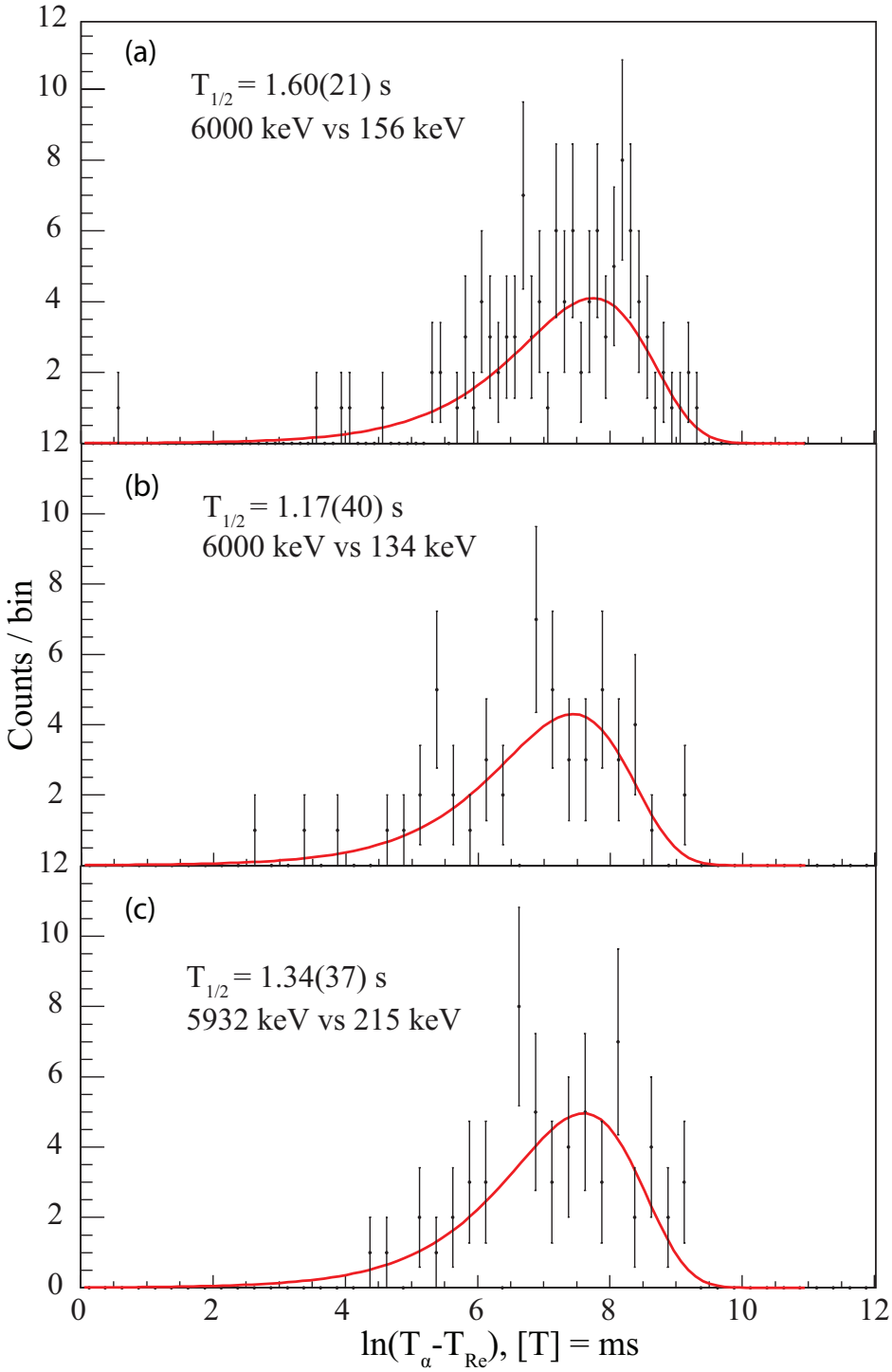

Figure 3.21: Time distributions of ^{177}Au α decays populating the (a) 156.1 keV excited state with emitted 156.1 keV γ ray, (b) 156.1 keV excited state with emitted 134.5 k γ ray and (c) 424.4 keV excited state with emitted 215.1 keV γ ray in ^{173}Ir. Search times $\Delta t(\alpha$ - ER) < 4 s and $\Delta t(\gamma$ - $\alpha)$ < 200 ns were used along with red 2-dimensional gates used in 3.19. The time differences on the x-axis are plotted taking the natural logarithm of the observed time difference $\Delta t(\alpha - \mathrm{ER})$ (in ms units) [94].

$Q_{\alpha,tot} = Q_\alpha$ (5998) + E_γ (134) = 6271(7) keV. The difference between the corresponding $Q_{\alpha,tot} = Q_\alpha$ (5998) + E_γ (134) = 6271(7) keV and $Q_\alpha(6156) = 6298$ keV of the g. s. $\rightarrow$ g. s. Q value of ^{177}Au^g is 24(8) keV. This observation suggests a second de-excitation path of the 156.1 keV excited state in ^{173}Ir, where the 134.5 keV transition is placed as a crossover transition feeding the excited state at an energy of 24(8) keV. It should be noted here that the calculation of the aforementioned $Q_{\alpha,tot}$ ignored the contribution from conversion and Auger electrons due to α - electron summing effect. This effect increases the α-decay energy by 20.6(22) keV. However, the increase is not observed in the present data. A possible explanation is that the 24(8) keV excitated state de-excites via emission of isomeric, i.e. delayed γ ray. A different approach suggests weak internal conversion of the 21.6 keV transition. Since the smallest conversion coefficient for the 21.6 keV transition is $\alpha = 4$ [33], this option can be ruled out. Unfortunately, no γ rays emitted from this excited state were observed.

Another possible configuration would place the 5998 keV α decay as a part of the ^{177}Au^m decay path. In this scenario, the 5998 keV decay populates a new 343.3 keV excited state in ^{173}Ir. This places the 134.5 keV γ ray as a crossover transition to the 213(16) keV excited state in ^{173}Ir. The Q value changes to Q_α(5998) + E$_\gamma$(134) = 6089(8) keV which is in a good agreement with Q_α(6125) = 6085(5) keV. In the spectrum of child α decays, see Fig. 3.20, a small peak labelled as ^{173}Ir^m is present. The 134.5 keV coincidence is significantly weaker compared to the 156.1 keV coincidence, see Fig. 3.19. This may correspond to the presence of the significantly weaker ^{173}Ir^m α decay peak in Fig. 3.20. However, the ^{173}Ir^m α decay peak could also originate from random correlations. The half-life of ^{173}Ir^m is 2.16(4) s with a branching ratio of $b_\alpha = 11.0(21)$ % [93]. In addition to long search times, the ^{177}Au was the dominant reaction channel. Therefore, the spectra of correlated α_2 decays can be contaminated with the child decays of ^{177}Au. The number of 5998 keV α decays coincident with 134.5 keV γ rays in Fig. 3.19 is 37. Unfortunatelly, a spectrum of child α decays correlated with the 5998 keV α decays also in coincidence with the 134.5 keV γ rays could not be produced. An additional search time $\Delta t(\alpha_2 - \alpha_1) \leq 9$ s reduced the statistics of the correlated child decays and no usable spectra could be produced. Lastly, the half-life was measured in similar fashion to the previous α decay, with resulting value T$_{1/2}$(5998) = 1.17(40) s, see Fig. 3.21. This value is in better agreement with T$_{1/2}$(^{177}Au^m) = 1.193(13) s than T$_{1/2}$(^{177}Au^g) = 1.501(20) s. The nature of the 134.5 keV transition is further discussed below in Sec. 3.4.2.1

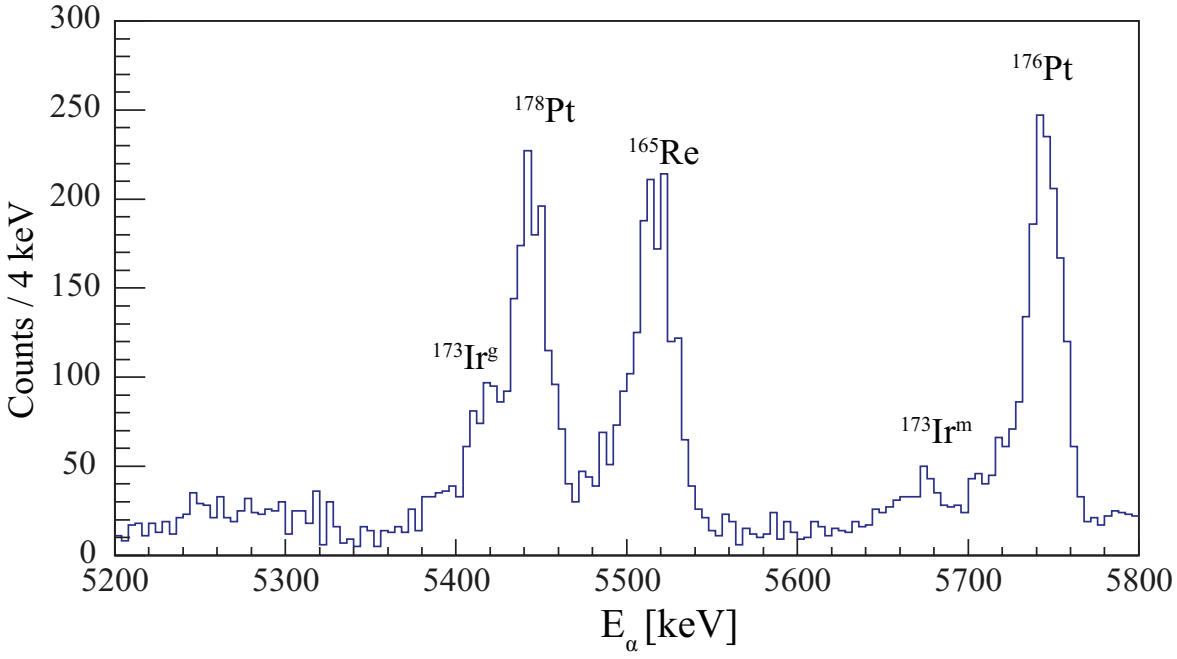

Figure 3.23: Child α_2 decays correlated with the 5932 keV parent α_1 decays. The same search times were used as in the ER-α_1-α_2 3.18. Random correlation with ^{165}Re, ^{176}Pt and ^{178}Pt are present due to long search times.

The last coincidence attributed to the ^{177}Au decay belongs to the 5932(6) keV α decay coincident with 215 keV γ rays. The α-particle energy is a known α decay of ^{177}Au^{m}. It proceeds from the 11/2^{-} excited state at 181.9(4) keV in ^{177}Au [95] and leads to the (9/2^{-}) excited state at an energy of 424.4(13) keV in ^{173}Ir [86]. Until now, no transitions were observed to depopulate the 424.4(13) keV excited state in ^{173}Ir. The 215 keV γ ray seen in coincidence with this α decay suggest the population of 424.4(13) keV excited state with subsequent emission of 215.1 keV γ ray. Since the 213(16) keV excited state in ^{173}Ir is a known 2.20(5) s isomer, contribution from the internal conversion of the 213 keV transition is negligible and not observed in the discussed matrix. The total Q value for this decay is 6091(6) keV, and it agrees with the Q_α(6125) = 6085(5) keV. In Fig. 3.23, α-decay events correlated with the 5932 keV alphas are shown. Correlation times required for the events to be put in the spectrum were $\Delta t(\alpha_1 - \text{ER}) \leq 4$ s and $\Delta t(\alpha_2 - \alpha_1) \leq 9$ s. Here, a weak correlation with the 5675(6) keV alphas can be seen. This energy agrees with 5672(3) keV α decay of ^{173}Ir^{m}. Note that random-correlation peaks are located at the same energies as in Fig. 3.20. Secondly, areas under the peaks corresponding to random correlations are greater than in Fig. 3.20. This arises from the fact that the 5932 keV energy gate is part of the ^{178}Au decay peak, while the 5998 keV energy gate is not part of any peak correspond-

ing to dominant evaporation channel, see Fig. 3.17. Moreover, analysis of the decay-time distributions results in $T_{1/2}(215) = 1.34(37)$ s, which agrees within the error bars with the $T_{1/2}(^{177}Au^{m}) = 1.193(13)$ s [86]. Therefore, the 215.7 keV γ-ray coincidence seen in 3.19 fits well as a crossover transition between the 424.4 keV and 213 keV levels. Based on the arguments presented above this it was also placed in the decay scheme in Fig. 3.22.

3.4.2 Discussion - ^{177}Au

The α decay characteristics along with the multipolarity of the observed γ-ray transitions are discussed in this section. Starting with multipolarity, the same analysis as in the Sec. 3.2 was performed for the 156 keV γ ray transition. The analysis results in $\alpha_K(156) = 3.3(15)$. Unfortunately, this result is exaggerated, because the number of Ir K_β x rays used in the calculation contains also Ir K_β x rays emitted during the 215.1 keV transition. Moreover, the possible 134.5 keV transition can increase the number of observed Ir K_β x rays as well. Therefore, the real conversion coefficient will be smaller than calculated. Since the 156 keV γ-ray transition is seen as prompt, its multipolarities are limited to $E1$, $M1$ or $E2$. Theoretical values of aforementioned multipolarities for the 156.1 keV transition are $\alpha_K(E1) = 0.105(11)$, $\alpha_K(M1) = 1.42(17)$, $\alpha_K(E2) = 0.32(4)$ [33]. Therefore, the suggested multipolarity is ($M1$+$E2$). The α decay characteristics for the α decay populating the 156 keV excited state in ^{173}Ir were calculated using only the 156 keV transition, due to tentative nature of 134.5 keV. Here, the method used in the Sec. 3.2 was used to calculate the reduced decay width $\delta^2 = 1.3(3)$ keV and hindrance factor HF = 80(21). These values indicate a hindered decay. Therefore, the spin of the initial state should differ from the final state. This supports the lower order multipolarity character for the 156 keV transition. Regarding the g. s. $\rightarrow$ g. s. α decay of ^{177}Au, the calculated values are $\delta^2 = 47(4)$ keV and HF = 2.2(5). These indicate unhindered decay. It means that the wave functions of the initial and final state should have large overlap. No additional information about α decay characteristics or multipolarity of the 215.1 keV γ-ray transition could be extracted from the experimental data considering the mixing of Ir K_β x rays from 215.1 keV and 156.1 keV transitions. Due to the low statistics of the 215.1 keV coincidences in Fig. 3.19, similar estimation as for the 156.1 keV γ-ray transition could not be made. Additionally, the 5932 keV α decay was previously studied in [86].

3.4.2.1 The 5998 keV α decay coincidence with 134.5 keV γ ray

The 134.5 keV γ-ray transition coincident with the 5998 keV α decay was compared with neighbouring ^{173}Ir nuclei. Recently, the α decay of ^{179}Au was studied by [86]. Here, the 5718(10) keV α decay populating the 131.9(4) keV excited state was observed. Two different γ rays de-exciting the 131.9(4) keV excited state were observed. One feeds the ground state in ^{173}Ir, while the other is a 105.3 keV transition from the 131.9 keV excited state to the 26.1 keV excited state in ^{173}Ir. The 131.9 keV transition was assigned $M1$ multipolarity, while the 105.3 keV transition was characterized by ($M1/E2$) multipolarity. Moreover, the reduced width and hindrance factor of the α decay populating the 131.9 keV excited state in ^{175}Ir were calculated as δ^2 = 2.1(7) keV and HF = 27(9). The relative branching ratio for the 5718 keV α decay was measured as $I_{\alpha,rel}$(5718) = 0.97(31) %. However, in the ^{175}Ir, the 26.1(4) keV excited state was observed to emit the 26.1 keV γ ray with the $M1$ character [86]. Moreover, in [96] an experimental reduced transition probability is given as $B(M1)$ = 3.3 x10$^{(-6)}$ W. u.

Additionally, a 25.7 keV excited state was observed in the ^{177}Au isotope. It was attributed spin and parity of (3/2$^+$). It was identified from energy differences of parallel 264.5 keV and 290.2 keV γ-ray transitions which were assigned as members of ground-state band [95]. The 25.7 keV excited state in ^{177}Au could be an isomeric state [97]. This correspond with the idea that the 21.6 keV excited state in ^{173}Ir populated by the 134.5 keV transition is also isomeric. As mentioned in Sec. 3.4.1, the energy of α decays in coincidence with 134.5 keV γ rays should be shifted to higher energies due to the conversion and Auger electron summing. However, no such shift in the α decay energy was observed. A possible explanation for this is that the 21.6 keV transition depopulates an isomeric state. In such case the conversion and Auger electrons would be emitted later after the α decay and therefore no summing effect would occur. To verify the possibility of 21.6 keV being isomeric a theoretical half-life of the 21.6 keV excited state was calculated. For this a reduced transition probability in the same range as $B(M1)$ = 3.3 x10$^{(-6)}$ W. u. taken from the neighboring ^{175}Ir [96] isotope was used. The result of the calculated half-life is $\approx$ 670(50) ns. This supports the argument that the 21.6 keV level in ^{173}Ir is an excited isomeric state.

The similarities with the neighbouring nuclei puts the possibility of the 134.5 keV γ ray being a crossover transition between a 343 keV excited state and 213 keV isomeric state in disadvantage. The measured half-life $T_{1/2}$ = 1.17(40) s fits better to the $T_{1/2}$ = 1.193(13) s

which belongs to the $^{177}Au^{m}$ decay. Simulations of the 134 keV transition de-exciting the 156 keV, 343 keV excited state and the measured data is shown in Fig. 3.24. There, the 21.6 keV was simulated as prompt transition. Note, the slight shift of the 134 keV coincidence in (a). The simulation supports the 134 keV γ-ray transition feeding the 213 keV excited state in ^{173}Ir. However, due to the systematics of neighbouring nuclei, the 134.5 keV transition is tentatively assigned to de-excite from the 156.1 keV excited state in ^{173}Ir.

3.4.3 Other α-γ coincidences

This section is dedicated to the investigation of remaining prompt α-γ coincidences in Fig. 3.19. The analysis was performed in similar fashion as in the Sec. 3.2.3. All of the identified coincidences are listed in Table 3.5. The coincidence between 6202(4) keV α decay and 35.1(5) keV γ ray was attributed to the ^{173}Pt α decay. First, the time difference between the recoil implantation and subsequent α decay was plotted in Fig. 3.25. The measured half-life is 326(57) ms. This is within the error bars of the $T_{1/2}(^{173}Pt) = 382(2)$ [98]. The Q value analysis results in $Q_{\alpha,tot} = Q_{\alpha}(6202) + E_{\gamma}(35) = 6384(4)$ keV. This value matches well with Q_{α} = 6350(50) keV of ^{173}Pt g. s. $\rightarrow$ g. s. α decay. When the known level scheme of ^{169}Os is consulted [98], this 35.1 keV γ ray could be a crossover transition between the 171.2 keV and 136.2 keV excited states. When the energy of conversion and Auger electrons is subtracted from the measured E_{α} = 6202 keV, the Q_{α} result in 6233(5) keV. The energy difference between this value and Q_{α} = 6350(50) keV is 117(51) keV. This challenge the possibility of the 35 keV γ ray to depopulate the 171.2 keV excited state in ^{169}Os. Since, no additional information could be extracted from the γ-γ analysis, the 35 keV γ ray was tentatively assigned as the transition depopulating the 35 keV excited state in ^{169}Os.

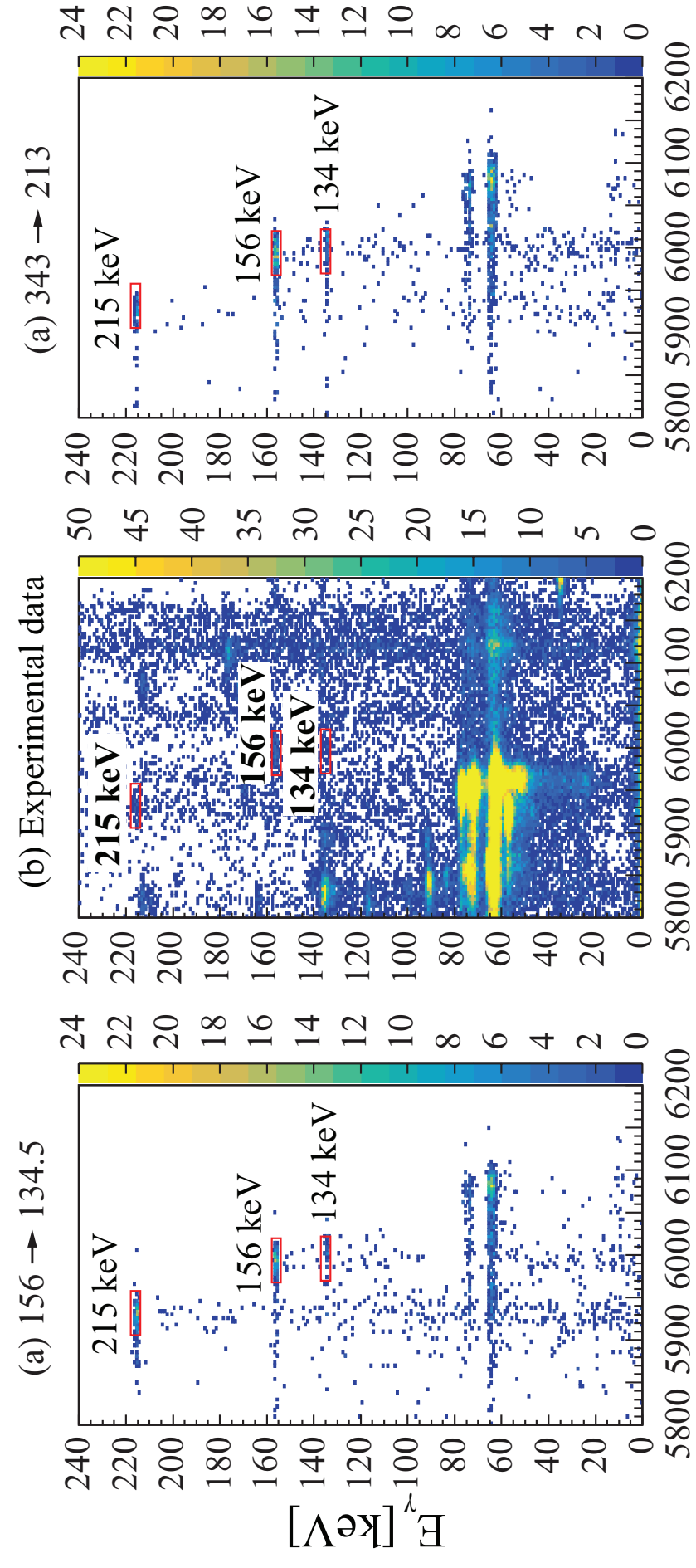

Figure 3.24: The comparison of simulated decay of ^{177}Au with (a) 134.5 keV γ ray as crossover transition between 156 keV and 21.6 keV excited states in ^{173}Ir, (b) experimental data and (c) 134.5 keV γ ray depopulating the 343 keV excited state in ^{173}Ir.

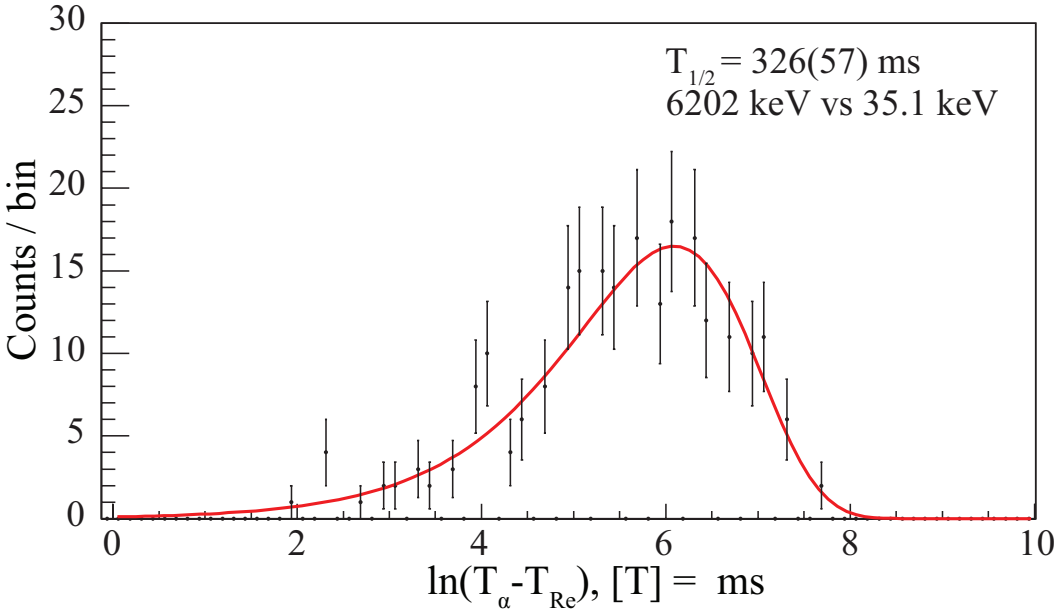

Figure 3.25: Logarithmic time distribution of α decays coincident with 35.1 keV γ ray, see Fig. 3.19. The time differences on the x-axis are plotted taking the natural logarithm of the observed time difference $\Delta t(\alpha - \mathrm{ER})$ (in ms units) [94].

The coincidence between 5952(6) keV α decay and 170 keV γ ray was not successfully identified. The half-life analysis, see Fig. 3.26, results in $T_{1/2} = 0.55(16)$ s. This value matches with 0.57(3) s, witch belongs to the g. s. $\rightarrow$ g. s α decay of ^{169}Ir. However, the Q-value analysis results in $Q_{\alpha,tot}$ = Q_α(5952) + E_γ(170) = 6266(5) keV, which is different from $Q_\alpha(^{169}\mathrm{Ir}) = 6141(4)$ keV. There is a known second α-decay branch in ^{169}Ir. This $(11/2^-)$ $\rightarrow$ $(11/2^-)$ α-decay branch depopulates the 153(24) keV excited state in ^{169}Ir and it feeds the 48(26) keV excited state in ^{165}Re. The value Q_α = 6268(14) keV matches well with the Q_α value calculated for the 5952(6) keV α decay. However, the significantly shorter half-life $T_{1/2}(6119) = 0.280$ s contradicts our experimental findings. In the range of $160 < A < 180$ exists one additional candidate with half-life within the error bars of the measured value. It is the α decay of ^{173}Pt with $T_{1/2} = 382(2)$ ms [98]. This Pt isotope has four known α-decay branches. Two of them are visible in the prompt α-γ matrix, see Fig. 3.19. The Q-value analysis results in $Q_{\alpha,tot} = Q_\alpha(5952) + E_\gamma\ 170 = 6263$ keV, while the Q value of ^{173}Pt is 6350(50) keV. The difference of these two values is 87(50) keV. Within the error bars the 5952 keV α decay could populate the 280(1) + x keV excited state in ^{169}Os with 170 keV γ-ray transition populating the 101(7) keV excited state. Nevertheless, the 101(7) keV would

have to be a isomeric state due to non-observation of summation of 5952 keV α particle energy with the conversion and Auger electrons from the 101 keV transition. This is indirectly supported by the fact that there is no known γ-ray transition depopulating the 101(7) keV excited state in ^{173}Pt. The analysis of the ER-α_1-α_2 matrix did not lead to any useful informations. Since it was not possible to extract additional informations, the assignment of the coincidence between $E_\alpha = 5952$ keV and 170 keV γ ray was not concluded.

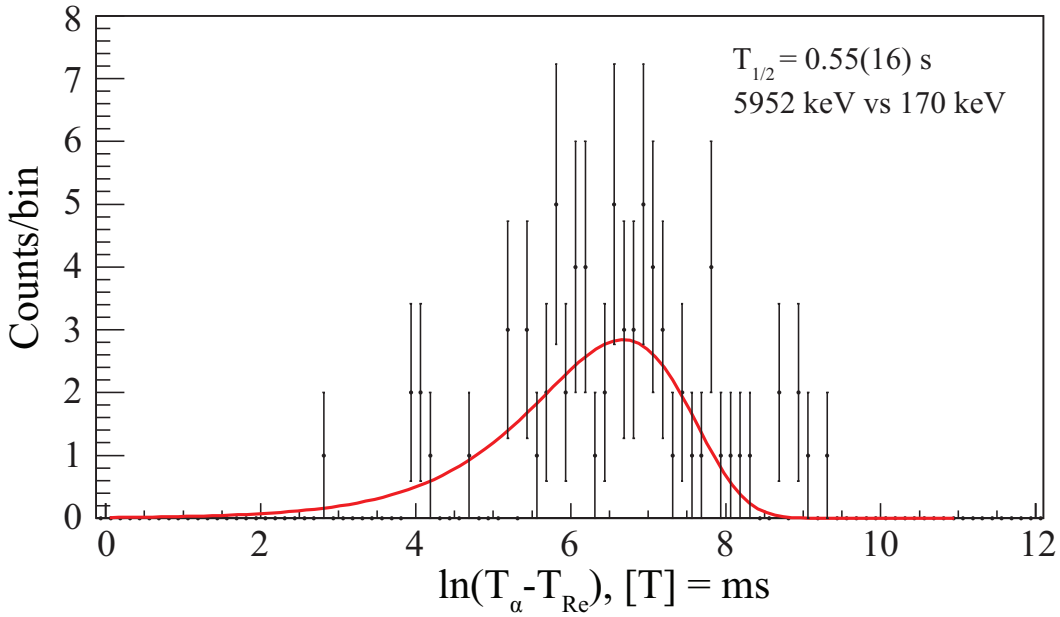

Figure 3.26: Time distributions of α decays coincident with 170 keV γ ray, see Fig. 3.19. The time differences on the x-axis are plotted taking the natural logarithm of the observed time difference $\Delta t(\alpha - \mathrm{ER})$ (in ms units) [94].

In the final analysis, the delayed α-γ coincindence matrix was constructed, see Fig. 3.27. Search times 200 ns$\leq \Delta t(\gamma - \alpha) \leq$ 700 μs together with previous $\Delta t(\alpha - \mathrm{ER}) \leq 4$ s were used. The investigation of the delayed α-γ coincidences was performed in similar fashion as in Sec. 3.2.3. Here, the same coincidence between $E_\alpha = 5997$ keV and $E_\gamma = 147$ keV can be seen. To verify the ^{181}Hg origin, the half-life of the 147 keV isomeric state was measured. The time distribution between the 5997 keV α decays and 147 keV γ rays is plotted in Fig. 3.28. The resulting half-life of this isomeric state was measured as $T_{1/2}(147\ \mathrm{keV}) = 2.55(13)$ μs. This agrees with the previous value 2.2(3) μs. Even though the compound nuclei was ^{180}Hg, the ^{181}Hg nuclei could be produced due to small amount of impurities in the target (98 % enrichment).

The two remaining coincidences in the α-γ coincindence matrix shown in Fig. 3.27

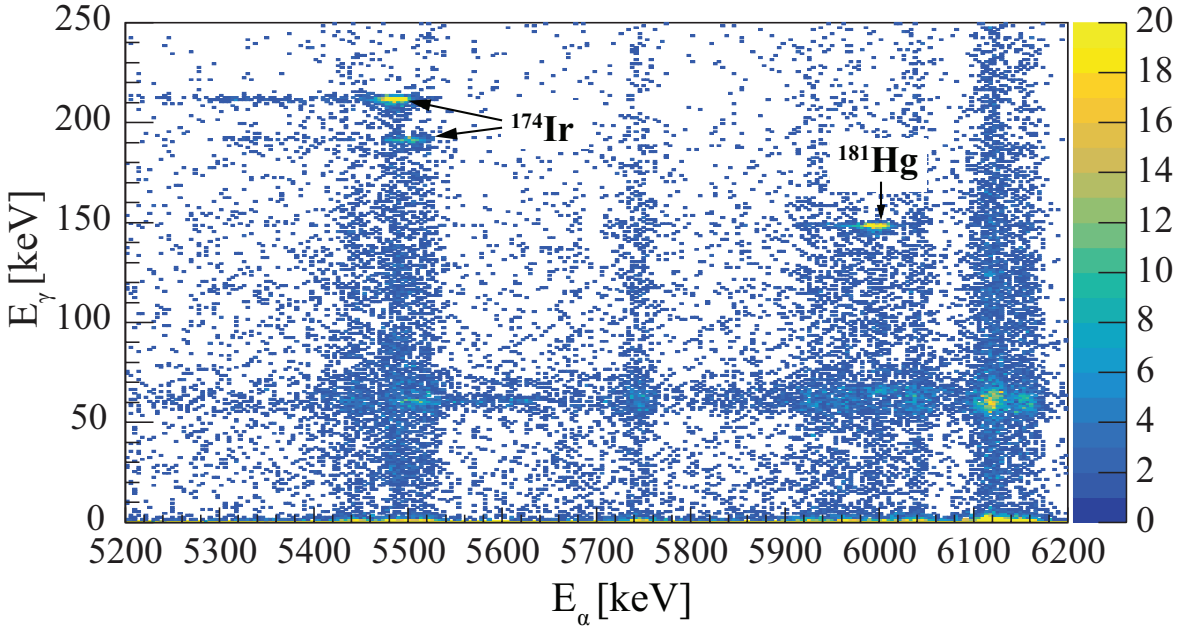

Figure 3.27: The α-γ coincidence matrix, measured with the DSSD detector and focal plane HPGe Clover and planar detectors. Time windows used for coincidence search are 200 ns$\leq \Delta t(\gamma - \alpha) \leq 7\,\mu$s, together with $\Delta t(\alpha - \mathrm{ER}) \leq 4$ s for correlated α decays.

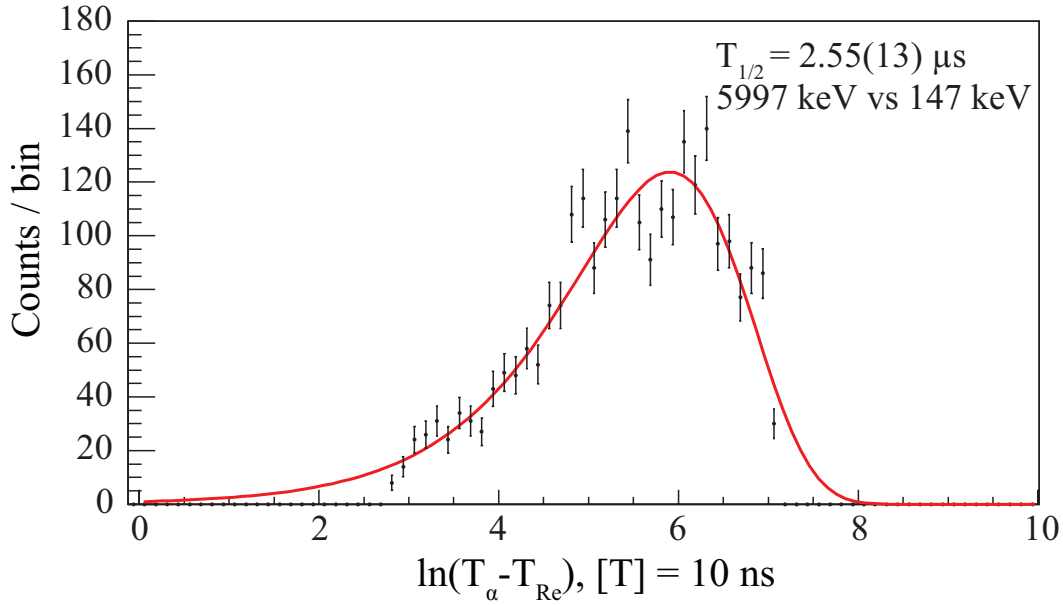

Figure 3.28: Logarithmic time distribution of α decays and coincident 147 keV γ ray, see Fig. 3.27. The time differences on the x-axis are plotted taking the natural logarithm of the observed time difference $\Delta t(\gamma - \alpha)$ (in 10 ns units) [94].

were identified already in the analysis of prompt α-γ coincindences, see Fig. 3.19. There, they were identified as α decay of ^{174}Ir^{m}. The E$_\alpha$ = 5488(6) keV is in coincidence with the 210.7(5) keV γ ray, while the E$_\alpha$ = 5499(6) keV is seen in coincidence with 190.6(6) keV. Previously in [102], the 5478(6) keV α decay was observed to populate the (7$^+$) excited state at 210.3(2) keV in ^{170}Re. Two γ rays de-exciting this state are known: 210.3(2) keV γ ray, populating the (5$^+$) ground state and 190.2(2) keV transition feeding the (6$^-$) excited state at 20.13(23) keV. The 190.6 keV γ ray is seen in our data with different α decay energy due to conversion and Auger electron summing. Although, the energies are within the error bars of the ones published in [102], there are some differences. Firstly, the 210.3 keV and 190.2 keV γ rays were assigned the $E1$ and $E2$ multipolarity character, respectively. The assignment was based on the intensity of α-delayed x rays. This does not seem to be supported in our data since both γ rays are seen in both prompt and delayed α-γ coincindence matrices. Possible explanation for their presence in both matrices is that the 210 keV excited state is an isomeric state with half-life around 150 ns. For this reason time distributions of both α-γ coincidences were constructed, see in Figs. 3.29 and 3.30.

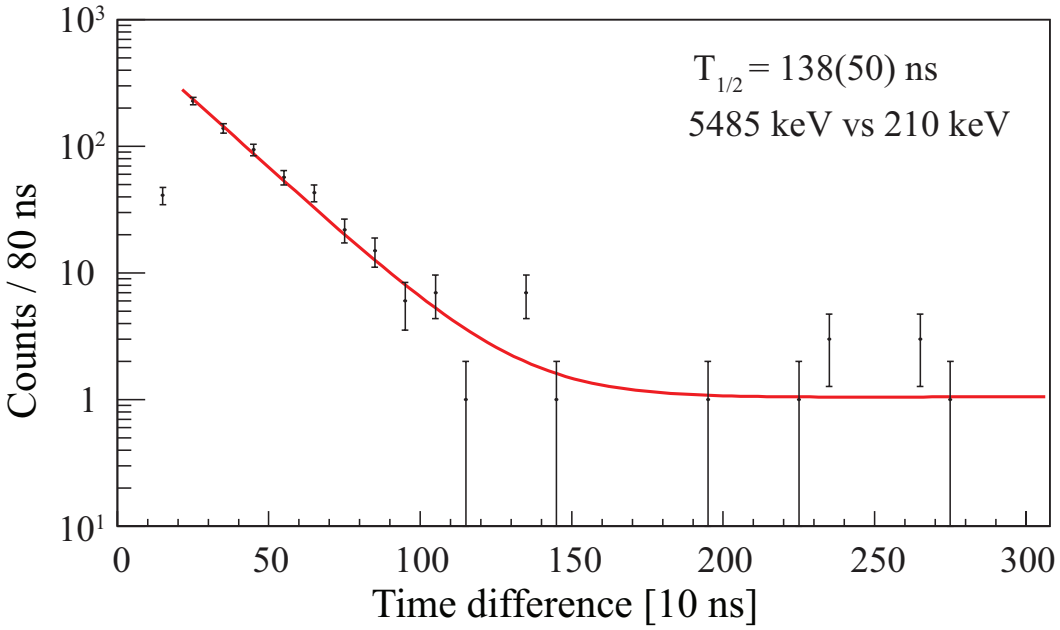

Figure 3.29: Distributions of time differences between (a) E$_\alpha$ = 5488 keV and coincident 210.7 keV γ ray. An exponential decay curve with a constant background was used to fit the data points and is shown as a solid red line. The measured half-life is 138(50) ns.

The search time between α decays measured by the DSSD detector and γ-rays detection in the planar detector was set to $\Delta t(\gamma - \alpha) \leq 200$ ns. Due to the fact that measured α-γ time differences are comparable with the used search time, both coincidences are present in

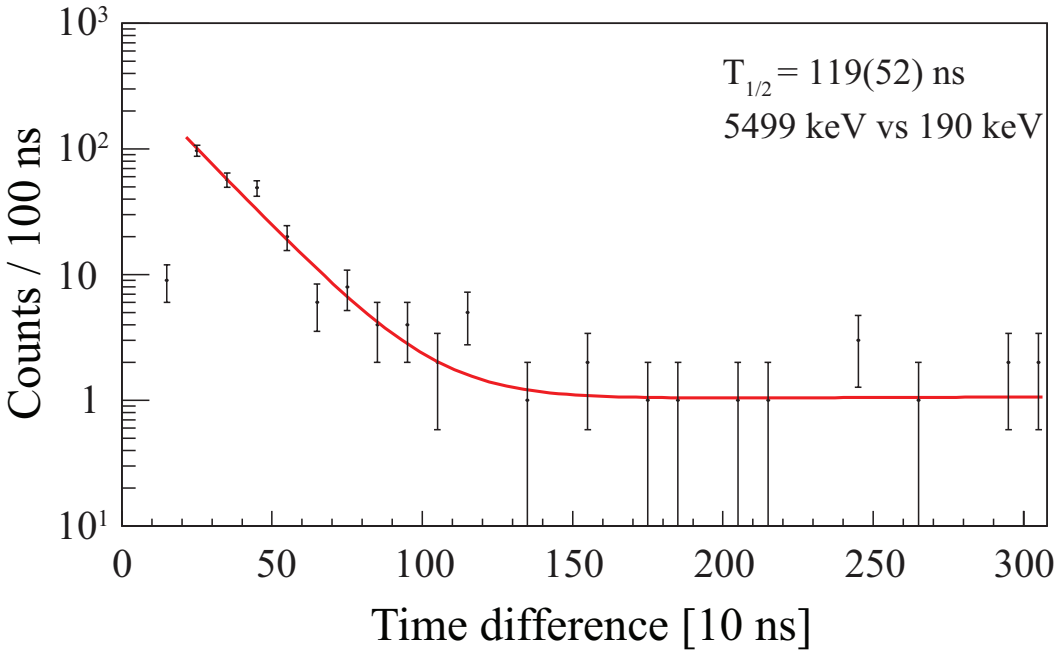

Figure 3.30: Time distribution of 5499 keV α decays and coincident 190.2 keV γ ray. An exponential decay curve with a constant background was used to fit the data points and is shown as a solid red line. The measured half-life is 119(52) ns.

the prompt and delayed α-γ coincidence matrices, see Figs. 3.5 and 3.19. Therefore, the 210 keV excited state in ^{170}Re is seen as isomeric in our data.

Parent nucleus	E_α^{exp} [keV]	E_α^{tab} [keV]	E_α^{tab} Reference	Child [keV]	E_γ [keV]	$Q_{\alpha,\,tot}$	$I_i \rightarrow I_f$
^{178}Au	5852(4)	5848(4)	[88]	^{174}Ir	83.8(6)	6070(4)	$(3^+, 4^+) \rightarrow (3, 4)$
^{178}Au	5842(4)	5840(10)	[88]	^{174}Ir	91.0(5)	6067(4)	$(3^+, 4^+) \rightarrow (3, 4)$
^{178}Au	5832(5)	5830(9)	[88]	^{174}Ir	99.9(9)	6066(5)	$(3^+, 4^+) \rightarrow (3, 4)$
^{178}Au	5816(4)	5812(4)	[88]	^{174}Ir	117.0(7)	6067(4)	$(3^+, 4^+) \rightarrow (3, 4)$
^{178}Au	5754(7)	5758(8)	[88]	^{174}Ir	175.1(9)	6061(7)	$(3^+, 4^+) \rightarrow (3, 4)$
^{178}Au^m	5840(5)	5843(6)	[88]	^{174}Ir	140.5(12)	6115(5)	$(7^+, 8^+) \rightarrow (7, 8)$
^{178}Au^m	5963(4)	5961(10)	[88]	^{174}Ir	24.5(26)	6125(7)	$(7^+, 8^+) \rightarrow (7, 8)$
^{176}Au^{hs}	6112(4)	6117(7)	[99]	^{172}Ir^{hs}	175.5(6)	6430(4)	$(8^+, 9^+) \rightarrow (7^+)$
^{176}Au^{hs}	6073(5)	6082(7)	[99]	^{172}Ir^{hs}	211.5(4)	6426(5)	$(7^+, 9^+) \rightarrow$ (-)
^{173}Pt	6202(4)	6201(4)	[100]	^{169}Os	35.1(5)	6381(4)	$(7/2^-) \rightarrow (7/2^-)$
^{173}Pt	6202(4)	6097(5)	[100]	^{169}Os	136.3(5)	6485(4)	$(7/2^-) \rightarrow (7/2^-)$
^{173}Pt	6074(5)	6067(5)	[100]	^{169}Os	171.1(6)	6389(5)	$(7/2^-) \rightarrow (9/2^-)$
^{174}Pt	5754(10)	5762(5)	[98]	^{170}Os	287.6(11)	6177(10)	$(0^+) \rightarrow (2^+)$
^{175}Pt	5952(5)	5948(4)	[11]	^{171}Os	77.1(5)	6168(5)	$(7/2^-) \rightarrow (5/2^-)$
^{175}Pt	5828(7)	5819(4)	[11]	^{171}Os	131.4(6)	6096(7)	$(9/2^-) \rightarrow (7/2^-)$
^{175}Pt	5830(5)	5814(4)	[11]	^{171}Os	134.6(5)	6101(5)	$(7/2^-, 9/2^-) \rightarrow (7/2^-)$
^{175}Pt	5822(5)	5814(4)	[11]	^{171}Os	211.9(9)	6170(5)	$(7/2^-, 9/2^-) \rightarrow (5/2^-)$
^{176}Pt	5522(4)	5530(3)	[69]	^{172}Os	228.4(9)	5879(4)	$(7/2^-, 9/2^-) \rightarrow (5/2^-)$
^{177}Pt	5429(4)	5423(10)	[69]	^{173}Os	92.2(6)	5647(4)	$(7/2^-, 9/2^-) \rightarrow (5/2^-)$
^{178}Pt	5289(4)	5291(4)	[101]	^{172}Os	158.7(6)	5569(4)	$(7/2^-, 9/2^-) \rightarrow (5/2^-)$
^{174}Ir	5278(4)	5275(10)	[102]	^{170}Re	224.9(9)	5627(4)	$(3^+) \rightarrow (3^+)$
^{174}Ir	5304(4)	5316(10)	[102]	^{170}Re	193.8(5)	5623(4)	$(3^+) \rightarrow (3^+)$
^{174}Ir	5486(4)	5478(6)	[102]	^{170}Re	210.8(5)	5637(12)	$(7^+) \rightarrow (7^+)$
^{174}Ir	5506(7)	5478(6)	[102]	^{170}Re	190.1(6)	5626(13)	$(7^+) \rightarrow (7^+)$
^{181}Au	5248(5)	5246(4)	[89]	^{177}Ir	171.0(5)	5538(4)	$(3/2^-) \rightarrow$ (-)
^{181}Au	5305(6)	5246(4)	[89]	^{177}Ir	127.5(7)	5752(6)	$(3/2^-) \rightarrow$ (-)
^{181}Au	5472(4)	5479(5)	[89]	^{177}Ir	148.4(6)	5744(4)	$(3/2^-) \rightarrow (3/2^-)$

Table 3.5: Table of identified α-γ coincidences shown in Fig. 3.19, from the experiment JR115. The 2^{nd} and 6^{th} column denotes measured energies of α and γ-ray transitions, while the 3^{rd} column represents tabulated values. The 4^{th} column contains references for the E_α^{tab}. The 7^{th} column represents the $Q_{\alpha,tot}$. The last column represent initial I_i and final I_f spins and parities for γ-ray transitions in child nuclei.

Summary and future outlook

This work presents results of α-decay spectroscopy of two neutron-deficient isotopes ^{179}Hg and ^{177}Au. The data for the study of ^{179}Hg isotope were acquired during the experiment with code name S17, while ^{177}Au nuclei were primarily produced in the experiment JR115. Both experiments were performed at the Accelerator Laboratory of the University of Jyväskylä, Finland. The experimental setup was composed of the Jurogam2 surrounding the target, the gas-filled separator RITU and the focal plane spectrometer GREAT. The duration of both experiments was more than 10 days. This work is aimed on the analysis of the data measured at the focal plane of the RITU separator.

In the S17 experiment the α-decay fine-structure of ^{179}Hg was observed for the first time. This result was achieved thanks to the recoil-decay tagging technique, which allowed for inspection of correlated α decays and α-γ coincidences. A newly observed α-decay branch with $E_\alpha = 6156$ keV depopulates the $I^\pi = (7/2^-)$ ground state in ^{179}Hg to the 131.3 keV excited state in ^{175}Pt. The α-decay branching ratio $b_\alpha = 0.23$ % and reduced decay width $\delta^2 = 1.7$ keV were calculated based on experimental data and previous studies of ^{179}Hg. These values were used to determine the hindrance factor $HF = 41(19)$. This value suggest the same parity in the parent and child nucleus. Owing to the presence of Pt K_β x rays, an experimentally deduced conversion coefficient $\alpha_K(131.3) = 3.9$ was measured for the first time. Due to the prompt nature of the 131.3 keV transition, it was assigned the $M1$ multipolarity. Our experimental observations were verified by a GEANT4 simulation.

The methods used in the experiment S17 were used to analyse the data from the experiment JR115. Two fine-structure α decays of the ^{177}Au were observed. First, the known 5932 keV α transition was observed in coincidence with the 215.7 keV γ ray. This established a crossover transition between the $(9/2^-)$ excited state at 424.4 keV and $(11/2^-)$ isomeric state at 213 keV in ^{173}Ir. Furthermore, a new 5998 keV α-decay branch was observed in ^{177}Au feeding the 156 keV excited state in ^{173}Ir. Two de-excitation paths were identi-

fied for this state. First a 156 keV transition leading to the ground state in ^{173}Ir was observed. Based on the similarities with neighbouring nuclei of ^{173}Ir, a second 134.5 keV transition was tentatively placed as a crossover transition from the 156 keV excited state to a new 21.6 keV level in ^{173}Ir. Owing to significantly higher statistics of 156.1 keV γ rays, a conversion coefficient $\alpha_K(156.1) = \dot{3}.3(15)$ was measured. The calculated value of the conversion coefficient was overestimated because Ir K_β x rays from the 156.1 keV transition were mixed with Ir K_β x originating from 134.5 keV and 215.1 keV transitions. This, combined with the prompt nature of the 156.1 keV γ ray implies $(M1 + E2)$ multipolarity character for the 156.1 keV transition. To verify our assumption in regards to the ^{177}Au decay a GEANT4 simulation was performed. In the final part of the analysis, other prompt plus delayed α-γ coincidences were investigated. Two transitions with energies $E_\gamma = 210.3$ keV and 190.2 keV, originating from the 210 keV level in ^{170}Re were observed in both matrices. A half-life of $T_{1/2} = 129(72)$ ns was measured for the 210 keV excited state in ^{170}Re.

Future research should further develop and confirm these initial findings by exploiting the study of the α-decay fine structure in this region of nuclei. For example, level schemes in neighbouring ^{173}Ir isotopes lack critical informations about low-lying states. In addition, experiments focused on the α decay spectroscopy combined with conversion electrons spectroscopy of both studied isotopes are needed to increase the statistics and therefore confirm these novel finding.

Zhrnutie

V tejto práci sú prezentované výsledky štúdia alfa rozpadovej spektroskopie dvoch neutrónovo deficitných izotopov ^{179}Hg a ^{177}Au. Dáta pre štúdium izotopu ^{179}Hg boli získané počas experimente s kódovým označením S17, zatiaľ čo jadrá ^{177}Au boli primárne produkované v experimente JR11. Oba experimenty boli vykonané v urýchľovačovom laboratóriu Univerzity v Jyväskylä, Fínsko. Oba experimenty pozostávali z poľa germániových detektorov Jurogam 2 umiestneného okolo terča, plynového separátora RITU a fokálneho spektrometra GREAT. Trvanie oboch experimentov bolo viac ako 10 dní. Táto práca je zameraná na analýzu dát nameraných vo fokálnej rovine separátora RITU.

V experimente S17 bola prvý krát pozorovaná jemná štruktúra alfa rozpadu ^{179}Hg. Tento výsledok bol dosiahnutý vďaka metóde založenej na identifikácií rozpadov spätne odrazených jadier, ktorá umožnila inšpekciu korelovaných alfa rozpadov a alfa-gama koincidencií. Novo pozorovaná alfa rozpadová vetva ^{179}Hg s energiou E_α = 6156 keV pochádza z $I^\pi = (7/2^-)$ základného stavu v ^{179}Hg, pričom populuje 131 keV vzbudenú hladinu so spinom a paritou $(9/2^-)$ v ^{175}Pt. Na základe experimentálnych dát a predošlých štúdií ^{179}Hg bola vypočítaná hodnota väzbového pomeru b_α = 0.23 % a redukovaná šírka rozpadu δ^2 = 1.7 keV. Tieto hodnoty boli následne použité na určenie faktoru potlačenia *HF* = 42(19). Táto hodnota naznačuje podobnú paritu v rodičovskom a detskom jadra. Vďaka prítomnosti Pt K_β röntgenov bolo možné prvý krát experimentálne stanoviť konverzný koeficient $\alpha_K(131.3)$ = 3.9. Na základe toho že bol 131.3 keV prechod videný ako promptný, mu bolo možné priradiť multipolaritu $M1$. Naše výsledky boli overené aj GEANT4 simuláciou.

Metodiky použité v experimente S17 boli aplikované aj na analýzu dát experimentu JR115. Dve jemné štruktúry alfa rozpadu ^{177}Au boli pozorované. V prvom rade bol videný známy 5932 keV alfa rozpad v koincidencií s gama žiarením s energiou 215.7 keV. Vďaka tomu bol po prvý krát experimentálne identifikovaný prechod spájajúci vzbudenú hladinu $(9/2^-)$ s energiou rovnou 424.4 keV a 213(16) keV izomérnu hladinu $(11/2^-)$ v ^{173}Ir.

Následne bola pozorovaná nová alfa rozpadová vetva ^{177}Au s energiou 5998 keV populujúca vzbudenú hladinu na 156 keV v ^{173}Pt. Boli identifikované dva spôsoby deexcitácie tejto vzbudenej hladiny. Prvý spôsob je pomocou 156.1 keV prechodu populujúci základný stav v ^{173}Ir. Na základe podobností so susediacimi jadrami ^{173}Ir bol predbežne priradený druhý 134.5 keV prechod spájajúci 156.1 keV level s novým 21.6 keV vzbudeným stavom v ^{173}Ir.

Vďaka podstatne vyššej štatistike 156.1 keV gama kvánt bolo možné zmerať konverzný koeficient $\alpha_K(156.1)$ = 3.3(15). Takto vypočítaná hodnota bola nadhodnotená lebo Ir K_β röntgeny z 156.1 keV prechodu boli zmiešané s Ir K_β röntgeny pochádzajúcich z 134.5 a 215.1 keV prechodov. Táto skutočnosť spolu s promptným charakterom 156.1 keV gama kvanta naznačuje ($M1$ + $E2$) multipolaritu pre 156.1 keV prechod v ^{173}Ir. Na overenie našich predpokladov ohľadne alfa rozpadu ^{177}Au bola vykonaná GEANT4 simulácia. Na záver boli skúmané zvyšné promptné a oneskorené α-γ koincidencie. Dva prechody s energiami E_γ = 210.3 keV and 190.2 keV pochádzajúce z 210 keV vzbudenej hladiny v ^{170}Re boli pozorované v obidvoch maticiach. Polčas pre 210 keV stav v ^{170}Re bol nameraný s hodnotou $T_{1/2}$ = 129(72) ns.

Budúci výskum by mal ďalej rozvíjať a potvrdiť naše pozorovania využitím štúdie jemnej štruktúry alfa rozpadu v tejto oblasti jadier. Napríklad schémam vzbudených hladín v susedných izotopoch ^{173}Ir chýbajú dôležité informácie o nízko poloených hladinách. Okrem toho je potrebné vykonať experimenty zamerané na alpha rozpadovú spektroskopiu kombinovanú so spektroskopiou konverzných elektrónov oboch študovaných izotopov, aby sa navýšila štatistika a potvrdili naše objavy.

Bibliography

[1] Y. Qian and Z. Ren. "New insight into α clustering of heavy nuclei via their α decay". In: *Physics Letters B* 777 (2018), pp. 298–302.

[2] K. P. Santhosh and C. Nithya. "Predictions on the modes of decay of even Z superheavy isotopes within the range 104Z136". In: *Atomic Data and Nuclear Data Tables* 119 (2018), pp. 33–98.

[3] J. P. Cui *et al.* "α-decay half-lives of superheavy nuclei". In: *Phys. Rev. C* 97 (2018), p. 014316.

[4] M. Ismail and A. Adel. "Effect of deformation parameters, Q value, and finite-range NN force on α-particle preformation probability". In: *Phys. Rev. C* 89 (2014), p. 034617.

[5] T. Grahn *et al.* "Collectivity of ^{196}Po at low spin". In: *Phys. Rev. C* 80 (1 2009), p. 014323.

[6] A. Andreyev *et al.* "A triplet of differently shaped spin-zero states in the atomic nucleus ^{186}Pb". In: *Nature* 405 (2000), pp. 430–433.

[7] M. Leino *et al.* "Gas-filled recoil separator for studies of heavy elements". In: *Nuclear Instruments and Methods in Physics Research Section B: Beam Interactions with Materials and Atoms* 99 (1995), pp. 653–656.

[8] R. D. Page *et al.* "The GREAT spectrometer". In: *Nuclear Instruments and Methods in Physics Research Section B: Beam Interactions with Materials and Atoms* 204 (2003). 14th International Conference on Electromagnetic Isotope Separators and Techniques Related to their Applications, pp. 634–637.

[9] E. S. Paul *et al.* "In-beam γ-ray spectroscopy above Sn-100 using the new technique of recoil decay tagging". In: *Physical Review C* 51 (1995), p. 78.

[10] S. M. Polikanov and G. Sletten. “Evidence for nuclear shape coexistence in ^{180}Hg”. In: *Z. Physik A - Atomic Nuclei* 325 (1986), pp. 197–202.

[11] P. Peura *et al.* “Quasiparticle alignments and α-decay fine structure of ^{175}Pt”. In: *Phys. Rev. C* 89 (2014), p. 024316.

[12] G. Gamow. “Mass Defect Curve and Nuclear Constitution”. In: *Proceedings of The Royal Society A: Mathematical, Physical and Engineering Sciences* 126 (1930), pp. 632–644.

[13] T. Meyer-Kuckuk. *Fyzika atómového jádra*. SNTL - Státní nakladatelství technické, 1979.

[14] D. J. Rowe and J. L. Wood. *Fundamentals of Nuclear Models: Foundational Models*. Vol. 1. 5 Toh Tuck Link, Singapore 596224: World Scientific Publishing Co. Pte. Ltd., 2010. ISBN: 978-981-256-955-4.

[15] M. M. Goeppert. “On Closed Shells in Nuclei. II”. In: *Phys. Rev.* 75 (12 1949), pp. 1969–1970.

[16] O. Haxel *et al.* “On the "Magic Numbers" in Nuclear Structure”. In: *Phys. Rev.* 75 (1949), pp. 1766–1766.

[17] C. Lizarazo. “γ-ray spectroscopy of ^{92,94}Se isomeric decay”. MA thesis. Darmstadt: TU Darmstadt, 2018.

[18] K. S. Krane. *Introductory Nuclear Physics*. John Wiley & Sons, 2010. ISBN: 978-0471805533.

[19] S. Raman, C. W. Nestor, and P. Tikkanen. “Transition probability from the ground to the first-excited 2^+ state of even-even nuclides”. In: *Atomic Data and Nuclear Data Tables* 78.1 (2001), pp. 1–128.

[20] G. Giacalone. “A matter of shape: seeing the deformation of atomic nuclei at high-energy colliders”. MA thesis. Paris: Université Paris-Saclay, CNRS, CEA, 2020.

[21] S. G. Nilsson. “BINDING STATES OF INDIVIDUAL NUCLEONS IN STRONGLY DEFORMED NUCLEI”. In: *Kgl. Danske Videnskab. Selskab., Mat.-fys Medd.* 29 (1955).

[22] X. Wang. *Exotic Collective Excitations at High Spin: Triaxial Rotation and Octupole Condensation*. 2008.

[23] M. A. Alwaleedi. “Band structures of ^{131}Ce”. MA thesis. Liverpool: Oliver Lodge Laboratory, 2013.

[24] R. W. Gurney and Edw. U. Condon. “Wave Mechanics and Radioactive Disintegration”. In: *Nature* 122 (1928), pp. 439–439.

[25] R. Resnick R. Eisberg. *Quantum Physics of Atoms, Molecules, Solids, Nuclei, and Particles*. Vol. 2. John Wiley & Sons, 1985. ISBN: 978-0471873730.

[26] W. Loveland, D. Morrissey, and G. Seaborg. *Modern Nuclear Chemistry*. 2005. ISBN: 978-0471115328.

[27] F. G. Kondev. In: *Nuclear Data Sheets* 159 (1 2019).

[28] J. O. Rasmussen. “Alpha-Decay Barrier Penetrabilities with an Exponential Nuclear Potential: Even-Even Nuclei”. In: *Phys. Rev.* 113 (1959), pp. 1593–1598.

[29] K. Heyde. *Basic Ideas and Concepts in Nuclear Physics Volume 3*. CRC Press, 2004. ISBN: 978-0750309806.

[30] J. M. Blatt and V. F. Weisskopf. *Theoretical Nuclear Physics*. Dover Publications, 2010. ISBN: 0486668274.

[31] V. F. Weisskopf. “Radiative Transition Probabilities in Nuclei”. In: *Phys. Rev.* 83 (1951), pp. 1073–1073.

[32] A. H. Wapstra *et al.* “The decay of ^{203}Hg, ^{203}Pb and ^{201}Pb”. In: *Physica* 20 (1954), pp. 169–177.

[33] T. Kibédi and *et al.* “Evaluation of theoretical conversion coefficients using BrIcc”. In: *Nuclear Instruments and Methods in Physics Research Section A: Accelerators, Spectrometers, Detectors and Associated Equipment* 589 (2008), pp. 202–229.

[34] J. A. Bearden and A. F. Burr. “Reevaluation of X-Ray Atomic Energy Levels”. In: *Rev. Mod. Phys.* 39 (1967), pp. 125–142.

[35] P. Raghavan. “Table of nuclear moments”. In: *Atomic Data and Nuclear Data Tables* 42 (1989), pp. 189–291.

[36] G. Dracoulis P. Walker. “Energy traps in atomic nuclei”. In: *Nature* 399 (1999), pp. 35–45.

[37] S. M. Polikanov and G. Sletten. “Spontaneously fissioning isomers in U, Pu, Am and Cm isotopes”. In: *Nuclear Physics A* 151 (1970), pp. 656–672.

[38] T. Cousins, T. J. Kennett, and W. V. Prestwich. "Low energy states in ^{180}Ta". In: *Phys. Rev. C* 24 (1981), pp. 911–916.

[39] K. E. G. Löbner. "Systematics of absolute transition probabilities of K-Forbidden γ-ray transitions". In: *Physics Letters B* 26 (1968), pp. 369–370.

[40] D. Zakoucky *et al.* "Parity Non-Conservation Observed in Nuclear gamma Decay of ^{180m}Hf". In: *Acta Physica Polonica Series B* 39 (2008).

[41] G. Racah. "Theory of Complex Spectra. III". In: *Phys. Rev.* 63 (1943), pp. 367–382.

[42] J. Ressler *et al.* "Transition from the seniority regime to collective motion". In: *Physical Review C* 69 (2004).

[43] P. Van Isacker. "Seniority isomers in nuclei". In: *Journal of Physics: Conference Series* 322 (2011), p. 012003.

[44] B. Rubio and W. Gelletly. "Beta Decay of Exotic Nuclei". In: *The Euroschool Lectures on Physics with Exotic Beams, Vol. III*. Ed. by J.S. Al-Khalili and E. Roeckl. Springer Berlin Heidelberg, 2009, pp. 99–151. ISBN: 978-3-540-85839-3.

[45] O. Litaize and O. Serot. "Investigation of phenomenological models for the Monte Carlo simulation of the prompt fission neutron and γ emission". In: *Phys. Rev. C* 82 (2010), p. 054616.

[46] J. Sarén *et al.* "The new vacuum-mode recoil separator MARA at JYFL". In: *Nuclear Instruments and Methods in Physics Research Section B: Beam Interactions with Materials and Atoms* 266 (2008). Proceedings of the XVth International Conference on Electromagnetic Isotope Separators and Techniques Related to their Applications, pp. 4196–4200.

[47] C. W. Beausang *et al.* "Measurements on prototype Ge and BGO detectors for the Eurogam array". In: *Nuclear Instruments and Methods in Physics Research Section A: Accelerators, Spectrometers, Detectors and Associated Equipment* 313 (1992), pp. 37–49.

[48] G. Duchêne *et al.* "The Clover: a new generation of composite Ge detectors". In: *Nuclear Instruments and Methods in Physics Research Section A: Accelerators, Spectrometers, Detectors and Associated Equipment* 432 (1999), pp. 90–110.

[49] D. C. Radford. “ESCL8R and LEVIT8R: Software for interactive graphical analysis of HPGe coincidence data sets”. In: *Nuclear Instruments and Methods in Physics Research Section A: Accelerators, Spectrometers, Detectors and Associated Equipment* 361 (1995), pp. 297–305.

[50] A. Georgiev and W. Gast. “Digital pulse processing in high resolution, high throughput, gamma-ray spectroscopy”. In: *IEEE Transactions on Nuclear Science* 40 (1993), pp. 770–779.

[51] M. P. Carpenter *et al.* “Test and performance of a BGO Compton-suppression shield for GAMMASPHERE”. In: *Nuclear Instruments and Methods in Physics Research Section A: Accelerators, Spectrometers, Detectors and Associated Equipment* 353 (1994), pp. 234–238.

[52] J. Pakarinen *et al.* “The JUROGAM 3 spectrometer”. In: *The European Physical Journal A* 56 (2020), pp. 1–8.

[53] J. Pakarinen. “Probing non-yrast structures of ^{186}Pb in a RDT measurement employing the JUROGAM array”. MA thesis. Jyväskylä: University of Jyväskylä, 2005.

[54] J. Pakarinen *et al.* “The SAGE spectrometer”. In: 50 (2014), pp. 1–11.

[55] P. Papadakis *et al.* “The SAGE spectrometer: A tool for combined in-beam γ-ray and conversion electron spectroscopy”. In: *Journal of Physics: Conference Series* 312 (2011), p. 052017.

[56] J. Sarén *et al.* “Absolute transmission and separation properties of the gas-filled recoil separator RITU”. In: *Nuclear Instruments and Methods in Physics Research Section A: Accelerators, Spectrometers, Detectors and Associated Equipment* 654 (2011), pp. 508–521.

[57] M. Balogh. “Nuclear structure and phenomenon of shape coexistence in gold isotopes”. MA thesis. Bratislava: Comenius University, 2020.

[58] R. Brun and F. Rademakers. “ROOT An object oriented data analysis framework”. In: *Nuclear Instruments and Methods in Physics Research Section A: Accelerators, Spectrometers, Detectors and Associated Equipment* 389 (1997), pp. 81–86.

[59] S. Y. F. Chu, L. P. Ekström, and R. B. Firestone. “WWW Table of radioactive isotopes”. In: *APS Division of Nuclear Physics Meeting Abstracts*. 1999.

[60] M. R. Bhat. “Evaluated Nuclear Structure Data File (ENSDF)”. In: *Nuclear Data for Science and Technology* (2023). edited by S. M. Qaim (Springer-Verlag, Berlin, Germany), p. 817.

[61] A. N. Andreyev *et al.* “GEANT Monte Carlo simulations for the GREAT spectrometer”. In: *Nuclear Instruments and Methods in Physics Research Section A: Accelerators, Spectrometers, Detectors and Associated Equipment* 533 (2004), pp. 422–434.

[62] I. Lazarus *et al.* “The GREAT triggerless total data readout method”. In: *IEEE Transactions on Nuclear Science* 48 (2001), pp. 567–569.

[63] F. A. Ali. *to be published*.

[64] P. Rahkila. “Grain - A java data analysis system for total data readout”. In: *Nuclear Instruments and Methods in Physics Research Section A: Accelerators, Spectrometers, Detectors and Associated Equipment* 595 (2008), pp. 637–642.

[65] J. Mayer. *Nuclear Spectrum Analysis Tool*. https://github.com/janmayer/hdtv. 1990.

[66] A.G. Demin *et al.* “New mercury isotopes”. In: *Nuclear Physics A* 106 (1967), pp. 337–349.

[67] P.G. Hansen *et al.* “Studies of the α-active isotopes of mercury, gold and platinum”. In: *Nuclear Physics A* 148 (1970), pp. 249–272.

[68] P. G. Hansen *et al.* “The alpha decay of ^{179}Hg and ^{178}Hg”. In: *Nuclear Physics A* 160 (1971), pp. 445–448.

[69] E. Hagberg *et al.* “Alpha decay of neutron-deficient mercury isotopes and their daughters”. In: *Nuclear Physics A* 318 (1979), pp. 29–44.

[70] M. Venhart *et al.* “Determination of α-decay branching ratios for ^{178,179}Hg”. In: *Eur. Phys. J. A* 48 (2012).

[71] A. Siivola. “Alpha-active platinum isotopes”. In: *Nuclear Physics* 84 (1966), pp. 385–397.

[72] H. Gauvin *et al.* “Reactions of ^{40}Ar with ^{159}Tb, ^{142}Nd and ^{144}Sm; New α-activities from ^{189}Bi, ^{173}Pt and ^{177}Au”. In: *Nuclear Physics A* 208 (1973), pp. 360–370.

[73] M. S. Basunia. “Nuclear Data Sheets for A = 179”. In: *Nuclear Data Sheets* (2005).

[74] M. Sedlák. *Private Communication*. August, 2021.

[75] S. Agostinelli *et al.* "Geant4 a simulation toolkit". In: *Nuclear Instruments and Methods in Physics Research Section A: Accelerators, Spectrometers, Detectors and Associated Equipment* 506 (2003), pp. 250–303.

[76] James F. Ziegler, M.D. Ziegler, and J.P. Biersack. "SRIM - The stopping and range of ions in matter (2010)". In: *Nuclear Instruments and Methods in Physics Research Section B: Beam Interactions with Materials and Atoms* 268.11 (2010), pp. 1818–1823.

[77] B. Pritychenko and A. Sonzogni. "Q-value calculator (QCalc)". In: *National Nuclear Data Center, Brookhaven National Laboratory: Upton, NY, USA* (2016).

[78] M. Nyman. "Shape coexistence in light bismuth and astatine isotopes: An in-beam and decay-spectroscopic study". In: *Research report/Department of Physics, University of Jyväskylä* (2009).

[79] F. Kondev *et al.* "First Observation of Excited Structures in Neutron-Deficient ^{179}Hg: Evidence for multiple shape coexistence". In: *Phys.Lett.* 528B (2002), p. 221.

[80] C. A. Kalfas *et al.* "Study of high spins in ^{173}Os". In: *Nuclear Physics A* 526 (1991), pp. 205–223.

[81] J. Espino *et al.* "Rotational band structures in ^{171,172}W: Aspects on signature partnership at high spin". In: *Nuclear Physics A* 567 (1994), pp. 377–413.

[82] I. Rezanka *et al.* "High-spin rotational states in ^{169}Hf from the ^{159}Tb(^{14}N, 4nγ) reaction and decay of ^{169}Ta". In: *Phys. Rev. C* 11 (1975), pp. 1767–1785.

[83] G. D. Dracoulis *et al.* "Intrinsic states and rotational bands in ^{177}Pt". In: *Nuclear Physics A* 510 (1990), pp. 533–556.

[84] XU Yan-Bing *et al.* "Study of Collective Rotational Bands in ^{179}Pt". In: *Chinese Physics C* 28 (2004), pp. 584–587.

[85] M. J. A. De Voigt *et al.* "Rotational bands in ^{181}Pt". In: *Nuclear Physics A* 507 (1990), pp. 447–471.

[86] R. D. Harding *et al.* "Laser-assisted nuclear decay spectroscopy of ^{176,177,179}Au". In: *Phys. Rev. C* 104 (2021), p. 024326.

[87] R. D. Harding *et al.* "Laser-assisted decay spectroscopy for the ground states of ^{180,182}Au". In: *Physical Review C - Nuclear Physics* 102 (2020).

[88] M. Al-Monthery. "Decay Studies of ^{178}Au and Its Daughter ^{174}Ir". MA thesis. York, England: University of York, 2019.

[89] C. R. Bingham *et al.* "α-decay rates for $^{181-186}$Au and $^{181-185}$Pt isotopes". In: *Phys. Rev. C* 51 (1995), pp. 125–135.

[90] P. J. Sellin *et al.* "The limit of stability of proton-rich thallium isotopes: a search for the decay of ^{177}Tl". In: *Zeitschrift für Physik A Hadrons and Nuclei* 338 (2 1991).

[91] F. G. Kondev *et al.* "Identification of excited structures in proton unbound nuclei ^{173,175,177}Au: shape co-existence and intruder bands". In: *Physics Letters B* 512 (2001), pp. 268–276.

[92] A. N. Andreyev *et al.* "Decay of the $9/2^-$ isomer in ^{181}Tl and mass determination of low-lying states in ^{181}Tl, ^{177}Au, and ^{173}Ir". In: *Phys. Rev. C* 80 (2 2009), p. 024302.

[93] C. M. Baglin. "Nuclear Data Sheets for A = 169". In: *Nuclear Data Sheets* 109 (2008), pp. 2033–2256.

[94] K. H. Schmidt. "A new test for random events of an exponential distribution". In: *Eur. Phys. J. A* 8 (2000), pp. 141–145.

[95] M. Venhart *et al.* "Population of a low-spin positive-parity band from high-spin intruder states in ^{177}Au: The two-state mixing effect". In: *Physics Letters B* 806 (2020), p. 135488.

[96] S. A. Gillespie *et al.* "Identification of a 6.6 μm isomeric state in ^{175}Ir". In: *Phys. Rev. C* 99 (2019), p. 064310.

[97] M. Venhart. *Private Communication*. March, 2023.

[98] T.-M. Goon. "Alpha and Gamma-ray Spectroscopic Studies of Au, Pt, and Ir Nuclei Near the Proton Dripline". MA thesis. Knoxville: University of Tennessee, 2004.

[99] A. N. Andreyev *et al.* "α decay of ^{176}Au". In: *Phys. Rev. C* 90 (4 2014), p. 044312.

[100] A. M. Thornthwaite. "Structure of the neutron-deficient nuclei ^{173}Au and ^{173}Pt and their α-decay descendants". MA thesis. Liverpool, England: University of Liverpool, 2014.

[101] Y. A. Akovali. “Review of Alpha-Decay Data from Doubly-Even Nuclei”. In: *Nuclear Data Sheets* 84 (1998), pp. 1–114.

[102] W.-D. Schmidt-Ott *et al.* “Isomerism in neutron-deficient iridium isotopes alpha- and beta-decay studies of $^{171-175}$Ir”. In: *Nuclear Physics A* 545 (1992), pp. 646–664.

Appendix A

Publications

M. Balogh, E. Jajčišinová, M. Venhart, A. Herzáň, J. L. Wood, D. T. Joss, F. A. Ali, K. Auranen, S. Bánovská, M. Bírová, R. J. Carroll, D. M. Cox, J. G. Cubiss, T. Davis, M. C. Drummond, P. T. Greenlees, T. Grahn, A. Gredley, J. Henderson, U. Jakobsson, R. Julin, S. Juutinen, G. Kantay, J. Konki, P. Konopka, M. Leino, V. Matoušek, A. K. Mistry, C. G. McPeake, D. O'Donnell, R. D. Page, J. Pakarinen, P. Papadakis, J. Partanen, P. Peura, P. Rahkila, P. Ruotsalainen, M. Sandzelius, J. Sarén, B. Saygl, M. Sedlák, D. Seweryniak, C. Scholey, J. Sorri, J. A. Špaček, S. Stolze, M. Taylor, A. Thornthwaite, J. Uusitalo, M. Veselský, S. Vielhauer, F. P. Wearing, F.P.
"New collective structures in Au 179 and their implications for the triaxial deformation of the Pt 178 core".
Physical Review C, **106**, 6 (2022).
DOI: https://doi.org/10.1103/PhysRevC.106.064324

M. Balogh, A. Herzáň, V. Matoušek, M. Sedlák, M. Beňo, J. Dobrovodský, G. Kantay, P. Konopka, P. Noga, A. Repko, A. Špaček, D. Vaňa, M. Venhart, S. Vielhauer.
"Automated method for offline correction of spectrometry data affected by time instability".
Nuclear Instruments and Methods in Physics Research Section A, **1004**, 11 (2021).
DOI: https://doi.org/10.1016/j.nima.2021.165368

M. Venhart, J. L. Wood, M. Sedlák, M. Balogh, M. Bírová, A. J. Boston, T. E. Cocolios, L. J. Harkness-Brennan, R.-D. Herzberg, L. Holub, D. T. Joss, D. S. Judson, J. Kliman, J. Klimo, L. Krupa, J. Lušsnák, L. Makhathini, V. Matoušek, Š. Motyčák, R. D. Page, A. Patel, K. Petrík, A. V. Podshibyakin, P. M. Prajapati, A. M. Rodin, A. Špaček, R. Urban, C. Unsworth, M. Veselský.
"New systematic features in the neutron-deficient Au isotopes".
Journal of Physics G: Nuclear and Particle Physics **44**, 074003 (2017).
DOI: https://doi.org/10.1088/1361-6471/aa7297